

Evolution, nucleosynthesis and yields of low mass AGB stars at different metallicities.

S. Cristallo¹ and O. Straniero¹

INAF-Osservatorio Astronomico di Collurania, 64100 Teramo, Italy

and

R. Gallino^{2,3}

Dipartimento di Fisica Generale, Università di Torino, 10125 Torino, Italy

Center for Stellar and Planetary Astrophysics, School of Mathematical Sciences, Monash

University, P.O. Box 28, Victoria 3800, Australia

and

L. Piersanti¹

INAF-Osservatorio Astronomico di Collurania, 64100 Teramo, Italy

and

I. Domínguez⁴

Departamento de Física Teórica y del Cosmos, Universidad de Granada, 18071 Granada, Spain

and

M.T. Lederer⁵

Institut für Astronomie, Türkenschanzstraße 17, A-1180 Wien, Austria

Received / Accepted

Received _____; accepted _____

ABSTRACT

The envelope of thermally pulsing AGB stars undergoing periodic third dredge-up episodes is enriched in both light and heavy elements, the ashes of a complex internal nucleosynthesis involving p, α and n captures over hundreds of stable and unstable isotopes. In this paper, new models of low-mass AGB stars ($2 M_{\odot}$), with metallicity ranging between $Z=0.0138$ (the solar one) and $Z=0.0001$, are presented. Main features are: i) a full nuclear network (from H to Bi) coupled to the stellar evolution code, ii) a mass loss-period-luminosity relation, based on available data for long period variables, and iii) molecular and atomic opacities for C- and/or N-enhanced mixtures, appropriate for the chemical modifications of the envelope caused by the third dredge up. For each model a detailed description of the physical and chemical evolution is presented; moreover, we present a uniform set of yields, comprehensive of all chemical species (from hydrogen to bismuth). The main nucleosynthesis site is the thin ^{13}C pocket, which forms in the core-envelope transition region after each third dredge up episode. The formation of this ^{13}C pockets is the principal by-product of the introduction of a new algorithm, which shapes the velocity profile of convective elements at the inner border of the convective envelope: both the physical grounds and the calibration of the algorithm are discussed in detail. We find that the pockets shrink (in mass) as the star climbs the AGB, so that the first pockets, the largest ones, leave the major imprint on the overall nucleosynthesis. Neutrons are released by the $^{13}\text{C}(\alpha, n)^{16}\text{O}$ reaction during the interpulse phase in radiative conditions, when temperatures within the pockets attain $T \sim 1.0 \times 10^8$ K, with typical densities of $(10^6 \div 10^7)$ neutrons \times cm^{-3} . Exceptions are found, as in the case of the first pocket of the metal-rich models ($Z = 0.0138$, $Z = 0.006$ and $Z = 0.003$), where the ^{13}C is only partially burned during the interpulse: the surviving part is ingested in the convective zone generated by the subsequent thermal pulse and then burned at $T \sim 1.5 \times 10^8$ K, thus producing

larger neutron densities (up to 10^{11} neutrons \times cm $^{-3}$). An additional neutron exposure, caused by the $^{22}\text{Ne}(\alpha, n)^{25}\text{Mg}$ during the thermal pulses, is marginally activated at large Z , but becomes an important nucleosynthesis source at low Z , when most of the ^{22}Ne is primary. The final surface compositions of the various models reflect the differences in the initial iron-seed content and in the physical structure of AGB stars belonging to different stellar populations. Thus, at large metallicities the nucleosynthesis of light elements (Sr, Y, Zr) is favored, whilst, decreasing the iron content, the overproduction of heavy s elements (Ba, La, Ce, Nd, Sm) and lead becomes progressively more important. At low metallicities ($Z=0.0001$) the main product is lead. The agreement with the observed [hs/lr] index observed in intrinsic C stars at different [Fe/H] is generally good. For the solar metallicity model, we found an interesting overproduction of some radioactive isotopes, like ^{60}Fe , as a consequence of the anomalous first ^{13}C pocket. Finally, light elements (C, F, Ne and Na) are enhanced at any metallicity.

Subject headings: stars: AGB and post-AGB — physical data and processes: nuclear reactions, nucleosynthesis, abundances

1. Introduction

The fundamental role played by Thermally Pulsing Asymptotic Giant Branch (TP-AGB) stars in the chemical evolution has been early recognized (Ulrich 1973). These stars are responsible for the nucleosynthesis of the main and the strong components of the s -process (Gallino et al. 1998; Travaglio et al. 1999) and contribute to the synthesis of various light elements, such as Li, C, N and F. These stars are bright red giants (M_{bol} ranging from -4 to -7). Their compact CO cores, whose mass ranges between 0.5 and $1 M_{\odot}$, are progressively cooled by plasma neutrino emission. Owing to the efficient heat conduction provided by degenerate electrons, the cores are maintained in a quasi isothermal state. Outside, there is an extended H-rich envelope, largely convective and progressively eroded by an intense mass loss (from 10^{-8} up to $10^{-4} M_{\odot}/\text{yr}$). The most interesting nucleosynthesis processes occur in a thin He-rich zone ($10^{-2} - 10^{-3} M_{\odot}$), located between the H and the He burning shells (hereafter He intershell).

The energy irradiated by these stars is mainly provided by the hydrogen burning. He burning is off during most of the AGB lifetime, so that the mass of the He intershell increases as a consequence of the advancing H burning shell. Then, periodic thermonuclear runaways (*Thermal Pulses*, TPs) are driven by violent He ignitions occurring when the He buffer attains a critical value (Schwarzschild & Härm 1965; Weigert 1966). Owing to the sudden release of energy by the 3α reactions, the He intershell becomes dynamically unstable against convection, while the external layers expand and cool down. As a consequence of the convective mixing, the whole He intershell becomes enriched in C (the main product of the partial He burning) and heavy elements, as produced by the s process (slow neutron captures). After a short period (10 to 200 yr), the thermonuclear runaway ceases, a stationary He burning takes place and convection disappears within the He intershell. Meanwhile, at the base of the H-rich envelope, the outgoing nuclear energy flux and the dropping temperature cause the radiative gradient to exceed the adiabatic gradient at positions more and more close to the He intershell. Finally, after a few

hundred years, the convective envelope penetrates the He intershell zone (Third Dredge Up, TDU). Straniero et al. (2003) showed that all TP-AGB stars may undergo recurrent third dredge up episodes, provided their envelope mass is sufficiently large. The minimum envelope mass for the occurrence of the TDU is of a few tenths of M_{\odot} , but the precise value depends on the core mass and on the envelope composition.

The occurrence of many third dredge up episodes in thermally pulsing low mass AGB stars has two important consequences. First of all it is responsible for the chemical modification of the envelope, which becomes progressively enriched in primary C and in the products of the s process. This provides a simple explanation for the observed spectroscopic sequence of AGB stars, from the M to the C type, through the MS and S stars (Smith & Lambert 1986; Malaney & Lambert 1988; Busso et al. 1995, 2001; Abia et al. 2002). The carbon excess, mixed within the envelope by previous third dredge up episodes, causes a significant increase of the radiative opacity in the envelope, so that the effective temperature sinks, the stellar radius increases and the mass loss rate rises. The second important consequence of the penetration of the convective envelope into the He- and C-rich He intershell concerns the formation of the so called ^{13}C pocket, where the main and the strong components of the classical s process are built up (see Gallino et al. 1998). Indeed, when the convective envelope recedes after a third dredge up episode, it leaves a small region (of the order of a few $10^{-4} M_{\odot}$) characterized by an increasing proton profile embedded in a bath of C and He (about 20 and 80 %, by mass fractions, respectively). During the relatively long period that elapses between two subsequent thermal pulses (interpulse), this region heats up; then, ^{13}C is firstly produced through the $^{12}\text{C}(p, \gamma)^{13}\text{N}(\beta^{-}\gamma)^{13}\text{C}$ and, later on (at $T \sim 0.9 \times 10^8$ K), the $^{13}\text{C}(\alpha, n)^{16}\text{O}$ provides the slow neutron flux required to activate the s process nucleosynthesis (Straniero et al. 1995). This pocket, strongly enriched in heavy elements, is engulfed into the convective zone generated by the subsequent thermal pulse. When the temperature at the base of this convective zone exceeds 2.7×10^8 K, a small neutron burst is powered by the $^{22}\text{Ne}(\alpha, n)^{25}\text{Mg}$ reaction. In low mass AGB stars of nearly solar metallicity, this second neutron source is

marginally activated (Straniero et al. 1997). Several observations confirm such a theoretical expectation (see e.g. Lambert et al. 1995; Abia et al. 2001). However, this second neutron source plays a more relevant role at low metallicity, even in low mass AGB stars.

Our knowledge of the physical properties of AGB stars and of their nucleosynthesis is mainly based on observations and models for intermediate age stellar populations of the Milky Way. The recent availability of optical and near IR spectroscopy of AGB stars belonging to nearby galaxies, dwarf spheroidals as well as the Magellanic Clouds, allow us to extend our investigation to metal poor stellar populations with age of the order 1-2 Gyr (Domínguez et al. 2004; de Laverny et al. 2006; Reyniers et al. 2007; Lebzelter et al. 2008; Abia et al. 2008). In addition to that, the growing number of studies on C-enhanced metal-poor stars enriched in s-elements (CEMPs), as stimulated by dedicated surveys (Beers et al. 1999; Christlieb 2003) provide new hints on the nucleosynthesis occurred in the now extinct AGB-halo population, as due to stars whose initial masses were in the range 1 to 7 M_{\odot} . The aim of this paper is to investigate how the theoretical scenario changes with decreasing metallicity, from the solar value to that of the metal poor stars belonging to the Galactic halo or to the nearby galaxies. Extant stellar models have been computed by adopting limited networks. For example, Karakas & Lattanzio (2007) include all the relevant processes and isotopes from H to Si, plus a few Fe-group isotopes and an artificial neutron sink to account for heavy element neutron captures. In this way, they can provide a reasonable estimate of the light element yields. Our approach is different. We compute evolutionary models, followed from the pre-main sequence up to the AGB tip, of stars with initial mass 2 M_{\odot} and different metallicities (namely, $Z=0.0138$, 0.006, 0.003, 0.001 and 0.0001), by adopting a full nuclear network that includes all the stable and the relevant unstable isotopes from hydrogen to bismuth. In our previous works (Gallino et al. 1998; Bisterzo et al. 2008), full nucleosynthesis calculations were obtained by means of a post-process code: in such a case, the main physical parameters were obtained by means of stellar models calculated with a restricted nuclear network involving key isotopes and reactions (Straniero et al. 1997). Then, an ad hoc (average) ^{13}C

pocket was imposed. In the present work stellar evolution and nucleosynthesis are coupled. If the faster post-process calculation allow us to investigate a large area in the parameter space, the present, fully coupled, calculations shed light on the possible feedbacks between chemical and physical evolution. These new models include several improvements in the input physics and in the computational algorithms (see Straniero et al. 2006, thereafter SGC06): the most important for the AGB evolution are illustrated in § 2. The calibration of some free parameters used by the mixing algorithm are discussed in § 3. Results are presented in § 4, § 5 and § 6. A final discussion follows in § 7.

2. The theoretical recipe: radiative opacity, nuclear data, mixing scheme and mass loss

The stellar models here presented have been computed by means of the FRANEC code (Chieffi et al. 1998, and references therein). An updated description of the various input physics adopted in the AGB computations can be found in SGC06. Owing to the particular relevance for the present paper, let us describe the radiative opacity, some key nuclear reaction rates, the mixing algorithm and the mass loss rate.

As discussed by Marigo (2002), the increase of the radiative opacity caused by the C dredged up induces important changes in the physical structure of the outermost layers of an AGB star, with important consequences on the effective temperature, the radius and the mass loss rate. In addition to that, when the CN cycle takes place in the innermost part of the convective envelope or immediately below it, an important fraction of the primary C that is dredged up to the surface may be converted into N. This is a common phenomenon in massive AGBs (the so called hot bottom burning, HBB) (Sugimoto 1971; Iben 1973), even if there are several observational evidence proving that deep-mixing processes can also occur in low mass AGBs (Cool Bottom Process, CBP) (see Nollett et al. 2003). As a consequence of the carbon dredged up, new molecular species may form in the cool atmosphere of an AGB star, like CN, HCN or C₂. Note that since

the amount of primary C synthesized by the 3α reaction and mixed by the third dredge up is of the same order of magnitude at any metallicity, the resulting overabundance of this element (and eventually N) is very large at low metallicity. Whilst at solar metallicity the final C enhancement in the envelope may be a factor of 2 to 4, at $Z=0.0001$ it rapidly attains a factor of 1000. For this reason, if the adoption of a proper radiative opacity (including enhancements of C and N) may only introduce limited quantitative changes in the overall picture of AGB stars with solar metallicity, its use at low metallicity is absolutely mandatory, because it leads to substantial modifications of the whole theoretical scenario (see Cristallo et al. 2007). Therefore, below $T = 10^4$ K we use new opacity tables derived by means of the COMA code (Aringer 2000), which include all the molecular and atomic species relevant for AGB atmospheres. At higher temperatures, the opacity tables have been calculated by means of the the OPAL web facility (<http://www-phys.llnl.gov/Research/OPAL/opal.html>). Table 1 lists the C and the N enhancement factors (with respect to the solar scaled values) adopted for the opacity tables at different metallicities. All the elements (except H, He, C and N) are assumed to be solar scaled (namely $[M/Fe]=0$). The enhancement of the α elements (O, Ne, Mg, Si, S, Ca), more appropriated for low metallicity halo stars, is not considered here, given that it only adds minor effects on the Rosseland mean opacity. The full database providing low temperature Rosseland opacities for a wide range of metallicities with varying carbon and nitrogen abundances is described in Lederer & Aringer (2008).

The nuclear network is essentially the same already described in Section 6 of SGC06: it includes about 500 isotopes (from H to Bi) and more than 700 nuclear reactions (charged particle reactions, neutron captures and β -decays). However, few reaction rates have been changed or updated. In particular, concerning reactions among charged nuclei, the $^{14}\text{N}(\alpha,\gamma)^{18}\text{F}$ rate is now taken from Görres et al. (2000), whilst for the $^{22}\text{Ne}(\alpha,n)^{25}\text{Mg}$ rate we follow Jaeger et al. (2001). Then, we have updated the $^{151}\text{Sm}(n,\gamma)^{152}\text{Sm}$ reaction rate, following the prescriptions reported by Abbondanno et al. (2004), and the cesium isotopes neutron captures rates, as suggested by

Patronis et al. (2004). Concerning the ^{175}Lu unthermalized isomeric state (see Section 7.5 of SGC06), we adopt an isomeric ratio $\text{IR}=0.2$ for temperatures lower than 2.0×10^8 K and $\text{IR}=0.25$ for higher temperatures. For a more detailed analysis of this important branching see Heil et al. (2008).

Mixing caused by convection is obtained by means of a time-dependent mixing scheme in which the degree of mixing between two mesh points, whose separation is ΔR , is linearly dependent on the ratio between the time step and the mixing time scale¹. An exhaustive description of the mixing algorithm can be found in Section 8 of SGC06 (see also Chieffi et al. 2001). Let us here recall the main concepts. The average convective velocity (v_c) is calculated according to the mixing-length theory (Cox & Giuli 1968), whereas the boundaries of the convective regions are located as given by the Schwarzschild criterion. In order to handle the instability of the convective boundary taking place during the third dredge up episodes, when the H-rich envelope penetrates the H-depleted core, we assume that the convective velocity drops to 0 following an exponential decline, namely:

$$v = v_{bce} \exp\left(-\frac{d}{\beta H_p}\right), \quad (1)$$

where d is the distance from the formal convective boundary (as defined by the Schwarzschild criterion), v_{bce} is the velocity at the formal convective boundary, H_p is the pressure scale height and β is a free parameter. All the evolutionary sequences presented in § 4 and 5 of the present paper have been obtained assuming $\beta = 0.1$. In the next Section we will describe the procedure followed to fix the value of the β parameter. A similar mathematical profile has been already applied to the calculation of AGB models by Herwig et al. (1997) (see also Herwig 2000). However, Herwig et al. (1997) used an exponential decline equation to calculate the diffusion coefficient, instead of the convective velocity, and applied this prescription to all the convective boundaries. In this way, they always obtain overshoot at the top and at the bottom of any convective zone,

¹Here the mixing time scale is defined as $\tau_{mix} = \Delta R/v_c$.

while in our models Eq. 1 works only when $v_{bce} > 0$, as it happens in the case of the bottom of the convective envelope at the time of the third dredge up. A second important difference concerns the mixing scheme, which determines the chemical coupling among mesh points within the same convective zone. In the diffusive mixing adopted by Herwig et al. (1997), the variation of the composition during a given time step depends on the second derivative of the composition with r (the radial coordinate), whilst in our algorithm this relationship is linear. These differences directly affect the profile of protons in the transition zone between the fully-convective envelope and the radiative core at the time of the third dredge up and the temperature attained in the He-rich intershell during a thermal pulse. We will discuss the consequences on the nucleosynthesis in the next section.

Concerning mass loss, we adopt a Reimers' formula ($\eta = 0.4$) for the pre-AGB evolution, whilst for the AGB, we follow a procedure similar to the one described by Vassiliadis & Wood (1993), but revising the mass loss-period and the period-luminosity relations, taking in to account more recent infrared observations of AGB stars (see SGC06 for the references). A comparison among our mass loss rate and those obtained by means of the Reimers' formula and the Vassiliadis and Wood prescriptions can be found in Section 5 of SGC06. An important remark concerns the dependence of the mass loss rate on the metallicity. The mass loss-period relation we use is based on data relative to Galactic AGB stars having nearly solar iron. In a recent paper, Groenewegen et al. (2007) showed that the same relation applies also to carbon stars in the Magellanic Clouds, whose metallicity is lower, on average, than that of the Galactic C-stars. Similar indications come from Spitzer observations of mass loss of carbon stars belonging to dwarf Spheroidal Galaxies (see Lagadec & Zijlstra 2008). In § 5 and § 6.5 we discuss the effect of different mass loss prescriptions on the evolution and nucleosynthesis of the $Z=0.0001$ model.

3. Instability of the convective boundary, dredge up and the formation of the ^{13}C pocket

In this Section we describe the models obtained by changing the value of the β parameter introduced in the previous Section to treat the instability of the convective boundary layer, arising when the H-rich convective envelope penetrates the He-rich zone. During a third-dredge-up episode, a chemical discontinuity forms at the convective boundary, causing an abrupt change of the radiative opacity. If a bare Schwarzschild criterion is adopted to limit the mixing, the average convective velocity drops from about 10^4 cm/s to 0 in 2 adjacent mesh points. In this condition, any perturbation causing mixing of material across the boundary layer leads to an increase of the opacity in the underlying stable zone, which immediately becomes unstable against convection. As it is well known, a similar condition occurs at the external border of the convective core during the central He-burning phase (Castellani et al. 1971). The most important consequence of this instability is the propagation of the convective instability; if in the case of the central-He burning such an occurrence implies the growth of the convective core, in the case of the TDU a deeper penetration of the convective envelope into the H-exhausted core is expected. Actually, it should exist a transition region, between the fully convective envelope and the radiatively stable H-exhausted core, where the convective velocity smoothly decreases to 0 and, therefore, a partial mixing takes place. In such a way, after any dredge-up episode, a zone with a smoothed H profile is left behind. Since the amount of ^{12}C is rather large (about 20 % by mass fraction) in this transition zone, at H re-ignition those few protons are captured by the abundant ^{12}C and form a ^{13}C pocket. Later on, the s process nucleosynthesis is activated, through the $^{13}\text{C}(\alpha, n)^{16}\text{O}$ reaction. Note that a ^{14}N pocket and a ^{23}Na pocket form, partially overlapped to the ^{13}C pocket (see next Section).

The mixing algorithm described in the previous Section mimics the formation of such a transition zone. The free parameter (β), used to tune the decline of the average convective velocity at the base of the convective envelope, determines the extension of such a transition zone

and, in turn, the amount of ^{13}C available for the neutron capture nucleosynthesis. To calibrate such a parameter, we have repeated the calculation of the same sequence TP-interpulse-TP for $0 \leq \beta \leq 0.2$. This test has been performed at two metallicities ($Z=0.0138$ and $Z=0.0001$) in order to test the sensitivity of our calibration procedure when changing the metal content. Results are illustrated in Fig. 1, Fig. 2, Fig. 3 and Fig. 4. Left panels refer to the epoch of the maximum penetration of the convective envelope during the third dredge up ². In the right panels, we show the same region, but after the H re-ignition, once the convective envelope recedes and the ^{13}C pocket is fully developed. The results of these test models are quantitatively summarized in Table 2, where in columns 1 to 7 we report: the value of β , the mass ΔM_{TDU} of the H-depleted material that is dredged up, the ratio $\lambda = \Delta M_{TDU}/\Delta M_{\text{H}}$ (being ΔM_{H} the mass of the material that has been burned by the H-shell during the previous interpulse period), the mass ΔM_{pocket} of the zone where the mass fraction of *effective* ^{13}C is larger than 10^{-3} , the product $\beta \times H_P$ at the epoch of the maximum penetration of the convective envelope, the total mass ΣH of hydrogen left below the formal convective boundary at the same epoch and the total mass $\Sigma^{13}\text{C}_{\text{eff}}$ of *effective* ^{13}C within the pocket³. Fig. 5 illustrates the definitions of the various quantities reported in Table 2. ΔM_{TDU} and the masses of the effective ^{13}C for both metallicities are also plotted, as a function of β , in Fig. 6 and Fig. 7, respectively. The third dredge up occurs at lower core masses when a velocity profile is applied at the bottom of the convective envelope. Moreover, larger β values imply deeper

²The heavy vertical-dashed line indicates the location of the formal boundary of the convective envelope, as defined by means of the Schwarzschild criterion.

³The mass fraction of *effective* ^{13}C in a given mesh point is defined as $X_{13}^{\text{eff}} = X_{13} - X_{14} \frac{13}{14}$, where X_{13} and X_{14} are the mass fractions of ^{13}C and ^{14}N , respectively. Owing to its large neutron capture cross section, ^{14}N is the most efficient neutron poison, so that the s-process nucleosynthesis is significantly depressed where it becomes comparable to the ^{13}C . For this reason, we define the mass of the ^{13}C pocket as the mass of the zone where $X_{13}^{\text{eff}} > 10^{-3}$ (see Fig. 5).

TDU. On the contrary, the total amount of ^{13}C in the pocket shows a maximum at $\beta = 0.1$. Note that the pocket practically disappears for the largest β value, reflecting the fact that when enough H is mixed into the transition zone, the CN cycle goes to the equilibrium and ^{14}N , rather than ^{13}C , is produced. For $\beta = 0.1$, the effective ^{13}C masses are 7.4×10^{-6} and $5.5 \times 10^{-6} M_{\odot}$, at $Z=0.0138$ and $Z=0.0001$, respectively. These values are close to the standard one adopted by Gallino et al. (1998), namely $4 \times 10^{-6} M_{\odot}$ ⁴. Gallino et al. (1998) showed how this choice of the ^{13}C -pocket allows the buildup of the main and the strong components, *i.e.* the distribution of s-elements from the Sr-Y-Zr peak up to the Pb-Bi peak in the solar system, whilst other works (Busso et al. 2001; Abia et al. 2001, 2002) argue that a certain spread of the effective ^{13}C mass is required in order to reproduce the heavy elements overabundances in a large sample of Galactic C(N type) stars. More recently, Bisterzo et al. (2008) confirm the need for such a spread, extending their analysis to CEMP stars. It is worth to note that whilst Gallino et al. (1998) assume a constant effective ^{13}C mass, in our models we find a characteristic evolution of the ^{13}C pocket (see Fig. 8). In particular, a maximum mass of ^{13}C is attained after very few thermal pulses (2 or 3); later on, the pocket progressively shrinks, in mass, until it disappears during the late part of the AGB evolution (see next section). Nevertheless, the success of the post-process calculations in reproducing a large amount of observational data concerning AGB stars (Lambert et al. 1995; Busso et al. 1995; Abia et al. 2001, 2002), their progeny on the post-AGB (Reyniers et al. 2007), Galactic evolution of s process elements (Travaglio et al. 1999, 2001, 2004) and the isotopic composition of C-rich pre-solar grains (SiC) (Zinner et al. 2006a; Lugaro et al. 1999) suggests to adopt β values allowing the formation of ^{13}C pocket whose average size is similar to the ST case. On the other hand, as shown in Fig. 7, only values of β close to 0.1 provide enough *effective* ^{13}C . For this reason, in all the computation here presented we have adopted $\beta = 0.1$ (but see § 7 for further

⁴ This amount of ^{13}C is often referred as the ST (*standard*) case for low mass AGB nucleosynthesis models.

remarks).

Let us come back to the differences between our mixing scheme and the one adopted by Herwig et al. (1997). Basing on a few additional models computed by using a diffusion algorithm instead of our linear mixing, we have verified that in this case the extension in mass of the zone where the proton abundance left by the TDU is $10^{-3} < X < 10^{-2}$ cannot be larger than about $10^{-5} M_{\odot}$ (for any value of the β parameter)⁵. Instead, as shown in Fig. 5, when our mixing algorithm is adopted, the same region extends for a few $10^{-4} M_{\odot}$. Such a difference affects the total mass of the effective ^{13}C within the pocket, which may be about 20 times larger in the case of a linear mixing scheme (for comparisons, see Figure 4 in Herwig 2000). As a consequence, the resulting s-process yields are significantly reduced if a diffusive mixing is adopted. A further difference concerns the overshoot at the bottom of the convective zone generated by a thermal pulse. In our models, the exponential decline described by Eq. 1 switches off when, as in this case, the radiative gradient is equal to the adiabatic gradient at the convective border, so that $v_{bce}=0$. On the contrary, Herwig et al. (1997) force a certain overshoot below the base of this convective zone, in spite of the strong negative difference between the radiative and adiabatic gradient and the huge entropy barrier generated by the shell-He burning. This implies stronger thermal pulses and larger temperatures at the base of the He-rich intershell, thus increasing the efficiency of the s-process nucleosynthesis powered by the $^{22}\text{Ne}(\alpha,n)^{25}\text{Mg}$ reaction (see Lugaro et al. 2003).

A reliable (hydrodynamical) model of convection capable to describe the mixing across the boundaries of the major convective zones should provides a more realistic description of the AGB evolution and nucleosynthesis (for a recent attempt, see Meakin & Arnett 2007). On the other hand, comparisons between the predicted AGB nucleosynthesis and the abundances observed in AGB stars may be used to constrain the efficiency of convection. This is the approach we follow

⁵This is the range of hydrogen mass fraction required to produce enough *effective* ^{13}C . If $X > 10^{-2}$, ^{14}N rather than ^{13}C would be produced, while for $X < 10^{-3}$ too few ^{13}C is synthesized.

in the present paper.

4. Reference models at different metallicity

In this Section we present and compare 5 evolutionary sequences of AGB models having the same initial mass ($2 M_{\odot}$), but different initial composition, namely: $(Z; Y) = (0.0138; 0.269)$, $(0.006; 0.260)$, $(0.003; 0.260)$, $(0.001; 0.245)$, $(0.0001; 0.245)$. The mass is representative of low mass AGB stars and the five metallicities almost span the entire metal distribution of our Galaxy and of the extragalactic resolved stellar populations, like the Magellanic Clouds, M31 and several dwarf spheroidal galaxies. The most metal-rich model corresponds to the composition of the pre-solar nebula, as derived by means of an up-to-date standard solar model obtained by adopting the latest compilation of solar abundance ratios (Lodders 2003; see Piersanti et al. 2007 for more details). The 5 evolutionary tracks, from the pre-main sequence up to the end of the AGB, are reported in Fig. 9. The TP-AGB phase is characterized by large oscillations in luminosity, associated to the expansions and contractions powered by thermal pulses, and an evident red excursion that is the direct consequence of the formation of new molecular species taking place after the transition from O- to C-rich atmosphere.

In Fig. 10 we show the evolution, during the TP-AGB phase, of the positions, in mass coordinates, of the inner border of the convective envelope, of the location of the maximum energy production within the H-burning shell and of the location of the maximum energy production within the He-intershell, top to bottom line, respectively. The last 2 lines separate 3 main regions within the star: the innermost zone is the degenerate CO core, the intermediate one is the He intershell and the more external is the H-rich envelope. The evolution of the 3 lines mark the most important events occurring during the TP-AGB phase. Between two thermal pulses (interpulse phase), the H-burning shell advances in mass, while the He burning is practically off. Then, when the He intershell attains a critical mass, the He flash starts. After a few years, during which

the thermonuclear runaway occurs, a quiescent He burning settles in, while the H burning dies down. Later on, within about 1000 yr, the convective envelope penetrates the H-He discontinuity (third dredge up). Note that for a certain time during the interpulse, the line representing the maximum energy production within the He-intershell moves suddenly upwards. At that epoch, the 3α reactions are practically extinguished in the whole He intershell, but the temperature in the region occupied by the newly formed ^{13}C pocket is large enough ($T \sim 1.0 \times 10^8$ K) to ignite the $^{13}\text{C}(\alpha, n)^{16}\text{O}$ reaction and the consequent s process nucleosynthesis. Indeed, the ^{13}C burning releases about 5-10 MeV per reaction, depending on the energy of the consequent neutron capture on a seed nucleus. Note that this additional energy release has a negligible effect on the further physical evolution.

Table 3 reports some properties characterizing the 5 evolutionary sequences, namely (from left to right): the progressive number of the thermal pulse (n_{TP}), the total mass at the time of the onset of the thermal pulse (M_{Tot}), the corresponding mass of the H-exhausted core (M_{H})⁶, the mass of the H-depleted material dredged up (ΔM_{TDU}), the maximum mass of the convective zone generated by the TP (ΔM_{CZ}), the mass burnt by the H-shell during the previous interpulse period (ΔM_{H}), the overlap factor r (defined as the fraction of ΔM_{CZ} already included in the convective zone generated by the previous TP), the λ factor (defined as the ratio between ΔM_{TDU} and ΔM_{H}), the average number n_c of neutrons captured per initial iron seed nucleus during the radiative ^{13}C pocket burning, the duration of the interpulse period preceding the current TP (Δt_{ip}), the maximum temperature attained at the bottom of the convective zone generated by the TP (T_{MAX}), the surface metallicity after the dredge up (Z_{surf}) and the corresponding C/O ratio. Finally, the total mass of the material cumulatively dredged up during the whole evolutionary sequence is reported in the last row (M_{TDU}^{tot}).

As already discussed in Straniero et al. (2003), the TDU starts when the mass of the

⁶The corresponding envelope mass is simply: $M_{env} = M_{Tot} - M_{\text{H}}$.

H-exhausted core exceeds a critical value, whereas it ceases when the envelope mass, eroded by the mass loss, is reduced down to a critical value. In the five evolutionary sequences presented here, the first TDU episode takes place when (from $Z = 0.0138$ to $Z = 0.0001$) M_H is 0.560, 0.569, 0.576, 0.604, 0.641 M_\odot . Note that at the lowest metallicities ($Z = 0.001$ and 0.0001) a 2 M_\odot star already develops rather large core mass during the early-AGB, so that the third dredge up occurs almost soon after the beginning of the TP-AGB phase. At those metallicities, stars with smaller mass may experience TDU episodes at smaller M_H . The last TDU episode takes place when M_{env} is 0.534, 0.183, 0.207, 0.292, 0.242 M_\odot , for $Z = 0.0138, 0.006, 0.003, 0.001$ and 0.0001, respectively.

As discussed in § 3, the introduction of a smoothed profile of the convective velocities at the bottom of the envelope favors the occurrence of TDU at smaller core masses and enhances its efficiency, with respect to models where the bare Schwarzschild criterion is adopted (Straniero et al. 1997). As an example, in the 2 M_\odot model with $Z = 0.02$ of Straniero et al. (1997), the first TDU takes place when the core mass is 0.61 M_\odot and has a reduced efficiency with respect to the model presented here. A second reason at the base of these differences is the rate of the $^{14}\text{N}(p,\gamma)^{15}\text{O}$ reaction: we are currently using the most recent low-energy laboratory measurement of this rate by Imbriani et al. (2006), which is a factor of two lower with respect to the rate proposed by Caughlan & Fowler (1988) and Angulo et al. (1999). Being the $^{14}\text{N}(p,\gamma)^{15}\text{O}$ reaction the bottleneck of the CNO cycle, a lower rate implies a reduced H-burning efficiency, stronger TPs and larger TDUs, as already verified by Straniero et al. (2000) and confirmed by Herwig & Austin (2004).

An important quantity affecting the nucleosynthesis is the maximum temperature attained at the base of the convective zone generated by a TP. During the AGB evolution, this value progressively increases, reaches a maximum and, then, slightly decreases toward the last TP (Fig. 11, upper panel). In the most metal-rich model, T_{MAX} remains always below 3.0×10^8 K: this is due to the fact the H burning shell is efficient and, therefore, the TPs are weaker with respect to

lower metallicities (see Straniero et al. 2003). For that reason, in these models the $^{22}\text{Ne}(\alpha,n)^{25}\text{Mg}$ reaction is only marginally activated. On the contrary, in the two most metal-poor models, T_{MAX} attains higher values (up to 3.2×10^8 K), so that the $^{22}\text{Ne}(\alpha,n)^{25}\text{Mg}$ adds a significant contribution to the s process nucleosynthesis, in particular for the treatment of the branchings along the s-path. We will come back on this issue in the next Section.

Concerning ΔM_{TDU} , it depends non-linearly on the metallicity, the envelope mass and the core mass (see formula 3 in Straniero et al. 2003). Fixing the values of the other two parameters, it is generally larger at lower metallicity. It is also larger at larger envelope mass or/and core mass. During the AGB evolution, the core mass increases, while the envelope mass decreases, so that ΔM_{TDU} initially increases, following the growth of M_H , but then decreases, when the envelope erosion by mass loss is stronger. This is clearly showed in Fig. 11 (lower panel). Looking at the total mass of the material that is cumulatively dredged up, it has a minimum in the case of the most metal-rich evolutionary sequence ($\Delta M_{tot}^{TDU} = 3.62 \times 10^{-2} M_{\odot}$), whilst the maximum is attained at $Z = 0.001$ ($\Delta M_{tot}^{TDU} = 1.31 \times 10^{-1} M_{\odot}$). In § 5 we will show how the assumed mass loss rate affects this quantity.

The mass of the convective zone generated by a TP shrinks during the AGB evolution. In all of the 5 sequences, the last ΔM_{CZ} is about a factor of two smaller than the first. It is also a factor of two smaller at the lowest metallicity with respect to the largest one. On the contrary, the λ factor is smaller at larger metallicities, whilst the overlap (r factor) is similar in all the five sequences.

The $Z=0.0138$ sequence attains the C-star condition ($C/O > 1$) after 7 dredge up episodes and the final C/O is 1.88. More metal poor models becomes C-stars sooner and develop larger final C/O ratios: in the $Z=0.0001$ case, for example, the final C/O is 53. This is mainly due to the lower initial amount of O, rather than to the deeper dredge up.

5. Changing the mass loss and the mixing length efficiency.

In this Section we will show how the present theoretical scenario is affected by the assumed treatment of hydrodynamical phenomena, not explicitly included in the hydrostatic equations, such as mass loss and convection, whose efficiency in the models relies on some free parameters. For this purpose, we have calculated 2 additional evolutionary sequences, both at $Z=0.0001$. In the first one we have adopted a classical Reimers' formula ($\eta = 0.4$), up to the tip of the AGB, instead of that based on the calibrated mass loss-period-luminosity relation (see § 2). The second evolutionary sequence has been obtained by changing the value of the mixing length parameter ($\alpha = \Lambda/H_p$, where Λ is the mixing length) from 2.15, as required by the standard solar model (see Piersanti et al. 2007), to 1.8. The evolutions of T_{MAX} and ΔM_{TDU} for these two additional models are compared with the reference model in Fig. 12. Either the mass loss rate and the mixing length parameter are usually calibrated on stars with solar or nearly solar composition and little is known about the validity of these calibrations at low metallicity; for a discussion on the possible calibration of the mixing length at different Z see Chieffi et al. (1995) and Ferraro et al. (2006). The early TP-AGB evolution of the Reimers' model, which is mainly controlled by the growth of the H-exhausted core, is similar to the one obtained in the case of the reference model. However, when the envelope erosion becomes important, the two sequences depart from each other. In particular, as a consequence of the higher mass loss rate, the reference model terminates sooner. As a result, the Reimers' model experiences a larger number of TPs and third dredge-up episodes. The total mass cumulatively dredged up is $1.6 \times 10^{-1} M_{\odot}$, to be compared with $9.54 \times 10^{-2} M_{\odot}$ in the reference model (see Table 4).

The main effect of reducing the mixing length parameter is a smaller extension of the convective regions. As a consequence, the third dredge up is weaker and the temperature at the bottom of the convective zone powered by thermal pulses is lower (see Fig. 12). In this case the total mass cumulatively dredged up is just $6.13 \times 10^{-2} M_{\odot}$ (see Table 5).

The corresponding effects on the nucleosynthesis are discussed in § 6.5.

6. Nucleosynthesis in the He intershell

Let us start with the solar metallicity model. As noted in § 4, owing to the low temperature within the convective zones generated by the various TPs, the $^{22}\text{Ne}(\alpha, n)^{25}\text{Mg}$ reaction plays a marginal role as a neutron source at high metallicities, so that the most important nucleosynthesis site is the transition region between the core and the envelope, where the ^{13}C pocket forms. In Fig. 13 we report the mass fractions of selected isotopes in this zone, after the formation of the third pocket. Actually, three different "pockets" can be distinguished. The most internal one is the ^{13}C pocket (solid line), which is partially overlapped to a ^{14}N pocket (long dashed line). Note that the relevant s process nucleosynthesis occurs in the left (more internal) tail of the ^{13}C pocket, where the amount of ^{14}N , the major neutron poison, is low. The third and smallest pocket is made of ^{23}Na (short-long-dashed line). The latter forms where the abundance of ^{22}Ne (short-dashed line) is comparable to the ^{12}C abundance (dotted line), so that the $^{22}\text{Ne}(p, \gamma)^{23}\text{Na}$ reaction competes with the $^{12}\text{C}(p, \gamma)^{13}\text{N}$ in the proton capture game. As firstly suggested by Goriely & Mowlavi (2000), this ^{23}Na pocket may provide a significant contribution to the synthesis of sodium in AGB stars.

The most interesting result obtained by coupling stellar structure evolution and nucleosynthesis concerns the variations of the size of the 3 sub-pockets when the star climbs the Asymptotic Giant Branch. Fig. 14 and Fig. 15 show, for the solar metallicity model, the physical conditions in the core-envelope transition region at the time of the maximum penetration of the 3rd and of the 11th (*i.e.* the last) TDU, respectively. Solid and dashed lines represent the hydrogen and the ^{12}C profiles, respectively. The abundance curves in both figures have been shifted upward in order to match the pressure scale axis. The slanting dashed area shows the region of the fully convective envelope (as defined by the Schwarzschild criterion), whilst the horizontal and the vertical dashed

areas mark the regions where the ^{13}C and the ^{23}Na pockets will form later (the ^{14}N pocket, which overlaps with both the aforementioned pockets, is not reported in the plot for graphical reasons). Pressure and pressure scale height are also shown. Note as the pressure jump between the dense core and the loose envelope is definitely steeper in the case of the last TDU episode. In fact, when comparing the two physical structures, it comes out that the pressure of the H-exhausted core remains of the same order of magnitude, whilst the base of the envelope at the moment of the last TDU episode is more expanded with respect to the 3rd one, showing a pressure difference of about five orders of magnitude. In both cases, external convection penetrates down to a layer where the pressure is about 10^{11} dyne and H_P is about 10^{10} cm, but due to the steeper pressure gradient, the extension of the zone with a smoothed H profile is significantly reduced in the last TDU episode. In this case, the resulting pocket is definitely smaller. Table 6 lists the effective mass of ^{13}C for all the pockets produced in the $Z=0.0138$ and $Z=0.0001$ models. In the Table, we report (left to right): the mass of the H-exhausted core (M_{H}), the mass of effective ^{13}C in the pocket ($\Sigma^{13}\text{C}_{\text{eff}}$) and the mass extension of the pocket (ΔM). Note how the last pocket is more than one order of magnitude smaller than the first one.

The shrinkage of the ^{13}C pocket implies a progressive decrease of the s process efficiency as the star evolves along the AGB. For a long time, it has been assumed that the synthesis of the main component of the s process would require the partial superposition of different neutron exposures: Clayton (1961) showed that an exponential distribution of these exposures could reproduce the observed σN_s curve (see also Seeger et al. 1965). Ulrich (1973) noted that if the s process takes place at the base of the convective zone generated by a thermal pulse, the partial overlap of the recurrent convective zones provides, in a natural way, an exponential distribution of neutron exposures, thus reinforcing Clayton’s original suggestion. However, as argued by Gallino et al. (1998) (see also Straniero et al. 1995; Arlandini et al. 1999), when the s process occurs during the interpulse in the ^{13}C pocket, the scenario becomes more complex and cannot be described by a simple analytical function. Beside its relatively small thickness, the stratification of the ^{13}C

(and of the neutron poisons, as ^{14}N) within the pocket leads to stratified neutrons irradiations with different intensities. In addition to that, owing to the variation of the overall amount of ^{13}C available in the pocket, as we find in self-consistent evolutionary models of AGB stars, this stratification changes pulse by pulse. In particular, the first pockets, the largest ones, give a major contribution to the overall AGB nucleosynthesis compared with that of the smallest late pockets. This is illustrated in Fig. 16, where we report, for the solar metallicity model, the production factors, within the He intershell at the time of the 1st, 3rd, 6th and 11th TDU episodes, of nuclei whose synthesis is mainly ascribed to the s process (namely, nuclei whose s process contribution is larger than 80%)⁷. The s process nucleosynthesis occurs in the radiative ^{13}C pocket and leaves a thin layer highly enriched with heavy elements that is located in the middle of the He intershell. When the convection powered by the thermal pulse takes place, this material is spread out in the whole He intershell. In spite of the large dilution caused by the convective mixing⁸, the s-element overabundances in the He intershell rapidly increase during the first TPs. A maximum is attained at the 6th TP. At that time, in the He intershell the abundances of the s-only nuclei are on the average a factor of 500 larger than the initial ones (700 for the ls element and 300 for the hs elements). Later on, the production factors of the various s elements in the He intershell decrease. This is due to the shrinkage of the late pockets, which are no more able to compensate the convective dilution. Nevertheless, quite large overabundances are found in the He intershell up to the AGB tip, because of the partial overlap of the recurrent convective zones generated by the various TPs.

⁷The production factor is defined as N_j^s/N_j^\odot , where N_j^s is the abundance by number and N_j^\odot is the corresponding solar scaled abundance.

⁸Note that the mass of the largest pocket is only $6 \times 10^{-4} M_\odot$, while the convective zones attain about $3 \times 10^{-2} M_\odot$.

6.1. Evolution of the surface composition: the main and the strong s process components.

The variations of the surface composition after selected TDU episodes of the solar metallicity model are reported in Fig. 17. Looking at the elements beyond Fe ($Z=26$), the most abundant species are those corresponding to isotopes with particularly small neutron capture cross sections. In particular, the peaks corresponding to magic neutron numbers ($N=50, 82$ and 126) clearly emerge from the bulk production of the s process. In general, magic neutron nuclides act as bottlenecks of the s process. At solar metallicity, owing to the relatively large amount of iron seed, compared with the number of neutrons released by the radiative ^{13}C burning, the productions of the light, ls (Sr-Y-Zr), elements and the heavy, hs (Ba-La-Ce-Nd-Sm), elements, namely the first and the second s-peaks, are favored with respect to the lead production (the third s-peak). At the end of the AGB evolution, the surface ratios [hs/ls] and [Pb/hs] are -0.21 and -0.33 , respectively. This values are attained after a few TDU episodes, those following the first and largest ^{13}C pockets. Later on, the overabundances continue to grow, as a consequence of the TDU, but these ratios remain constant.

The final surface composition of the five models with different metallicity are shown in Fig. 18. Surface abundances after selected TDUs are shown in Table 7, Table 8, Table 9, Table 10 and Table 11. Only key elements are tabulated. Moreover, a selection of final elemental abundances, isotopic ratios and spectroscopic indexes are listed in Table 12⁹. The $^{13}\text{C}(\alpha,n)^{16}\text{O}$ reaction is primary-like (*i.e.* not directly affected by the metallicity of the pristine material), whilst the iron seeds scale with the metallicity. Thus, by lowering the metallicity, the number of neutron per seed nuclei progressively increases: this trend clearly results from column 9 of Table 3. Within the ^{13}C pockets, in fact, the average number n_c of neutrons captured per initial iron seed nucleus increases with the metallicity, starting from about 40 at solar metallicity up to

⁹The complete set of these Tables is available in the electronic version of this paper.

4000 at $Z = 0.0001$ ¹⁰. Therefore, the bulk of the s process nucleosynthesis first moves from ls elements to hs elements and, at low metallicities, it shifts directly to ²⁰⁸Pb, at the termination point of the s path. This behavior is well reproduced by our models (see Fig. 18). A second important change occurring at low Z concerns the second neutron source, the ²²Ne(α ,n)²⁵Mg. In low metallicity models, owing to the larger temperature attained at the inner border of the convective zone generated by the thermal pulse, a second neutron burst takes place, causing interesting changes in the He intershell composition. At variance with the nucleosynthesis in the ¹³C pocket, since the maximum temperature in the convective shell generated by a TP increases pulse by pulse (see Fig. 11), it is in the late part of the AGB that the major effects induced by the second neutron burst become important. Among them, we recall the overproduction of some neutron-rich isotopes. Owing to the larger neutron density (10^{11} cm⁻³ instead of 10^7 obtained in the case of the radiative ¹³C pocket), several interesting branchings along the s process path are activated. Thus, neutron-rich isotopes, whose production is otherwise prevented by β decays of lighter isotopes, can be produced. Table 13 reports some characteristic isotopic ratios sensitive to the neutron density. The tabulated ratios relate to the branchings occurring at ⁸⁵Kr, ⁸⁶Rb, ⁹⁵Zr, ¹³³Xe and ¹⁴¹Ce, respectively. As a comparison, solar ratios are also reported. Note how they increase when the metallicity decreases. In particular, the ⁸⁷Rb is underproduced at large metallicity with respect to the lighter ⁸⁵Rb, whereas it is overproduced at low Z . This is a direct consequence of the opening of the ⁸⁵Kr and ⁸⁶Rb branchings, taking place when the neutron density exceeds $10^8 - 10^9$ neutron/cm³ (see Malaney & Lambert 1988). Note that, since ⁸⁷Rb is a magic neutron nucleus, the overall production of Rb is significantly enhanced at low Z . As a result, the ratio of Rb and

¹⁰Note that n_c involves neutron captures on both light elements and heavy elements. Neutron captures on light elements act as neutron poisons, thus decreasing the number of neutrons available for the s-process nucleosynthesis. The major neutron poison, represented by the ¹⁴N(n,p)¹⁴C reaction, has already been considered in the estimate of n_c .

ls increases at low Z . For example, $\log(\text{Rb}/\text{Sr})$ is 0.33, 0.42, 0.53, 0.77 and 0.85 at $Z=0.0138$, 0.006, 0.003, 0.001 and 0.0001, respectively. In Fig. 19 we report the maximum neutron densities attained in the models at various metallicities. As stressed before, the lower the metallicity is, the higher the neutron density attained during the TP is.

6.2. Evolution of the surface composition: from C to Fe.

The most striking consequence of the third dredge up is the surface carbon enhancement. By reducing the metallicity, the maximum enhancement with respect to iron increases from $[\text{C}/\text{Fe}]=0.6$ ($Z=0.0138$ model) to $[\text{C}/\text{Fe}]=3$ ($Z=0.0001$ model). Obviously, this implies that the C/O ratio increases with decreasing the metallicity, passing from 1.87 at solar metallicity to 53 at $Z=0.0001$ (see Table 12). Our models do not show evidences for HBB, therefore at low metallicities we obtain large C/N ratios and large $^{12}\text{C}/^{13}\text{C}$ isotopic ratios. Note that possible reduction of these ratios due to deep-mixing processes (as the CBP) is not explicitly considered in our models. Small enhancements of nitrogen are found, due to the dredge up of the thin region of incomplete H burning. Almost all the ^{14}N left by the H burning in the He intershell is converted into ^{22}Ne during the thermal pulse phase, through the chain $^{14}\text{N}(\alpha, \gamma)^{18}\text{F}(\beta^+ \nu)^{18}\text{O}(\alpha, \gamma)^{22}\text{Ne}$. The ^{22}Ne plays a fundamental role, particularly in metal-poor stars. It acts as a neutron source, as a poison and, at very low Z , as a seed capable to counterbalance the scarcity of iron (see Gallino et al. 2006). Note that at low Z , most of the ^{22}Ne is primary: at $Z=0.0001$, in fact, the amount of carbon in the envelope largely exceeds the pristine C+N+O since the first TDU episode. As a result, at the end of the AGB the amount of ^{22}Ne in the He intershell is comparable with that found in the same region of the solar metallicity model. Correspondingly, the surface abundance of neon is significantly enhanced (see Table 12). Despite the very low neutron capture cross section, the large abundance of ^{22}Ne allows the production of light isotopes like Na, Mg and Al. Sodium is further enhanced, because of the already mentioned formation of the ^{23}Na pocket,

due to protons capture in the most external layer of the core-envelope transition zone. At solar metallicity, the majority of the Na overproduction is due to the ingestion of the ^{23}Na pocket at the time of the TDU. At $Z=0.0001$, in addition to that, neutron captures on ^{22}Ne taking place in the radiative ^{13}C pocket and during the thermal pulse account for 13% and 35% of the total Na production, respectively (Cristallo et al. 2006).

Concerning O, it is only marginally affected by the internal nucleosynthesis at large Z . In low metallicity models, the oxygen enhancements results larger ($[\text{O}/\text{Fe}]=1$ at $Z=0.0001$) because of the reduced initial ^{16}O abundance. We recall that we have assumed a solar scaled initial composition, so that $[\text{O}/\text{Fe}]$ is nearly 0 at the beginning of the AGB for all the models here presented. Thus, in order to compare theoretical O overabundances to those measured in C-enhanced stars belonging to the Galactic halo (CEMP), one has to add an initial overabundance of, at least, 0.4 – 0.5 dex.

Among the light elements, ^{19}F is produced at all metallicities, with a significant production at the lowest one. Fluorine is synthesized by the $^{15}\text{N}(\alpha, \gamma)^{19}\text{F}$ reaction in the convective zone generated by a thermal pulse. The ^{15}N production is due to the $^{18}\text{O}(\text{p}, \alpha)^{15}\text{N}$ reaction: therefore, the ^{19}F production requires the simultaneous presence of ^{18}O and protons (see, e.g., Forestini et al. 1992). In the He intershell, protons are available in the radiative ^{13}C pocket and at the beginning of a thermal pulse (see, e.g., Lugaro et al. 2004), released by the $^{14}\text{N}(\text{n}, \text{p})^{14}\text{C}$ reaction: neutrons are therefore required for a consistent production of ^{15}N .

In the radiative ^{13}C pocket neutrons are produced by the $^{13}\text{C}(\alpha, \text{n})^{16}\text{O}$ reaction, while ^{18}O is synthesized by means of the $^{14}\text{C}(\alpha, \gamma)^{18}\text{F}(\beta^- \nu)^{18}\text{O}$ chain.

Few neutrons are also available at the beginning of a thermal pulse: they come from the burning of the ^{13}C left by the H-burning shell in the upper zone of the He intershell. This ^{13}C remains unburned during the interpulse and is engulfed in to the convective zone generated by the TP. The ^{13}C burns in a convective environment producing neutrons, which are almost totally captured by the (still abundant) ^{14}N , giving rise to a certain release of protons. At that time, the temperature

at the bottom of the convective shell is not high enough for a complete ^{18}O depletion, therefore ^{15}N is efficiently produced. The $^{22}\text{Ne}(\alpha, n)^{25}\text{Mg}$ reaction (which is the main source of neutrons during a TP) does not contribute to the fluorine nucleosynthesis because, when it takes place, the temperature is so high that no ^{14}N and too few ^{18}O survive in the convective shell. In summary, we have two main channels for the ^{15}N production in the He intershell. At solar metallicity, the two sources equally contribute to the fluorine production; at low metallicities, the ^{15}N accumulated in the radiative ^{13}C pocket is the main source of fluorine, because the ^{13}C left by the full CNO burning is rather low for the major part of the AGB lifetime (but see § 6.5).

6.3. Yields

One of the aims of this paper is to provide a complete and uniform set of AGB yields, comprehensive of all chemical species, starting from hydrogen up to the Pb-Bi s process ending point. Yields of selected isotopes at different metallicities are reported in Table 14: being the number of considered isotopes too large to provide it in a paper format, a constantly updated database of AGB yields is available on the web ¹¹ and in the electronic version of this paper. According to Tinsley (1980), the yield is:

$$M_y(k) = \int_0^{\tau(M_i)} [X(k) - X^0(k)] \frac{dM}{dt} dt \quad (2)$$

where dM/dt is the mass loss rate, while $X(k)$ and $X^0(k)$ stand for the current and the initial mass fraction of the isotope k , respectively. Yields are given in solar mass units. We recall that our calculation have been stopped after the last TDU episode, when the residual envelope mass is of the order of $(0.2 \div 0.5) M_\odot$. Except for the natural decay of the eventually surviving unstable isotopes, the envelope composition is freezed after this moment. Then, in computing the yields, we assume that the star loses the whole residual envelope through a single mass loss episode.

¹¹http://www.oa-teramo.inaf.it/osservatorio/personale/cristallo/data_online.html.

6.4. Short-lived radioactive isotopes.

In this Section we discuss the synthesis of a few short-lived radioactive isotopes, namely ^{26}Al , ^{36}Cl , ^{41}Ca , ^{60}Fe , ^{107}Pd and ^{205}Pb . The present theoretical predictions for low mass AGB stars may be used to interpret the evidence for the presence of these radioactive isotopes in the early solar system (ESS, see Wasserburg et al. 2006 for a review on short-lived radioactive from AGB stars) and in pre-solar dust grains (Zinner et al. 2006b). Moreover, ^{26}Al and ^{60}Fe are particularly important in the field of γ -ray astronomy (Diehl 2006): their detection from selected AGB sources could be possible in the next future by means of γ -rays instruments mounted on high-energy astronomical satellites. Let us start from these two short-lived isotopes.

The ground state of ^{26}Al has a terrestrial half-life of 7.16×10^5 yr, which is comparable to the duration of the whole TP-AGB phase of a low mass star. ^{26}Al is produced in the H-burning shell by proton captures on ^{25}Mg . Within the H-depleted (and ^{26}Al -rich) region, we need to distinguish two zones: the upper one, which extends from the tip of the convective shell generated by a TP up to the H-shell, and the lower one, which is engulfed in the convective shell. In the former region ^{26}Al survives and is dredged up to the surface, whilst in the latter one, owing to its large neutron-capture cross section, it is easily destroyed by neutron captures. This happens in radiative conditions within the ^{13}C -pockets and, more importantly, within the convective TPs. As a matter of fact, when the temperature at the bottom of the convective shell exceeds 2.7×10^8 K, ^{26}Al is easily destroyed. In our solar metallicity model, this condition is attained toward the end of the TP-AGB phase, so that part of the ^{26}Al engulfed in the convective shells is preserved. This is not the case of the low metallicity models, where the ^{22}Ne neutron source is efficient since the first TP (see Table 14). In that case, only the ^{26}Al in the upper part of the He intershell (not engulfed in the convective shell) survives and is dredged up to the surface.

The synthesis of ^{60}Fe during the radiative ^{13}C burning is limited, owing to the relatively fast β decay of ^{59}Fe (half-life 45 days). However, the higher neutron density generated by the convective

^{22}Ne burning allows to open the ^{59}Fe branching, leading to the production of ^{60}Fe . This explains the relatively large ^{60}Fe yield obtained in low metallicity models. The yield is higher at $Z=0.001$ than at $Z=0.0001$, because of the larger total dredged up mass.

A different production channel is active in the metal-rich models ($Z = 0.0138$, $Z = 0.006$ and $Z = 0.003$). The appearance at the surface of ^{60}Fe occurs after the first TDU episode. This reflects a peculiarity of the first ^{13}C pocket of these models: the temperature developed in the pocket during the interpulse is not large enough to fully consume ^{13}C before the onset of the following thermal pulse (Cristallo et al. 2006). Then, a certain amount of unburned ^{13}C is engulfed into the convective zone generated by the TP and is rapidly burned at higher temperature. The resulting neutron densities are rather large (more than 10^{11} cm^{-3}). In Fig. 19, we mark with an arrow the neutron peak corresponding to the ingestion of the first ^{13}C pocket into the convective shell generated by the following TP (this fact occurring for the metal-rich models only). Although the effect of this anomalous convective ^{13}C burning on the overall s process nucleosynthesis is negligible, some neutron-rich isotopes as, for example, ^{60}Fe , preserve the signature of such a peculiar event. Note that the surface isotopic ratio $^{60}\text{Fe}/^{56}\text{Fe}$ we obtain in the solar metallicity model (namely 4.0×10^{-5}) is about 10 times higher than the value reported by Wasserburg et al. (2006), as obtained by means of a post-process calculation, where the effect of the peculiar first ^{13}C pocket was not considered.

Let us finally discuss the production of the short-lived radioactive isotopes ^{36}Cl , ^{41}Ca , ^{107}Pd and ^{205}Pb , whose traces have been found in the ESS and whose origin can be ascribed to an AGB star. Concerning ^{41}Ca , an equilibrium value ($^{41}\text{Ca}/^{40}\text{Ca} \sim 10^{-2}$) is rapidly attained whenever a neutron source is activated: this value is inversely proportional to the ratio of the corresponding neutron capture cross sections. ^{107}Pd and ^{205}Pb are mainly synthesized during the standard radiative ^{13}C burning at any metallicity. The variations of the total yields of these two short-lived nuclei with the metallicity mainly reflect the increase of the neutron exposure when the metallicity decreases (because the number of neutrons per iron seed increases). This is only partially counterbalanced

by the larger dredged up mass.

As a general remark, since the decay rates depend on the environmental conditions (temperature and electron density), the use of stellar models, which follow the temporal evolution of these conditions in detail and in all the layers where radioactive isotopes are stored after their production, is mandatory. Such a warning should be seriously considered, particularly, when these isotopes are engulfed in convective zones where the temperature and the density vary considerably from the the bottom to the top. As an example, ^{205}Pb has a rather long terrestrial half-life (1.5×10^7 yr), but at the temperature of the He intershell of an AGB star its half-life is several order of magnitude shorter (Takahashi & Yokoi 1987). The faster decays occurring in radiative conditions during the time elapsed between the thermal pulse and the TDU (about 10^3 yr) significantly affects the resulting surface abundances of ^{205}Pb (see also Mowlavi et al. 1998).

In Table 15, we list the final surface abundances (by mass fraction) of the aforementioned short-lived radioactive isotopes (with the corresponding stable isotopes), at different metallicities.

6.5. Changing the mass loss and the mixing length efficiency: effects on the nucleosynthesis.

In § 5 we have shown how the physical parameters of the AGB evolutions depends on the choices of the mass loss rate and the mixing length efficiency. In this Section we discuss the corresponding effects on the nucleosynthesis. The results are illustrated in Fig. 20 and Table 16.

The final overabundances (with respect to iron) of the Reimers model are generally larger than those found in the reference model. This is a consequence of the larger duration of the AGB, as obtained when the mass loss rate is lower, so that the total dredged up mass is larger. On the average, the abundances of the s-elements increase by a factor of two, while for the light elements we found a variation in the range between +0.2 dex (carbon) and +0.5 dex (magnesium).

Concerning the fluorine production, we note that the delayed end of the AGB phase favors the second fluorine source even in low Z models (see § 6.2). The primary ^{13}C in the ashes of the H burning becomes, in the late TP-AGB phase of low Z models, as large as the ^{13}C found in the reference model with solar metallicity. As explained before, neutrons released by the burning of this ^{13}C at the beginning of each TP provide an additional channel for the production of ^{15}N . As a result, a longer AGB phase, as obtained by reducing the mass loss rate, favors this fluorine source, at any Z . Although the absolute abundances depend on the mass loss rate, the abundance ratios are less sensitive to the AGB duration. It occurs because the bulk of the s process nucleosynthesis has to be ascribed to the first ^{13}C pockets, the largest ones, so that a freeze out of the abundance ratios takes place after very few TPs in the He intershell material (see § 6.1). For this reason, the [hs/lr] and [Pb/hs] obtained in the case of the Reimers model are very similar to those of the reference model. Interestingly, the final C/N and $^{12}\text{C}/^{13}\text{C}$ isotopic ratios of the Reimers model decrease with respect to the reference one (where monotonic trends are found), even if HBB is not at work. This different behavior, which appears in the late AGB phase, is due to an increase with the core mass of the temperature at the bottom of the convective envelope during TDU episodes, which leads to a partial H-burning. During these phases, therefore, mixing and burning simultaneously occur. This phenomenon, already found by Goriely & Siess (2004) in a model with initial mass $M = 3 M_{\odot}$ and $Z = 0.0001$, enhances the ^{13}C and the ^{14}N in the envelope more rapidly than ^{12}C (which, in any case, increases after each TDU episode). When applying a velocity profile at the base of the convective envelope, in fact, protons are mixed to higher temperatures with respect to the ones attained when using the bare Schwarzschild criterion. A more detailed analysis of this phenomenon, based on models with different initial masses, will be presented in a forthcoming paper.

Finally, we evaluated the effects of varying the mixing efficiency by reducing the mixing-length parameter (case $\alpha = 1.8$). In that case, the lower cumulative dredged up mass leads to smaller overabundances. As in the Reimers model, the elemental ratios, which are sensitive to the

metallicity and to the ^{13}C mass in the pocket, are less affected by the structural model change.

7. Conclusion

This paper reports the first systematic calculation of low mass AGB models at different metallicities, in which the physical evolution of the star is coupled to a full nuclear network, from H to Bi. The major input physics, such as nuclear reaction rates, radiative opacity, mass loss rate, have been revised, in order to provide a reliable set of theoretical stellar yields.

The [hs/ls] and the [Pb/hs] ratios at different Z provide important hints about the nucleosynthesis occurring at different metallicities and represent useful tools to verify the goodness of our theoretical models, when compared with observational data. As shown in Table 12, the [hs/ls] is rather low at large Z , because the low number of neutron per seed limits the production of heavy s elements. When decreasing the metallicity, this ratio increases, achieving a sort of saturation for $Z < 0.001$. Below this threshold, the scarcity of seeds (essentially Fe) is partially compensated by a reduction of the mass of the ^{13}C pocket (see below). [Pb/hs] provides a more sensitive spectroscopic index to test low metallicity models. It is expected to monotonically increase from high to low Z , indeed. Let us stress that, since the [hs/ls] and the [Pb/Fe] are practically frozen after a few dredge up episodes, these indexes are almost independent of the assumed mass loss rate and on the efficiency of the TDU, which are two of the most uncertain quantities in AGB modelling. In practice, as noted by Busso et al. (2001) (see also Gallino et al. 2008; Bisterzo et al. 2008), they essentially depend on the effective ^{13}C mass within the ^{13}C pockets. In this context, by comparing the theoretical predictions of these indexes with spectroscopic ratios at different Z , we may have a direct check of the validity of our choice of the β parameter.

In Fig. 21 we have reported the observed [hs/ls] indexes, as measured in a sample of Galactic

and extragalactic C-stars with different metallicities (Abia et al. 2002, 2008; de Laverny et al. 2006). Spectroscopic and photometric studies indicate that these stars are intrinsic (N type) C-stars, *i.e.* low-mass AGB stars undergoing the third dredge up. The agreement with our theoretical predictions is comfortable. In particular, data confirm the increase of [hs/ls], when the metallicity is reduced below the solar value, up to a plateau attained at intermediate Z . Only the most metal-poor C(N) star of the sample, namely ALW-C7, a carbon star of the Carina dwarf galaxy, shows a too large [hs/ls] compared with the low Z plateau. However, as suggested by Abia et al. (2008), this star shows a particularly low abundance of Zr compared with other light s elements. Moreover, the fitting process in determining the ls abundances in ALW-C7 resulted more difficult with respect to ALW-C6, making the determination of the [hs/ls] even more uncertain (C. Abia, personal communication).

A second interesting check for the new theoretical scenario concerns the comparison with nucleosynthesis models based on post-processes calculations (Gallino et al. 2008; Bisterzo et al. 2008). In the post-process calculations, the relevant stellar parameters are derived according to older stellar evolutionary models (Straniero et al. 1997) and, where models were not available, by using the interpolation formulas provided by Straniero et al. (2003). Since these models have been computed by assuming a Reimers mass loss rate, the duration of the AGB and, in turn, the total mass of H-depleted and s-enriched material dredged up is larger than that found in the present computations. Although this difference affects the predicted overabundance of a single element, it has negligible effects on the [hs/ls] or the [Pb/hs] indexes. A second important difference of the post process calculations concerns the mass of the ^{13}C pocket, which is fixed to a constant value for the full AGB evolution; according to Gallino et al. (1998), the value of the ^{13}C mass is a free parameter of the nucleosynthesis model and the ST (standard) case corresponds to $\Sigma^{13}\text{C}_{\text{eff}} = 4 \times 10^{-6} M_{\odot}$ (see the discussion in § 3). The third important difference concerns the chemical profiles of ^{13}C and ^{14}N within the pocket (for the post process calculation see Fig. 1 of Gallino et al. 1998). In Fig. 22, the various lines represent the results of the post-process

calculations (Gallino et al. 2008; Bisterzo et al. 2008), whilst the filled squares are our new predictions. In the plot, ST refers to the standard case, whilst the cases labelled with ST*k or ST/k correspond to ^{13}C pockets whose mass is k and $1/k$ times the standard one, respectively. At large metallicities, our predictions for $[\text{hs}/\text{ls}]$ and $[\text{Pb}/\text{hs}]$ are in good agreement with those of the ST case (dotted lines). When the metallicity is reduced, however, the two spectroscopic indexes resulting from the new calculation move progressively toward the lines corresponding to smaller ^{13}C masses. This behavior is likely due to the smaller ^{13}C pockets we found at low Z (see Fig. 8 and Tab. 6), whose effect is to limit the maximum neutron exposure.

Let us conclude with a comment on the question of the spread of the ^{13}C pocket. As discussed by Bisterzo et al. (2008), a certain spread is required to explain the variety of $[\text{hs}/\text{ls}]$ observed in the available sample of carbon-enhanced metal-poor and s -rich stars (CEMPs), whose overabundance of heavy elements is supposed to be originating from mass transfer from an ancient AGB companion (extrinsic C-stars). Similar conclusions arise from the abundance analysis of Barium stars, which may be considered the CEMPs homologous at intermediate Z (Husti & Gallino 2008; Husti et al. 2008). By limiting our consideration to the Galactic (N type) carbon stars, those belonging to the disk of the Milky Way and having a nearly-solar metallicity, for which a quite large sample of $[\text{hs}/\text{ls}]$ is now available, we note that the dispersion around the average value, namely $\langle[\text{hs}/\text{ls}]\rangle = -0.19 \pm 0.3$, is of the same order of magnitude of the error bar of a single measurement (± 0.25). In addition to that, it should be noted that the prediction of our solar metallicity model, namely $[\text{hs}/\text{ls}] = -0.21$, is in excellent agreement with the measured average value. It should be recalled that the present models refer to only one AGB mass ($2 M_{\odot}$). The natural variation of the stellar parameters among stars with similar metallicity, as for example the mass or the initial He, C, N or O, may account for a certain spread in the observed $[\text{hs}/\text{ls}]$ and $[\text{Pb}/\text{hs}]$ ratios. In the next future, we will extend the theoretical database to investigate such a possibility.

SC, OS and RG are supported by the Italian MIUR-PRIN 2006 Project "Final Phases of Stellar Evolution, Nucleosynthesis in Supernovae, AGB stars, Planetary Nebulae". ID is supported by the spanish MEC project AYA2005-08013-C03-03 and by the andalusian FQM-292. MTL has been supported by the Austrian Academy of Sciences (DOC programme) and acknowledges funding by the Austrian Research Fund FWF (project P-18171). We gratefully thank Carlos Abia for many enlightening discussions.

REFERENCES

- Abbondanno, U., et al., 2004, *Phys. Rev. Lett.*, 93, 1103
- Abia, C., Busso, M., Gallino, R., Domínguez, I., Straniero, O., & Isern, J., 2001, *ApJ*, 559, 1117
- Abia, C., et al., 2002, *ApJ*, 579, 817
- Abia, C., de Laverny, P., & Wahlin, R., 2008, *A&A*, 481, 161
- Angulo, C., et al., 1999, *Nucl. Phys. A*, 656, 3
- Aringer, B., 2000, Ph.D. thesis, University of Vienna
- Arlandini, C., Käppeler, F., Wisshak, K., Gallino, R., Lugaro, M., Busso, M., & Straniero, O., 1999, *ApJ*, 525, 886
- Beers, T.C.: 1999, *ASP. Conf. Ser.*, 165, 202
- Bisterzo, S., et al., 2008, *PASA*, in press
- Busso, M., Lambert, D. L., Beglio, L., Gallino, R., Raiteri, C. M., & Smith, V. V., 1995, *ApJ*, 446, 775
- Busso, M., Gallino, R., Lambert, D.L., Travaglio, C., & Smith, V.V., 2001, *ApJ*, 557, 802
- Castellani, V., Giannone, P., & Renzini, A., 1971, *Ap&SS*, 10, 340
- Caughlan, G.R., & Fowler, W.D., 1988, *Atomic Data Nucl. Data Tables*, 40, 283
- Chieffi, A., Straniero, O., & Salaris, M., 1995, *ApJ*, 445, L39
- Chieffi, A., Limongi, M., & Straniero, O., 1998, *ApJ*, 502, 737
- Chieffi, A., Domínguez, I., Limongi, M., & Straniero, O., 2001, *ApJ*, 554, 1159

- Christlieb, N., 2003, *Rev. Mod. Astron.*, 16, 191
- Clayton, D.D., Fowler, W.A., Hull, T. E., & Zimmerman, B. A., 1961, *Ann. Phys.*, 12, 331
- Cox, J.P., & Giuli, R.T., 1968, *Principles of Stellar Structure*, Gordon & Breach Publ., New York
- Cristallo, S., Gallino, R., Straniero, O., Piersanti, L., & Domínguez, I., 2006, *Mem. Soc. Astron. Italiana*, 77, 774
- Cristallo, S., Straniero, O., Lederer, M.T., & Aringer, B., 2007, *ApJ*, 667, 489
- de Laverny, P., et al., 2006, *A&A*, 446, 1107
- Diehl, R., 2006, *New A Rev.*, 50, 534
- Domínguez, I., Abia, C., Straniero, O., Cristallo, S., & Pavlenko, Ya.V., 2004, *A&A*, 422, 1045
- Ferraro, F., Valenti, E., Straniero, O., & Origlia, L., 2006, *ApJ*, 642, 225
- Forestini, M., Goriely, S., Jorissen, A., & Arnould, M., 1992, *A&A*, 261, 157
- Freytag, B., Ludwig, H.-G., & Steffen, M., 1996, *A&A*, 313, 497
- Gallino, R., et al., 1998, *ApJ*, 497, 388
- Gallino, R., Bisterzo, S., Husti, L., Käppeler, F., Cristallo, S., & Straniero, O. , 2006, *Proceedings of the "International Symposium on Nuclear Astrophysics - Nuclei in the Cosmos - IX"*, *Proceedings of Science*, POS 100
- Gallino, R., Bisterzo, S., & Husti, L., 2008, *AIP Conf. Proceedings*, 1001, 123
- Goriely, S. & Mowlavi, N., 2000, *A&A*, 362, 599
- Goriely, S. & Siess, L., 2004, 421, L25
- Görres, J., et al., 2000, *Phys. Rev. C*, 62, 055801

- Groenewegen, M.A.T., et al., 2007, MNRAS, 376, 313
- Herwig, F., Blöcker, T., Schönberner, D., & El Eid, M., 1997, A&A, 324, L81
- Herwig, F., 2000, A&A, 360, 952
- Herwig, F., & Austin, S.M., 2004, ApJ, 613, L73
- Heil, M., et al., 2008, ApJ, 673, 434
- Husti, L., & Gallino, R., 2008, AIP Conf. Proceedings, 1001, 139
- Husti, L., et al., 2008, PASA, in press
- Iben, I.Jr., 1973, ApJ, 185, 209
- Imbriani, G., et al., 2006, EPJA, 24, 455
- Jaeger, M., et al., 2001, Phys. Rev. Lett., 87, 2501
- Lagadec, E., & Zijlstra, A.A., 2008, MNRAS, 390, 59L
- Lambert, D.L., Smith, V.V., Busso, M., Gallino, R., & Straniero, O., 1995, ApJ, 450, 302
- Lebzelter, T., Lederer, M. T., Cristallo, S., Hinkle, K. H., Straniero, O., & Aringer, B., 2008, A&A, 486, 511
- Lederer, M.T., & Aringer, B., 2008, A&A, in press (arxiv 0810.5672)
- Lodders, K., 2003, ApJ, 591, 1220
- Lugaro, M., Zinner, E., Gallino, R., & Amari, S., 1999, ApJ, 527, 369L
- Lugaro, M., Herwig, F., Lattanzio, J.C., Gallino, R., & Straniero, O., 2003, ApJ, 586, 1305
- Lugaro, M., Ugalde, C., Karakas, A., Görres, J., Wiescher, M., Lattanzio, J.C., & Cannon, R.C., 2004, ApJ, 615, 934

- Karakas, A., & Lattanzio, J.C., 2007, PASA, 24, 103
- Malaney, R.A., & Lambert, D.L., 1988, MNRAS, 235, 695
- Marigo, P.: 2002, A&A, 387, 507
- Matsuura, M., et al., 2008, AIP Conf. Proceedings, 1016, 383
- Meakin, C.A., & Arnett, D., 2007, ApJ, 667, 448
- Mowlavi, N., Goriely, S., & Arnould, M., 1998, A&A, 330, 206
- Nollett, K.M., Busso, M., & Wasserburg, G.J., 2003, ApJ, 582, 1036
- Patronis, N., et al. , 2004, Phys. Rev. Lett., 69, 025803
- Piersanti, L., Straniero, O., & Cristallo, S., 2007, A&A, 462, 1051
- Reyniers, M., Abia, C., van Winckel, H., Lloyd Evans, T., Decin, L., Eriksson, K., & Pollard, K.R., 2007, A&A, 461, 641 R
- Schwarzschild, M., & Härm, R., 1965, ApJ, 142, 855
- Seeger, P.A., Fowler, W.A., & Clayton, D.D., 1965, ApJS, 11, 121
- Smith, V.V., & Lambert, D.L., 1986, ApJ, 311, 843
- Straniero, O., Gallino, R., Busso, M., Chieffi, A., Limongi, M., & Salaris, M., 1995, ApJ, 440, L85
- Straniero, O., Chieffi, A., Limongi, M., Gallino, R., Busso, M., & Arlandini, C., 1997, ApJ, 478, 332
- Straniero, O., Limongi, M., Chieffi, A., Domínguez, I., Busso, M., & Gallino, R., 2000, Mem. Soc. Astron. Italiana, 71, 719

- Straniero, O., Domínguez, I., Cristallo, S., & Gallino, R., 2003, PASA, 20, 389
- Straniero, O., Gallino, R., & Cristallo, S., 2006, Nucl. Phys. A, 777,311
- Sugimoto, D., 1971, Prog. Theor. Phys., 45, 761
- Takahashi, K., & Yokoi, K., 1987, Atomic Data Nucl. Data Tables, 36, 375
- Tinsley, B.M., 1980, Fund. Cosmic Phys., 5, 287
- Travaglio, C., Galli, D., Gallino, R., Busso, M., Ferrini, F., & Straniero, O., 1999, ApJ, 521, 691
- Travaglio, C., Gallino, R., Busso, M., & Gratton, R., 2001, ApJ, 549, 346
- Travaglio, C., Gallino, R., Arnone, E., Cowan, J., Jordan, F., & Sneden, C., 2004, ApJ, 601, 864
- Ulrich, R.K., 1973, in *Explosive Nucleosynthesis*, eds. Schramm D.N. & Arnett W.D., (Austin: University Texas Press), 139.
- Vassiliadis, E., & Wood, P.R., 1993, ApJ, 413, 641
- Wasserburg, J.J., Busso, M., Gallino, R., & Nollett, K.M., Nucl. Phys. A, 777, 5
- Weigert, A., 1966, ZAp, 64, 395
- Zinner, E., et al., 2006, ApJ, 650, 320
- Zinner, E., et al., Nittler, L.R., Alexander, C.M.O'D., & Gallino, R., 2006, New A Rev., 50, 574

Table 1. The C- and N-enhancement factors for the H-rich opacity tables at various metallicities. $f=1$ corresponds to $[C/Fe]=0$ and $[N/Fe]=0$. For each metallicity, a routine for the calculation of the opacity coefficients interpolates on a 25 elements matrix, as originated by the the possible combination of the five C-enhancement and five N-enhancement factors.

Z	enhancement factor (f)				
0.0138	1	1.5	1.8	2.2	4
0.0060	1	2	5	10	50
0.0030	1	2	5	10	50
0.0010	1	5	10	50	200
0.0001	1	10	100	500	2000

Table 2. Variation with β of the ^{13}C pocket.

β	$\Delta M_{TDU} [M_{\odot}]$	λ	$\Delta M_{pocket} [M_{\odot}]$	$\beta \times H_P [\text{cm}]$	$\Sigma\text{H} [M_{\odot}]$	$\Sigma^{13}\text{C}_{\text{eff}} [M_{\odot}]$
Z=0.0138 (3rd Pulse followed by TDU)						
0	0.00E+00
0.01	0.00E+00
0.05	3.00E-04	0.04	9.40E-05	5.62E+08	4.37E-05	8.32E-07
0.075	1.15E-03	0.14	3.47E-04	8.82E+08	8.49E-05	3.12E-06
0.09	1.70E-03	0.20	7.66E-04	1.06E+09	9.56E-05	6.41E-06
0.10	2.50E-03	0.28	5.54E-04	1.22E+09	1.18E-04	7.38E-06
0.11	2.90E-03	0.32	2.54E-04	1.36E+09	1.29E-04	4.40E-06
0.125	4.10E-03	0.43	2.00E-05	1.61E+09	1.76E-04	8.80E-07
0.15	5.80E-03	0.58	1.00E-05	2.00E+09	2.04E-04	1.42E-07
0.20	7.90E-03	0.75	0.00E+00	2.73E+09	1.96E-04	0.00E+00
Z=0.0001 (2nd Pulse followed by TDU)						
0	1.90E-03	0.29
0.01	2.80E-03	0.39	7.00E-06	5.16E+07	2.01E-05	5.55E-08
0.05	3.32E-03	0.45	6.50E-05	3.10E+08	2.35E-05	6.07E-07
0.075	3.63E-03	0.45	3.14E-04	5.28E+08	4.01E-05	2.31E-06
0.09	3.81E-03	0.45	6.10E-04	5.44E+08	5.48E-05	4.65E-06
0.10	3.90E-03	0.51	5.44E-04	6.19E+08	6.63E-05	5.48E-06
0.125	4.59E-03	0.57	8.40E-05	1.05E+09	1.49E-04	5.61E-07
0.15	5.15E-03	0.65	0.00E+00	1.37E+09	1.72E-04	0.00E+00
0.20	6.12E-03	0.75	0.00E+00	1.72E+09	2.07E-04	0.00E+00

Table 2—Continued

β	ΔM_{TDU} [M_{\odot}]	λ	ΔM_{pocket} [M_{\odot}]	$\beta \times H_P$ [cm]	ΣH [M_{\odot}]	$\Sigma^{13}\text{C}_{\text{eff}}$ [M_{\odot}]
---------	----------------------------------	-----------	-------------------------------------	-------------------------	----------------------------	--

Table 3. Evolution of selected physical parameters of the 5 reference models.

n_{TP}^a	M_{Tot}^b	M_H^b	ΔM_{TDU}^b	ΔM_{CZ}^b	ΔM_H^b	r	λ	n_c	Δt_{ip}^c	T_{MAX}^d	Z_{surf}	C/O
Z=0.0138 Y=0.269												
-2	1.91E+00	5.48E-01	0.00E+00	3.25E-02	4.20E-03	8.99E-01	0.00E+00	...	14.0	2.20	1.39E-02	0.31
-1	1.90E+00	5.53E-01	0.00E+00	3.07E-02	4.80E-03	8.66E-01	0.00E+00	...	16.5	2.27	1.39E-02	0.31
1	1.89E+00	5.60E-01	2.00E-04	3.12E-02	7.00E-03	7.90E-01	2.90E-02	4.2×10^1	18.6	2.46	1.39E-02	0.31
2	1.88E+00	5.68E-01	1.20E-03	2.94E-02	7.90E-03	7.48E-01	1.52E-01	4.6×10^1	18.6	2.53	1.41E-02	0.34
3	1.86E+00	5.76E-01	2.50E-03	2.81E-02	9.00E-03	6.95E-01	2.78E-01	4.3×10^1	17.8	2.62	1.46E-02	0.43
4	1.84E+00	5.83E-01	3.70E-03	2.69E-02	9.90E-03	6.46E-01	3.74E-01	4.3×10^1	17.0	2.69	1.53E-02	0.57
5	1.82E+00	5.90E-01	4.50E-03	2.58E-02	1.07E-02	6.00E-01	4.21E-01	3.9×10^1	16.2	2.75	1.62E-02	0.75
6	1.78E+00	5.96E-01	4.90E-03	2.48E-02	1.10E-02	5.67E-01	4.45E-01	3.6×10^1	15.3	2.80	1.72E-02	0.95
7	1.72E+00	6.03E-01	4.90E-03	2.37E-02	1.11E-02	5.40E-01	4.41E-01	3.2×10^1	14.3	2.84	1.82E-02	1.15
8	1.63E+00	6.09E-01	4.80E-03	2.25E-02	1.10E-02	5.23E-01	4.36E-01	3.2×10^1	13.2	2.87	1.92E-02	1.35
9	1.51E+00	6.15E-01	4.40E-03	2.14E-02	1.07E-02	5.09E-01	4.11E-01	3.0×10^1	12.1	2.90	2.03E-02	1.57
10	1.35E+00	6.21E-01	3.80E-03	2.03E-02	1.03E-02	5.02E-01	3.69E-01	2.9×10^1	11.0	2.91	2.14E-02	1.78

Table 3—Continued

n_{TP}^a	M_{Tot}^b	M_H^b	ΔM_{TDU}^b	ΔM_{CZ}^b	ΔM_H^b	r	λ	n_c	Δt_{ip}^c	T_{MAX}^d	Z_{surf}	C/O
11	1.16E+00	6.26E-01	1.25E-03	1.91E-02	9.70E-03	5.00E-01	1.29E-01	2.4×10 ¹	9.91	2.92	2.19E-02	1.88
12	9.80E-01	6.33E-01	0.00E+00	1.71E-02	8.05E-03	5.31E-01	0.00E+00	2.2×10 ¹	8.30	2.87	2.19E-02	1.88
M_{TDU}^{tot}			3.62E-02									
Z=0.0060 Y=0.260												
-2	1.97E+00	5.55E-01	0.00E+00	3.32E-02	4.70E-03	8.82E-01	0.00E+00	...	15.9	2.27	6.07E-03	0.29
-1	1.97E+00	5.61E-01	0.00E+00	3.20E-02	6.30E-03	8.21E-01	0.00E+00	...	20.3	2.42	6.07E-03	0.29
1	1.96E+00	5.69E-01	1.60E-03	3.06E-02	7.90E-03	7.58E-01	2.03E-01	8.6×10 ¹	20.9	2.55	6.29E-03	0.40
2	1.95E+00	5.77E-01	3.40E-03	2.91E-02	9.50E-03	6.87E-01	3.58E-01	8.6×10 ¹	20.4	2.65	6.91E-03	0.69
3	1.93E+00	5.85E-01	5.30E-03	2.80E-02	1.09E-02	6.25E-01	4.86E-01	8.5×10 ¹	19.6	2.74	7.91E-03	1.15
4	1.91E+00	5.91E-01	6.70E-03	2.70E-02	1.20E-02	5.68E-01	5.58E-01	8.3×10 ¹	18.8	2.82	9.13E-03	1.70
5	1.89E+00	5.97E-01	7.30E-03	2.60E-02	1.28E-02	5.19E-01	5.70E-01	8.3×10 ¹	17.7	2.87	1.04E-02	2.27
6	1.86E+00	6.03E-01	7.60E-03	2.50E-02	1.29E-02	4.93E-01	5.89E-01	8.0×10 ¹	16.5	2.90	1.18E-02	2.85

Table 3—Continued

n_{TP}^a	M_{Tot}^b	M_H^b	ΔM_{TDU}^b	ΔM_{CZ}^b	ΔM_H^b	r	λ	n_c	Δt_{ip}^c	T_{MAX}^d	Z_{surf}	C/O
7	1.81E+00	6.08E-01	7.60E-03	2.40E-02	1.29E-02	4.71E-01	5.89E-01	7.8×10^1	15.3	2.93	1.31E-02	3.42
8	1.75E+00	6.13E-01	7.40E-03	2.30E-02	1.27E-02	4.59E-01	5.83E-01	7.5×10^1	14.1	2.96	1.45E-02	3.99
9	1.66E+00	6.18E-01	7.10E-03	2.20E-02	1.22E-02	4.58E-01	5.82E-01	7.2×10^1	12.9	2.99	1.58E-02	4.56
10	1.55E+00	6.23E-01	6.50E-03	2.10E-02	1.18E-02	4.45E-01	5.51E-01	7.1×10^1	11.9	3.00	1.72E-02	5.13
11	1.40E+00	6.28E-01	5.50E-03	1.98E-02	1.14E-02	4.34E-01	4.82E-01	6.8×10^1	10.8	3.00	1.87E-02	5.71
12	1.21E+00	6.33E-01	4.50E-03	1.87E-02	1.06E-02	4.45E-01	4.25E-01	6.6×10^1	9.68	3.00	2.02E-02	6.35
13	1.00E+00	6.38E-01	1.50E-03	1.75E-02	9.60E-03	4.60E-01	1.56E-01	6.6×10^1	8.47	2.99	2.11E-02	6.67
14	8.27E-01	6.44E-01	7.00E-04	1.54E-02	7.80E-03	5.04E-01	9.00E-02	5.3×10^1	6.91	2.92	2.17E-02	6.91
M_{TDU}^{tot}			7.27E-02									
Z=0.0030 Y=0.260												
-2	1.98E+00	5.63E-01	0.00E+00	2.92E-02	2.30E-03	9.62E-01	0.00E+00	...	10.4	2.09	3.04E-03	0.28
-1	1.98E+00	5.69E-01	0.00E+00	3.16E-02	5.80E-03	8.33E-01	0.00E+00	...	17.7	2.41	3.04E-03	0.28

Table 3—Continued

n_{TP}^a	M_{Tot}^b	M_H^b	ΔM_{TDU}^b	ΔM_{CZ}^b	ΔM_H^b	r	λ	n_c	Δt_{ip}^c	T_{MAX}^d	Z_{surf}	C/O
1	1.97E+00	5.76E-01	1.30E-03	2.97E-02	7.20E-03	7.67E-01	1.81E-01	1.6×10^2	20.1	2.54	3.21E-03	0.45
2	1.96E+00	5.84E-01	3.60E-03	2.82E-02	9.10E-03	6.86E-01	3.96E-01	1.7×10^2	19.8	2.66	3.88E-03	1.09
3	1.94E+00	5.91E-01	5.20E-03	2.72E-02	1.06E-02	6.13E-01	4.91E-01	1.7×10^2	19.1	2.77	4.92E-03	2.02
4	1.92E+00	5.98E-01	6.80E-03	2.62E-02	1.19E-02	5.56E-01	5.71E-01	1.6×10^2	18.2	2.85	6.17E-03	3.09
5	1.90E+00	6.04E-01	7.40E-03	2.53E-02	1.25E-02	5.07E-01	5.92E-01	1.6×10^2	17.1	2.89	7.51E-03	4.18
6	1.88E+00	6.09E-01	7.80E-03	2.43E-02	1.29E-02	4.72E-01	6.05E-01	1.4×10^2	15.9	2.94	8.87E-03	5.25
7	1.85E+00	6.14E-01	8.00E-03	2.34E-02	1.30E-02	4.52E-01	6.15E-01	1.4×10^2	14.7	2.97	1.02E-02	6.29
8	1.82E+00	6.19E-01	7.90E-03	2.24E-02	1.29E-02	4.37E-01	6.12E-01	1.4×10^2	13.6	3.00	1.16E-02	7.30
9	1.77E+00	6.24E-01	7.50E-03	2.15E-02	1.23E-02	4.30E-01	6.10E-01	1.4×10^2	12.5	3.03	1.29E-02	8.28
10	1.71E+00	6.28E-01	7.30E-03	2.06E-02	1.20E-02	4.23E-01	6.08E-01	1.3×10^2	11.6	3.04	1.43E-02	9.24
11	1.62E+00	6.33E-01	7.00E-03	1.98E-02	1.18E-02	4.14E-01	5.93E-01	1.3×10^2	10.7	3.05	1.57E-02	10.2
12	1.52E+00	6.37E-01	6.40E-03	1.89E-02	1.13E-02	4.12E-01	5.66E-01	1.3×10^2	9.86	3.05	1.71E-02	11.2
13	1.38E+00	6.41E-01	5.40E-03	1.80E-02	1.07E-02	4.14E-01	5.05E-01	1.3×10^2	9.05	3.06	1.86E-02	12.1
14	1.22E+00	6.46E-01	4.30E-03	1.70E-02	9.90E-03	4.22E-01	4.34E-01	1.3×10^2	8.16	3.06	2.01E-02	13.1
15	1.03E+00	6.51E-01	3.00E-03	1.59E-02	9.20E-03	4.32E-01	3.26E-01	1.2×10^2	7.29	3.04	2.17E-02	14.0

Table 3—Continued

n_{TP}^a	M_{Tot}^b	M_H^b	ΔM_{TDU}^b	ΔM_{CZ}^b	ΔM_H^b	r	λ	n_c	Δt_{ip}^c	T_{MAX}^d	Z_{surf}	C/O
16	8.63E-01	6.56E-01	6.00E-04	1.46E-02	8.00E-03	4.58E-01	7.50E-02	1.2×10^2	6.15	3.00	2.22E-02	14.4
M_{TDU}^{tot}			8.95E-02									
Z=0.0010 Y=0.245												
-1	1.94E+00	6.00E-01	0.00E+00	2.36E-02	2.20E-03	9.55E-01	0.00E+00	...	6.48	2.13	1.01E-03	0.25
1	1.93E+00	6.04E-01	2.00E-04	2.53E-02	4.70E-03	8.23E-01	4.30E-02	4.3×10^2	12.6	2.47	1.03E-03	0.31
2	1.92E+00	6.11E-01	3.00E-03	2.41E-02	6.70E-03	7.31E-01	4.48E-01	4.9×10^2	15.1	2.64	1.56E-03	1.85
3	1.91E+00	6.17E-01	5.40E-03	2.33E-02	8.80E-03	6.27E-01	6.14E-01	4.6×10^2	15.0	2.79	2.63E-03	4.56
4	1.89E+00	6.22E-01	7.20E-03	2.28E-02	1.06E-02	5.36E-01	6.79E-01	4.6×10^2	14.7	2.90	4.05E-03	7.64
5	1.88E+00	6.27E-01	8.50E-03	2.23E-02	1.19E-02	4.72E-01	7.14E-01	4.6×10^2	14.2	2.98	5.64E-03	10.6
6	1.85E+00	6.31E-01	9.30E-03	2.19E-02	1.26E-02	4.27E-01	7.38E-01	4.6×10^2	13.6	3.03	7.31E-03	13.3
7	1.83E+00	6.35E-01	9.70E-03	2.14E-02	1.31E-02	3.94E-01	7.40E-01	4.5×10^2	13.0	3.08	9.01E-03	15.9
8	1.81E+00	6.38E-01	9.70E-03	2.09E-02	1.31E-02	3.78E-01	7.40E-01	4.2×10^2	12.2	3.11	1.07E-02	18.3

Table 3—Continued

n_{TP}^a	M_{Tot}^b	M_H^b	ΔM_{TDU}^b	ΔM_{CZ}^b	ΔM_H^b	r	λ	n_c	Δt_{ip}^c	T_{MAX}^d	Z_{surf}	C/O
9	1.78E+00	6.41E-01	9.70E-03	2.03E-02	1.29E-02	3.70E-01	7.52E-01	3.9×10^2	11.5	3.15	1.24E-02	20.5
10	1.75E+00	6.44E-01	9.50E-03	1.97E-02	1.27E-02	3.58E-01	7.48E-01	3.9×10^2	10.8	3.16	1.41E-02	22.5
11	1.71E+00	6.47E-01	9.20E-03	1.91E-02	1.25E-02	3.51E-01	7.36E-01	3.8×10^2	10.1	3.18	1.58E-02	24.4
12	1.66E+00	6.50E-01	8.80E-03	1.85E-02	1.20E-02	3.51E-01	7.33E-01	3.8×10^2	9.46	3.18	1.74E-02	26.2
13	1.61E+00	6.53E-01	8.40E-03	1.79E-02	1.17E-02	3.48E-01	7.18E-01	3.8×10^2	8.83	3.18	1.91E-02	27.8
14	1.53E+00	6.56E-01	8.00E-03	1.72E-02	1.13E-02	3.50E-01	7.08E-01	3.8×10^2	8.24	3.19	2.08E-02	29.4
15	1.45E+00	6.59E-01	7.30E-03	1.66E-02	1.08E-02	3.50E-01	6.76E-01	3.9×10^2	7.65	3.18	2.26E-02	30.9
16	1.34E+00	6.61E-01	6.40E-03	1.58E-02	1.02E-02	3.56E-01	6.27E-01	3.9×10^2	7.06	3.17	2.44E-02	32.3
17	1.22E+00	6.65E-01	5.30E-03	1.50E-02	9.50E-03	3.68E-01	5.58E-01	3.8×10^2	6.46	3.17	2.62E-02	33.7
18	1.09E+00	6.68E-01	3.70E-03	1.41E-02	8.70E-03	3.82E-01	4.25E-01	3.8×10^2	5.83	3.13	2.80E-02	34.9
19	9.64E-01	6.72E-01	2.00E-03	1.31E-02	7.50E-03	4.11E-01	2.67E-01	3.8×10^2	5.14	3.10	2.96E-02	36.0
M_{TDU}^{tot}			1.31E-01									

Z=0.0001 Y=0.245

Table 3—Continued

n_{TP}^a	M_{Tot}^b	M_H^b	ΔM_{TDU}^b	ΔM_{CZ}^b	ΔM_H^b	r	λ	n_c	Δt_{ip}^c	T_{MAX}^d	Z_{surf}	C/O
-1	1.98E+00	6.34E-01	0.00E+00	1.83E-02	2.50E-03	9.19E-01	0.00E+00	...	4.21	2.19	1.01E-04	0.25
1	1.98E+00	6.41E-01	1.80E-03	1.96E-02	4.30E-03	7.97E-01	4.19E-01	4.6×10^3	9.50	2.55	3.36E-04	7.76
2	1.97E+00	6.45E-01	3.90E-03	1.90E-02	6.30E-03	6.78E-01	6.19E-01	5.1×10^3	10.0	2.72	1.02E-03	20.4
3	1.96E+00	6.49E-01	5.40E-03	1.86E-02	8.00E-03	5.77E-01	6.75E-01	5.4×10^3	9.75	2.85	2.06E-03	28.1
4	1.95E+00	6.53E-01	6.70E-03	1.83E-02	9.20E-03	5.08E-01	7.28E-01	4.9×10^3	9.58	2.95	3.31E-03	32.1
5	1.93E+00	6.56E-01	7.60E-03	1.80E-02	1.01E-02	4.51E-01	7.52E-01	4.6×10^3	9.35	3.03	4.67E-03	35.0
6	1.92E+00	6.59E-01	8.00E-03	1.77E-02	1.06E-02	4.09E-01	7.55E-01	4.4×10^3	9.06	3.07	6.08E-03	37.5
7	1.90E+00	6.62E-01	8.20E-03	1.74E-02	1.08E-02	3.84E-01	7.59E-01	4.2×10^3	8.74	3.12	7.52E-03	40.0
8	1.88E+00	6.65E-01	8.50E-03	1.70E-02	1.09E-02	3.67E-01	7.80E-01	3.9×10^3	8.37	3.16	8.96E-03	42.2
9	1.85E+00	6.67E-01	8.60E-03	1.67E-02	1.11E-02	3.45E-01	7.75E-01	3.9×10^3	8.01	3.19	1.04E-02	44.3
10	1.80E+00	6.70E-01	8.50E-03	1.63E-02	1.10E-02	3.32E-01	7.73E-01	3.9×10^3	7.62	3.22	1.19E-02	46.2
11	1.73E+00	6.72E-01	8.10E-03	1.58E-02	1.09E-02	3.21E-01	7.43E-01	3.9×10^3	7.22	3.23	1.33E-02	47.9
12	1.62E+00	6.75E-01	7.50E-03	1.53E-02	1.04E-02	3.28E-01	7.21E-01	3.7×10^3	6.82	3.24	1.49E-02	49.5
13	1.46E+00	6.77E-01	6.90E-03	1.48E-02	1.00E-02	3.34E-01	6.90E-01	3.7×10^3	6.39	3.24	1.65E-02	51.1

Table 3—Continued

n_{TP}^a	M_{Tot}^b	M_H^b	ΔM_{TDU}^b	ΔM_{CZ}^b	ΔM_H^b	r	λ	n_c	Δt_{ip}^c	T_{MAX}^d	Z_{surf}	C/O
14	1.20E+00	6.80E-01	4.90E-03	1.41E-02	9.50E-03	3.38E-01	5.16E-01	3.2×10^3	5.92	3.23	1.83E-02	52.5
15	9.25E-01	6.83E-01	7.50E-04	1.28E-02	8.15E-03	3.64E-01	9.20E-02	2.9×10^3	5.11	3.17	1.90E-02	53.1
M_{TDU}^{tot}			9.54E-02									

^aPulse number (negative values correspond to TP not followed by TDU)

^b M_\odot

^c 10^4 yr

^d 10^8 K

Table 4. Evolution of selected parameters for the Reimers ($\eta = 0.4$) model at $Z=10^{-4}$.

n_{TP}^a	M_{Tot}^b	M_H^b	ΔM_{TDU}^b	ΔM_{CZ}^b	ΔM_H^b	r	λ	n_c	Δt_{ip}^c	T_{MAX}^d	Z_{surf}	C/O
$Z=0.0001$ $Y=0.245$ Reimers $\eta = 0.4$												
-1	1.98E+00	6.34E-01	0.00E+00	1.83E-02	2.50E-03	9.19E-01	0.00E+00	...	4.21	2.19	1.01E-04	0.25
1	1.98E+00	6.41E-01	1.80E-03	1.96E-02	4.30E-03	7.97E-01	4.19E-01	4.6×10^3	9.50	2.55	3.36E-04	7.76
5	1.93E+00	6.56E-01	7.60E-03	1.80E-02	1.01E-02	4.51E-01	7.52E-01	4.0×10^3	9.35	3.03	4.67E-03	35.0
9	1.84E+00	6.70E-01	8.30E-03	1.63E-02	1.06E-02	3.38E-01	7.83E-01	3.7×10^3	7.60	3.22	1.18E-02	46.1 ⁵
14	1.75E+00	6.79E-01	7.00E-03	1.46E-02	9.60E-03	3.26E-01	7.29E-01	3.7×10^3	5.92	3.25	1.71E-02	51.5
18	1.66E+00	6.88E-01	5.60E-03	1.29E-02	8.30E-03	3.39E-01	6.75E-01	3.6×10^3	4.79	3.25	2.18E-02	54.7
25	1.50E+00	7.07E-01	3.20E-03	1.02E-02	6.50E-03	3.70E-01	4.92E-01	3.5×10^3	3.45	3.19	2.84E-02	57.7
32	1.35E+00	7.31E-01	3.00E-04	7.74E-03	4.30E-03	4.28E-01	7.00E-02	3.0×10^3	2.19	3.08	3.14E-02	58.6
M_{TDU}^{tot}			1.60E-01									

^aPulse number (negative values correspond to TP not followed by TDU)

^b M_{\odot}

Table 4—Continued

n_{TP}^a	M_{Tot}^b	M_H^b	ΔM_{TDU}^b	ΔM_{CZ}^b	ΔM_H^b	r	λ	n_c	Δt_{ip}^c	T_{MAX}^d	Z_{surf}	C/O
$^c 10^4 \text{ yr}$												
$^d 10^8 \text{ K}$												

Table 5. Evolution of selected parameters for the low mixing length ($\alpha_{m.l.} = 1.8$) model at $Z=10^{-4}$.

n_{TP}^a	M_{Tot}^b	M_H^b	ΔM_{TDU}^b	ΔM_{CZ}^b	ΔM_H^b	r	λ	n_c	Δt_{ip}^c	T_{MAX}^d	Z_{surf}	C/O
Z=0.0001 Y=0.245 $\alpha_{m.l.} = 1.8$												
-1	1.98E+00	6.35E-01	0.00E+00	1.81E-02	2.10E-03	9.52E-01	0.00E+00	...	3.67	2.13	1.01E-04	0.25
1	1.98E+00	6.39E-01	9.00E-04	1.97E-02	4.20E-03	8.15E-01	2.14E-01	4.6×10^3	8.94	2.50	1.63E-04	2.37
2	1.97E+00	6.44E-01	2.60E-03	1.88E-02	5.80E-03	7.08E-01	4.48E-01	4.7×10^3	9.62	2.66	5.86E-04	13.0
3	1.96E+00	6.49E-01	3.95E-03	1.81E-02	7.10E-03	6.24E-01	5.56E-01	5.1×10^3	8.70	2.77	1.30E-03	22.5
4	1.95E+00	6.53E-01	4.70E-03	1.76E-02	8.05E-03	5.54E-01	5.84E-01	4.9×10^3	8.19	2.86	2.20E-03	27.3
5	1.94E+00	6.57E-01	5.40E-03	1.71E-02	8.60E-03	5.10E-01	6.28E-01	4.6×10^3	7.80	2.92	3.21E-03	30.7
6	1.93E+00	6.60E-01	5.70E-03	1.66E-02	8.90E-03	4.72E-01	6.40E-01	4.6×10^3	7.44	2.98	4.28E-03	33.3
7	1.92E+00	6.63E-01	5.90E-03	1.61E-02	9.10E-03	4.44E-01	6.48E-01	4.6×10^3	7.09	3.02	5.38E-03	35.6
8	1.89E+00	6.67E-01	6.00E-03	1.57E-02	9.10E-03	4.28E-01	6.59E-01	4.5×10^3	6.75	3.05	6.49E-03	37.7
9	1.86E+00	6.70E-01	5.90E-03	1.52E-02	9.10E-03	4.10E-01	6.48E-01	4.5×10^3	6.41	3.08	7.61E-03	39.6
10	1.80E+00	6.73E-01	5.80E-03	1.48E-02	9.00E-03	4.03E-01	6.44E-01	4.5×10^3	6.08	3.10	8.74E-03	41.4
11	1.71E+00	6.76E-01	5.50E-03	1.43E-02	8.80E-03	3.97E-01	6.25E-01	4.5×10^3	5.75	3.12	9.89E-03	43.0

Table 5—Continued

n_{TP}^a	M_{Tot}^b	M_H^b	ΔM_{TDU}^b	ΔM_{CZ}^b	ΔM_H^b	r	λ	n_c	Δt_{ip}^c	T_{MAX}^d	Z_{surf}	C/O
12	1.59E+00	6.79E-01	4.70E-03	1.38E-02	8.50E-03	3.92E-01	5.53E-01	3.9×10^3	5.42	3.13	1.10E-02	44.5
13	1.41E+00	6.82E-01	3.10E-03	1.32E-02	8.00E-03	4.01E-01	3.87E-01	3.9×10^3	5.04	3.12	1.15E-02	45.1
14	1.19E+00	6.86E-01	1.10E-03	1.21E-02	7.10E-03	4.21E-01	1.55E-01	3.5×10^3	4.54	3.08	1.19E-02	45.6
M_{TDU}^{tot}			6.13E-02									

^aPulse number (negative values correspond to TP not followed by TDU)

^b M_\odot

^c 10^4 yr

^d 10^8 K

Table 6. Evolution of the ^{13}C pockets for $Z=0.0138$ and $Z=0.0001$. We report the mass of the H-exhausted core (M_{H}), the mass of the effective ^{13}C in the pocket ($\Sigma^{13}\text{C}_{\text{eff}}$) and the mass extension of the pocket (ΔM_{pocket}).

$N.$	$Z=0.0138$			$Z=0.0001$		
	M_{H}^a	$\Sigma^{13}\text{C}_{\text{eff}}^a$	$\Delta M_{\text{pocket}}^b$	M_{H}^a	$\Sigma^{13}\text{C}_{\text{eff}}^a$	$\Delta M_{\text{pocket}}^b$
1	0.5600	8.19E-06	5.96	0.6405	6.35E-06	5.79
2	0.5677	7.81E-06	6.04	0.6450	6.84E-06	5.44
3	0.5755	7.38E-06	5.54	0.6491	6.06E-06	4.58
4	0.5829	6.41E-06	5.40	0.6529	5.33E-06	4.45
5	0.5899	5.56E-06	5.09	0.6563	4.70E-06	4.35
6	0.5964	4.77E-06	4.33	0.6593	4.12E-06	3.96
7	0.6026	4.10E-06	4.01	0.6621	3.79E-06	3.79
8	0.6087	3.35E-06	3.35	0.6648	3.44E-06	3.74
9	0.6146	2.73E-06	2.81	0.6674	3.17E-06	3.29
10	0.6205	2.00E-06	1.99	0.6698	2.81E-06	2.82
11	0.6264	4.95E-07	0.71	0.6722	2.54E-06	2.60
12	0.6745	2.27E-06	2.51
13	0.6770	1.81E-06	1.88
14	0.6796	1.13E-06	1.31
15	0.6829	5.96E-07	0.73
TOT.		5.28E-05			5.50E-05	

^{a)} M_{\odot}

^{b)} $10^{-4} M_{\odot}$

Table 7. Elemental surface composition after selected TDUs of the $Z = 0.0138$ model. Key elements are tabulated.

[E/Fe]	TDU 1	TDU 4	TDU 7	TDU 11
C	-2.00E-01	6.72E-02	3.65E-01	5.75E-01
N	3.72E-01	3.71E-01	3.68E-01	3.65E-01
O	-5.16E-04	6.71E-04	2.43E-03	1.36E-03
F	-7.81E-03	7.03E-02	2.72E-01	4.88E-01
Ne	-2.55E-03	2.77E-02	1.03E-01	2.02E-01
Na	8.62E-02	9.87E-02	1.29E-01	1.72E-01
Mg	-1.92E-07	6.82E-04	3.59E-03	1.06E-02
Al	1.72E-04	1.76E-03	5.68E-03	1.06E-02
Sr	1.27E-06	4.13E-01	8.80E-01	1.11E+00
Y	-3.40E-07	4.05E-01	8.51E-01	1.08E+00
Zr	1.75E-08	3.95E-01	8.51E-01	1.07E+00
Ba	1.34E-06	3.95E-01	9.05E-01	1.10E+00
La	3.04E-06	3.42E-01	8.35E-01	1.02E+00
Ce	1.27E-06	2.87E-01	7.66E-01	9.51E-01
Pr	3.04E-07	1.72E-01	5.41E-01	7.14E-01
Nd	1.85E-06	1.90E-01	5.95E-01	7.69E-01
Sm	3.19E-07	9.80E-02	3.83E-01	5.30E-01
Eu	-1.83E-06	1.67E-02	8.93E-02	1.43E-01
Pb	-1.19E-07	5.36E-02	3.61E-01	5.43E-01

Note. — Table 7 is published in its entirety in the electronic edition of the *Astrophysical Journal*. A portion is shown here for guidance regarding its form and content.

Table 8. Elemental surface composition after selected TDUs of the $Z = 0.006$ model. Key elements are tabulated.

[El/Fe]	TDU 1	TDU 5	TDU 10	TDU 14
C	-9.26E-02	6.70E-01	1.03E+00	1.17E+00
N	3.94E-01	3.90E-01	3.83E-01	3.97E-01
O	-4.65E-04	1.50E-02	2.62E-02	2.90E-02
F	-8.65E-03	3.87E-01	8.51E-01	1.06E+00
Ne	4.94E-04	1.45E-01	4.09E-01	5.58E-01
Na	1.14E-01	1.52E-01	2.53E-01	3.58E-01
Mg	1.58E-04	6.57E-03	3.47E-02	6.77E-02
Al	5.90E-04	8.78E-03	2.04E-02	2.72E-02
Sr	4.65E-02	8.60E-01	1.22E+00	1.33E+00
Y	5.73E-02	8.72E-01	1.24E+00	1.36E+00
Zr	5.21E-02	9.18E-01	1.28E+00	1.39E+00
Ba	1.06E-02	1.40E+00	1.78E+00	1.87E+00
La	5.61E-03	1.43E+00	1.79E+00	1.88E+00
Ce	2.97E-03	1.48E+00	1.83E+00	1.91E+00
Pr	1.96E-03	1.23E+00	1.60E+00	1.69E+00
Nd	1.45E-03	1.34E+00	1.68E+00	1.76E+00
Sm	6.49E-04	1.09E+00	1.41E+00	1.49E+00
Eu	-1.52E-04	4.73E-01	7.39E-01	8.04E-01
Pb	3.05E-04	1.21E+00	1.54E+00	1.59E+00

Note. — Table 8 is published in its entirety in the electronic edition of the *Astrophysical Journal*. A portion is shown here for guidance regarding its form and content.

Table 9. Elemental surface composition after selected TDUs of the $Z = 0.003$ model. Key elements are tabulated.

[El/Fe]	TDU 1	TDU 6	TDU 11	TDU 16
C	-3.51E-02	1.06E+00	1.38E+00	1.54E+00
N	4.16E-01	4.12E-01	4.10E-01	4.38E-01
O	-1.42E-03	4.34E-02	7.14E-02	8.97E-02
F	-1.81E-02	7.27E-01	1.19E+00	1.47E+00
Ne	-8.52E-04	2.97E-01	6.36E-01	8.81E-01
Na	1.37E-01	2.05E-01	3.61E-01	5.70E-01
Mg	2.71E-04	1.72E-02	7.47E-02	1.70E-01
Al	8.66E-04	1.81E-02	3.21E-02	4.41E-02
Sr	4.20E-02	8.31E-01	1.12E+00	1.26E+00
Y	5.65E-02	8.66E-01	1.17E+00	1.33E+00
Zr	6.29E-02	9.17E-01	1.22E+00	1.38E+00
Ba	3.10E-02	1.51E+00	1.86E+00	2.01E+00
La	2.13E-02	1.56E+00	1.90E+00	2.05E+00
Ce	1.34E-02	1.67E+00	2.01E+00	2.15E+00
Pr	8.80E-03	1.46E+00	1.82E+00	1.98E+00
Nd	8.21E-03	1.57E+00	1.90E+00	2.04E+00
Sm	4.89E-03	1.34E+00	1.66E+00	1.80E+00
Eu	6.43E-04	6.79E-01	9.67E-01	1.10E+00
Pb	4.89E-04	2.02E+00	2.25E+00	2.32E+00

Note. — Table 9 is published in its entirety in the electronic edition of the *Astrophysical Journal*. A portion is shown here for guidance regarding its form and content.

Table 10. Elemental surface composition after selected TDUs of the $Z = 0.001$ model. Key elements are tabulated.

[El/Fe]	TDU 1	TDU 7	TDU 12	TDU 19
C	-2.13E-01	1.66E+00	1.95E+00	2.18E+00
N	4.59E-01	4.59E-01	4.72E-01	5.56E-01
O	-9.12E-03	1.59E-01	2.40E-01	3.22E-01
F	-3.85E-02	1.40E+00	1.83E+00	2.22E+00
Ne	-5.32E-03	7.21E-01	1.19E+00	1.60E+00
Na	1.67E-01	4.06E-01	7.69E-01	1.28E+00
Mg	9.40E-05	8.36E-02	3.27E-01	7.19E-01
Al	2.91E-03	7.65E-02	1.12E-01	1.79E-01
Sr	6.38E-06	7.94E-01	1.02E+00	1.26E+00
Y	2.56E-06	8.47E-01	1.11E+00	1.37E+00
Zr	2.56E-06	8.73E-01	1.14E+00	1.41E+00
Ba	5.06E-06	1.39E+00	1.70E+00	1.99E+00
La	2.56E-06	1.43E+00	1.74E+00	2.03E+00
Ce	6.55E-07	1.54E+00	1.87E+00	2.15E+00
Pr	-2.57E-06	1.38E+00	1.73E+00	2.02E+00
Nd	2.56E-06	1.44E+00	1.75E+00	2.04E+00
Sm	-4.37E-06	1.24E+00	1.57E+00	1.86E+00
Eu	-2.54E-05	6.10E-01	9.05E-01	1.18E+00
Pb	2.56E-06	2.54E+00	2.76E+00	2.87E+00

Note. — Table 10 is published in its entirety in the electronic edition of the *Astrophysical Journal*. A portion is shown here for guidance regarding its form and content.

Table 11. Elemental surface composition after selected TDUs of the $Z = 0.0001$ model. Key elements are tabulated.

[E/Fe]	TDU 1	TDU 5	TDU 10	TDU 15
C	1.15E+00	2.41E+00	2.81E+00	3.00E+00
N	4.93E-01	5.23E-01	6.17E-01	8.58E-01
O	-9.15E-04	5.95E-01	8.76E-01	1.01E+00
F	-8.31E-02	2.13E+00	2.62E+00	2.90E+00
Ne	-3.48E-03	1.30E+00	1.91E+00	2.27E+00
Na	2.22E-01	7.70E-01	1.40E+00	1.77E+00
Mg	-2.92E-04	2.31E-01	8.59E-01	1.30E+00
Al	7.02E-03	1.94E-01	4.37E-01	6.37E-01
Sr	1.19E-04	5.17E-01	8.64E-01	1.01E+00
Y	8.69E-06	5.66E-01	9.60E-01	1.12E+00
Zr	9.89E-06	5.75E-01	9.92E-01	1.17E+00
Ba	6.13E-05	9.21E-01	1.36E+00	1.55E+00
La	-4.48E-06	9.37E-01	1.38E+00	1.57E+00
Ce	2.41E-06	1.04E+00	1.49E+00	1.69E+00
Pr	-1.07E-04	9.01E-01	1.35E+00	1.55E+00
Nd	-4.98E-06	9.27E-01	1.37E+00	1.57E+00
Sm	-1.09E-04	7.40E-01	1.20E+00	1.41E+00
Eu	-4.44E-04	2.66E-01	5.87E-01	7.65E-01
Pb	9.70E-06	2.37E+00	2.74E+00	2.88E+00

Note. — Table 11 is published in its entirety in the electronic edition of the *Astrophysical Journal*. A portion is shown here for guidance regarding its form and content.

Table 12. Final surface composition of the 5 reference models at different Z . The final s process indexes, the C/O and the $^{12}\text{C}/^{13}\text{C}$ are given.

	$Z = 1.38 \times 10^{-2}$	$Z = 6.0 \times 10^{-3}$	$Z = 3.0 \times 10^{-3}$	$Z = 1.0 \times 10^{-3}$	$Z = 1.0 \times 10^{-4}$
[C/Fe]	0.57	1.17	1.54	2.17	3.00
[N/Fe]	0.37	0.40	0.44	0.56	0.86
[O/Fe]	0.00	0.03	0.09	0.32	1.01
[F/Fe]	0.49	1.06	1.46	2.22	2.90
[Ne/Fe]	0.20	0.56	0.88	1.60	2.27
[Na/Fe]	0.17	0.36	0.57	1.28	1.77
[Mg/Fe]	0.01	0.07	0.17	0.72	1.30
[Al/Fe]	0.01	0.03	0.04	0.18	0.64
[ls/Fe]	1.08	1.36	1.32	1.34	1.10
[hs/Fe]	0.87	1.78	2.00	2.01	1.56
[Pb/Fe]	0.54	1.59	2.32	2.87	2.88
[hs/ls]	-0.21	0.42	0.68	0.67	0.46
C/O	1.87	6.92	14.4	36.0	53.0
C/N	5.84	23.0	46.1	151.0	406.0
$^{12}\text{C}/^{13}\text{C}$	1.42×10^2	5.75×10^2	1.37×10^3	5.20×10^3	1.72×10^4

Note. — Table 12 is published in its entirety in the electronic edition of the *Astrophysical Journal*. A portion is shown here for guidance regarding its form and content.

Table 13. Selected surface branching isotopic ratios at different Z . The tabulated ratios relate to the branchings occurring at ^{85}Kr , ^{86}Rb , ^{95}Zr , ^{133}Xe and ^{141}Ce , respectively. Solar ratios are also reported.

Isot. ratio	\odot	$Z = 1.38 \times 10^{-2}$	$Z = 6.0 \times 10^{-3}$	$Z = 3.0 \times 10^{-3}$	$Z = 1.0 \times 10^{-3}$	$Z = 1.0 \times 10^{-4}$
$^{86}\text{Kr}/^{84}\text{Kr}$	0.31	0.26	0.37	0.52	0.68	0.72
$^{87}\text{Rb}/^{85}\text{Rb}$	0.39	0.40	0.58	0.94	1.32	1.30
$^{96}\text{Zr}/^{94}\text{Zr}$	0.16	0.03	0.07	0.16	0.44	0.61
$^{134}\text{Xe}/^{132}\text{Xe}$	0.37	0.07	0.06	0.13	0.47	0.71
$^{142}\text{Ce}/^{140}\text{Ce}$	0.13	0.01	0.01	0.04	0.14	0.20

Table 14. Yields (in M_{\odot}) of selected isotopes of the 5 reference models at different Z .

Isotope	$Z = 1.38 \times 10^{-2}$	$Z = 6.0 \times 10^{-3}$	$Z = 3.0 \times 10^{-3}$	$Z = 1.0 \times 10^{-3}$	$Z = 1.0 \times 10^{-4}$
^1H	-4.06E-02	-7.05E-02	-8.21E-02	-1.16E-01	-9.92E-02
^2H	-3.77E-05	-3.79E-05	-3.86E-05	-5.42E-05	-5.39E-05
^3He	3.77E-04	3.35E-04	3.03E-04	2.59E-04	1.83E-04
^4He	3.23E-02	5.14E-02	6.31E-02	8.85E-02	7.99E-02
^{12}C	5.84E-03	1.28E-02	1.64E-02	2.23E-02	1.71E-02
^{13}C	5.16E-05	2.03E-05	1.01E-05	3.63E-06	6.97E-07
^{14}N	1.31E-03	6.03E-04	3.45E-04	1.52E-04	3.40E-05
^{15}N	-2.03E-06	-9.21E-07	-4.88E-07	-1.65E-07	-2.07E-08
^{16}O	-1.04E-05	1.70E-04	2.98E-04	4.47E-04	4.03E-04
^{17}O	3.32E-05	2.33E-05	1.68E-05	7.09E-06	9.33E-07
^{18}O	-5.65E-06	-2.78E-06	-1.53E-06	-5.08E-07	-3.20E-08
^{19}F	8.17E-07	1.61E-06	2.23E-06	3.97E-06	2.44E-06
^{20}Ne	-2.34E-06	1.33E-06	6.48E-06	2.80E-05	1.17E-05
^{21}Ne	8.15E-08	2.56E-07	3.94E-07	1.00E-06	5.54E-07
^{22}Ne	7.06E-04	1.21E-03	1.54E-03	2.69E-03	1.41E-03
^{23}Na	1.95E-05	1.77E-05	1.77E-05	3.25E-05	1.38E-05
^{24}Mg	9.94E-06	2.40E-05	3.32E-05	7.33E-05	2.64E-05
^{25}Mg	7.10E-07	6.21E-06	1.28E-05	4.36E-05	2.55E-05
^{26}Mg	3.16E-06	7.11E-06	8.17E-06	3.14E-05	3.21E-05
^{26}Al	3.06E-07	1.24E-07	6.62E-08	5.40E-08	5.33E-08
^{36}Cl	1.38E-09	1.42E-09	9.66E-10	4.34E-10	3.95E-11

Table 14—Continued

Isotope	$Z = 1.38 \times 10^{-2}$	$Z = 6.0 \times 10^{-3}$	$Z = 3.0 \times 10^{-3}$	$Z = 1.0 \times 10^{-3}$	$Z = 1.0 \times 10^{-4}$
⁴¹ Ca	3.90E-09	3.38E-09	2.05E-09	8.58E-10	7.11E-11
⁶⁰ Fe	5.76E-08	5.04E-08	6.35E-08	1.26E-07	2.04E-08
⁸⁹ Y	1.18E-07	1.01E-07	4.79E-08	1.55E-08	1.08E-09
¹⁰⁷ Pd	1.56E-09	1.70E-09	7.88E-10	1.99E-10	1.03E-11
¹³⁹ La	1.56E-08	5.44E-08	3.96E-08	1.08E-08	4.80E-10
²⁰⁵ Pb	1.48E-10	1.05E-09	1.54E-09	3.94E-10	1.30E-11
²⁰⁸ Pb	1.88E-08	1.51E-07	5.50E-07	8.48E-07	1.03E-07

Note. — Table 14 is published in its entirety in the electronic edition of the *Astrophysical Journal*. A portion regarding selected isotopes is shown here for guidance regarding its form and content.

Table 15. Final isotopic surface abundances (by mass fraction) of selected short-lived radioactive isotopes (with the corresponding stable isotopes) at different Z .

Isotope	$Z = 1.38 \times 10^{-2}$	$Z = 6.0 \times 10^{-3}$	$Z = 3.0 \times 10^{-3}$	$Z = 1.0 \times 10^{-3}$	$Z = 1.0 \times 10^{-4}$
^{26}Al	3.07E-07	1.41E-07	7.80E-08	7.37E-08	5.33E-08
^{27}Al	6.14E-05	2.77E-05	1.43E-05	6.43E-06	1.98E-06
^{35}Cl	3.72E-06	1.61E-06	7.97E-07	2.59E-07	2.78E-08
^{36}Cl	1.70E-09	1.51E-09	9.29E-10	5.35E-10	3.50E-11
^{40}Ca	6.26E-05	2.70E-05	1.34E-05	4.35E-06	4.78E-07
^{41}Ca	5.13E-09	3.52E-09	1.90E-09	1.11E-09	7.11E-11
^{56}Fe	1.20E-03	5.17E-04	2.56E-04	8.26E-05	8.35E-06
^{60}Fe	4.78E-08	3.93E-08	5.70E-08	1.38E-07	2.04E-08
^{204}Pb	2.42E-09	1.24E-08	1.58E-08	4.80E-09	1.50E-10
^{205}Pb	1.58E-10	1.04E-09	1.55E-09	4.61E-10	1.31E-11

Table 16. Final composition of the three models at $Z=10^{-4}$ (Reference, Reimers and low mixing length).

[El/Fe]	Reference	Reimers	$\alpha=1.8$
[C/Fe]	3.00	3.20	2.81
[N/Fe]	0.86	1.15	0.68
[O/Fe]	1.01	1.17	0.88
[F/Fe]	2.90	3.27	2.66
[Ne/Fe]	2.27	2.68	1.90
[Na/Fe]	1.77	2.26	1.36
[Mg/Fe]	1.30	1.82	0.84
[Al/Fe]	0.64	0.97	0.47
[ls/Fe]	1.10	1.30	0.85
[hs/Fe]	1.56	1.85	1.33
[Pb/Fe]	2.88	3.00	2.78
[hs/ls]	0.46	0.55	0.48
C/O	53	52	46
C/N	406	325	388
$^{12}\text{C}/^{13}\text{C}$	1.72×10^4	1.35×10^4	1.72×10^4

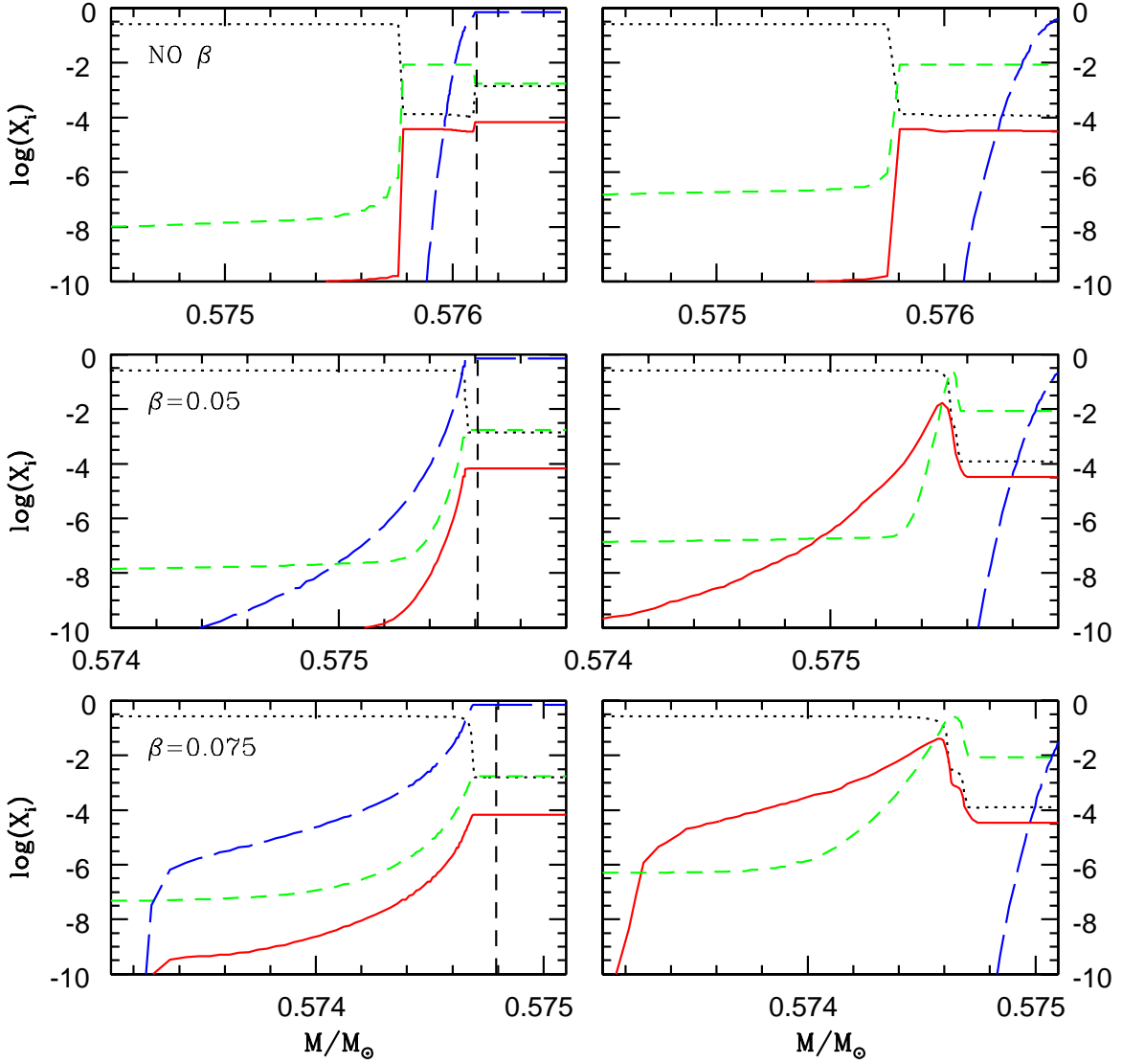


Fig. 1.— Each panel shows the composition of the core-envelope transition zone of the solar metallicity model ($M=2 M_{\odot}$) at the moment of the 3rd TDU, as obtained by adopting low values of the β parameter. We report the mass fractions of ^{12}C (dotted line), ^{13}C (solid line), ^{14}N (short-dashed line) and H (long-dashed line) in the transition zone. Left panels refer to the epoch of the maximum penetration of the convective envelope into the He intershell during the TDU, whilst right panels show the same region after the formation of the ^{13}C pocket. Note that in the $\beta = 0$ case, the convective envelope does not penetrate the H-exhausted core, so that the showed H profile is due to the previous shell-H burning, rather than to the operation of the exponential decline of the convective velocity described by Eq. 1

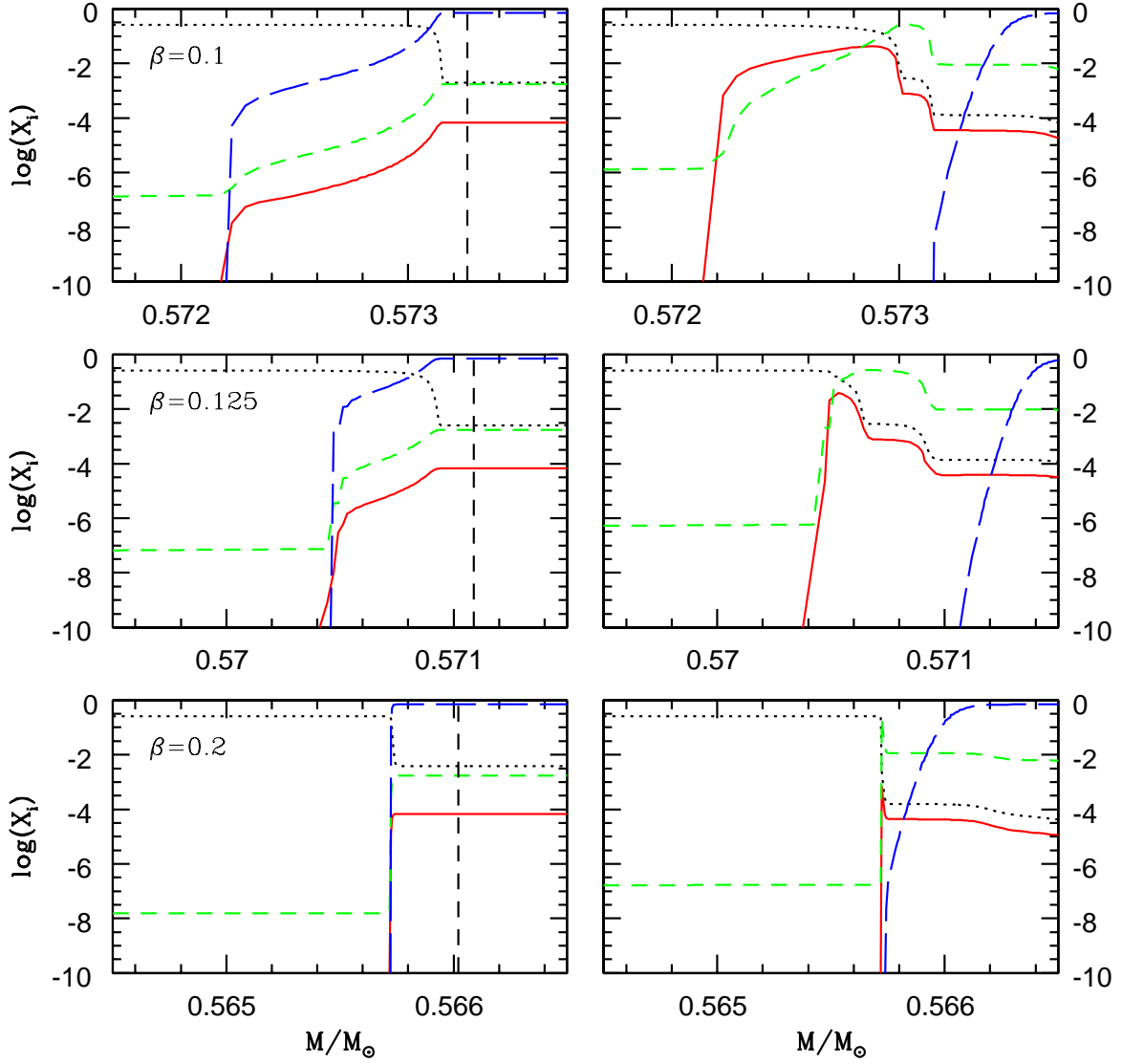


Fig. 2.— Same as in Fig. 1, but for larger values of the β parameter.

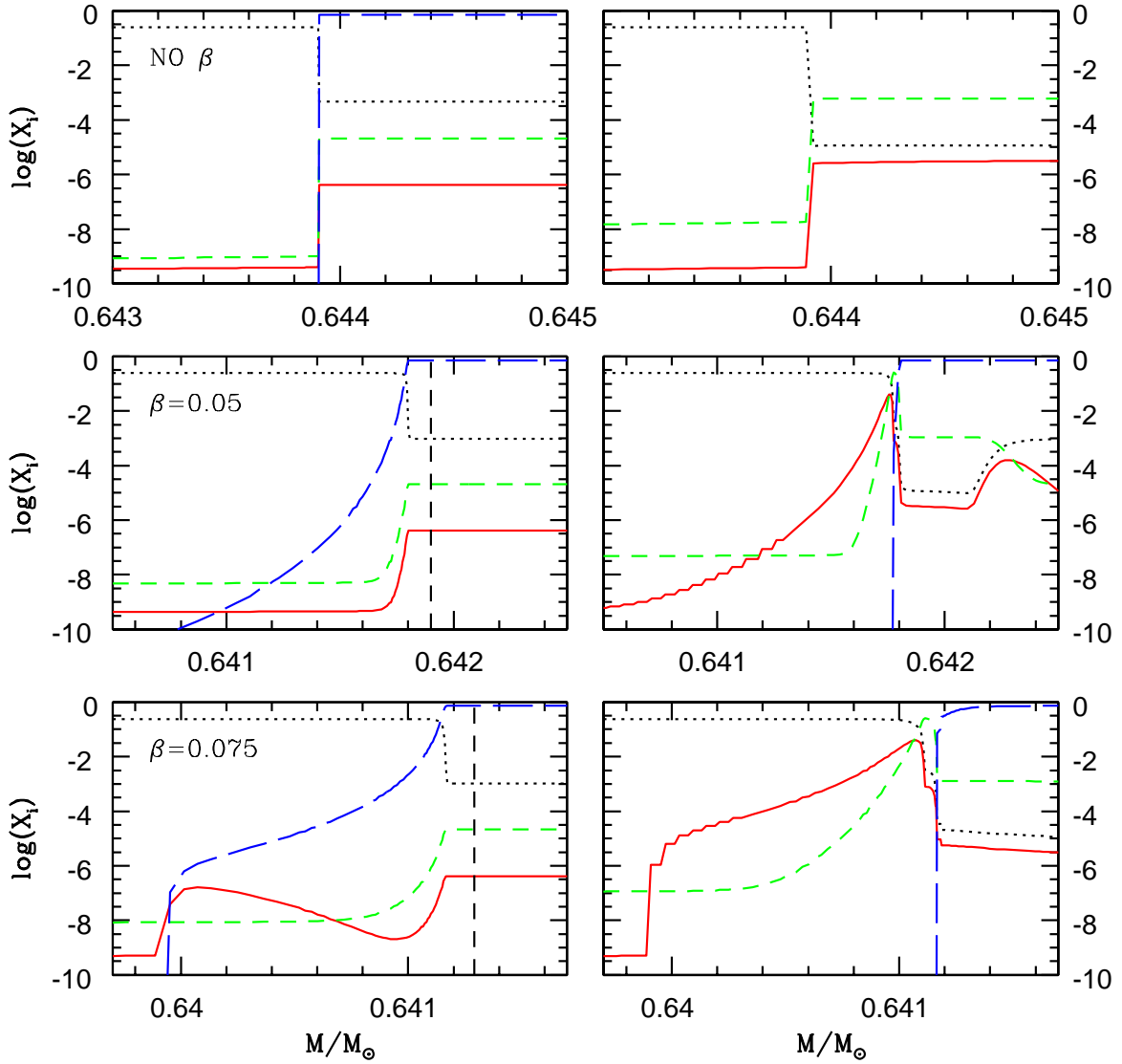


Fig. 3.— Same as in Fig. 1, but relative to the 2nd TDU of the model with $Z=0.0001$ and $M=2 M_\odot$.

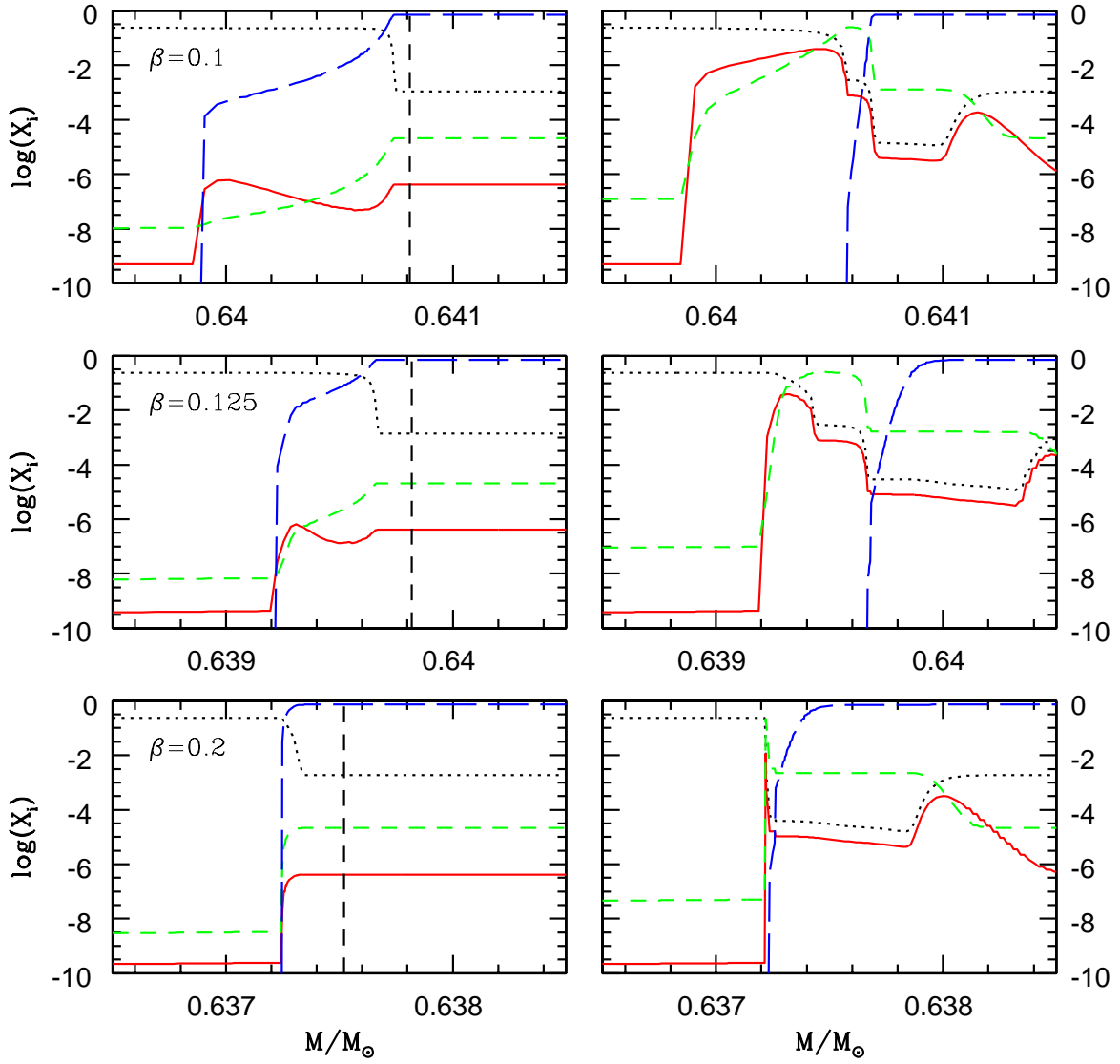


Fig. 4.— Same as in Fig. 3, but for larger values of the β parameter.

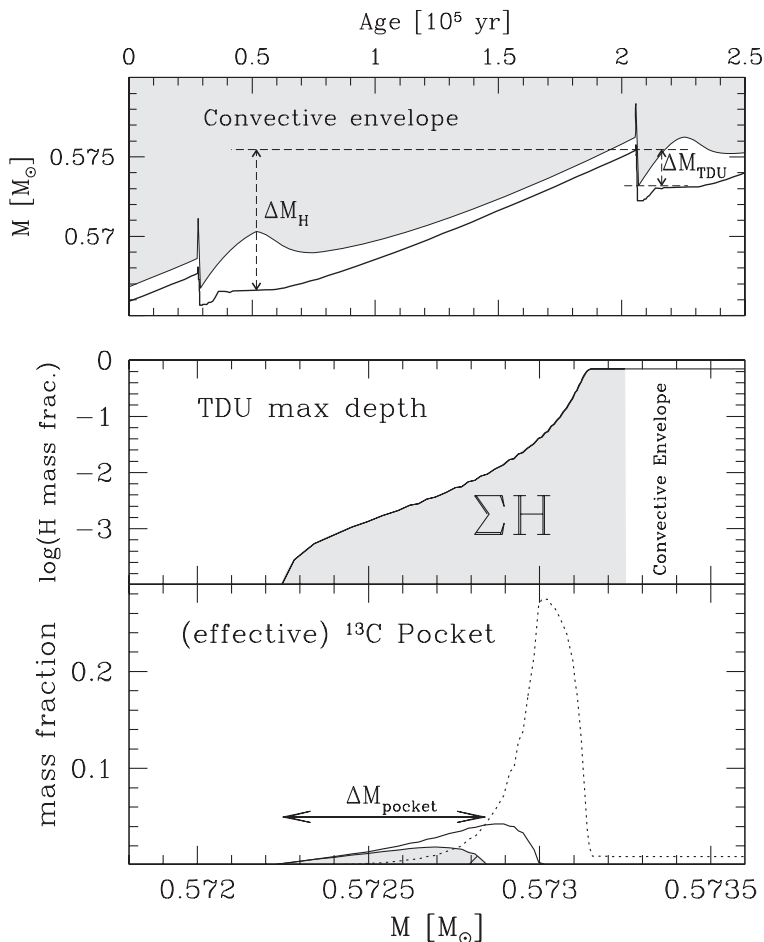


Fig. 5.— *Upper panel:* the evolutions of the transition region between the convective envelope and the H-exhausted core in between the 4th and the 5th thermal pulse of the 2 M_{\odot} model with solar metallicity and $\beta = 0.1$. The more external line represents the inner border of the convective envelope while the lower line shows the location of the layer where the nuclear energy production is maximum in the H-burning shell. The 2nd and the 3rd TDU episode are easily recognized. The quantity ΔM_H and ΔM_{TDU} are also graphically illustrated. *Central panel:* H profile in the top layer of the H-exhausted core at the epoch of the maximum penetration of the convective envelope during the 3rd TDU episode. The shaded area represents the quantity ΣH , namely the total mass of H left below the formal border of the convective envelope. *Bottom panel:* the same region, but after the development of the ^{13}C pocket. The solid and the dotted lines represent the mass fractions of ^{13}C and ^{14}N , respectively, while the shaded area is $\Sigma^{13}\text{C}_{\text{eff}}$, namely the mass of the *effective* ^{13}C in the pocket (see footnote 3 for the definition of *effective* ^{13}C). The arrow shows the parameter ΔM_{pocket} , corresponding to the extension (in mass) of the region where the *effective* ^{13}C is larger than 10^{-3}

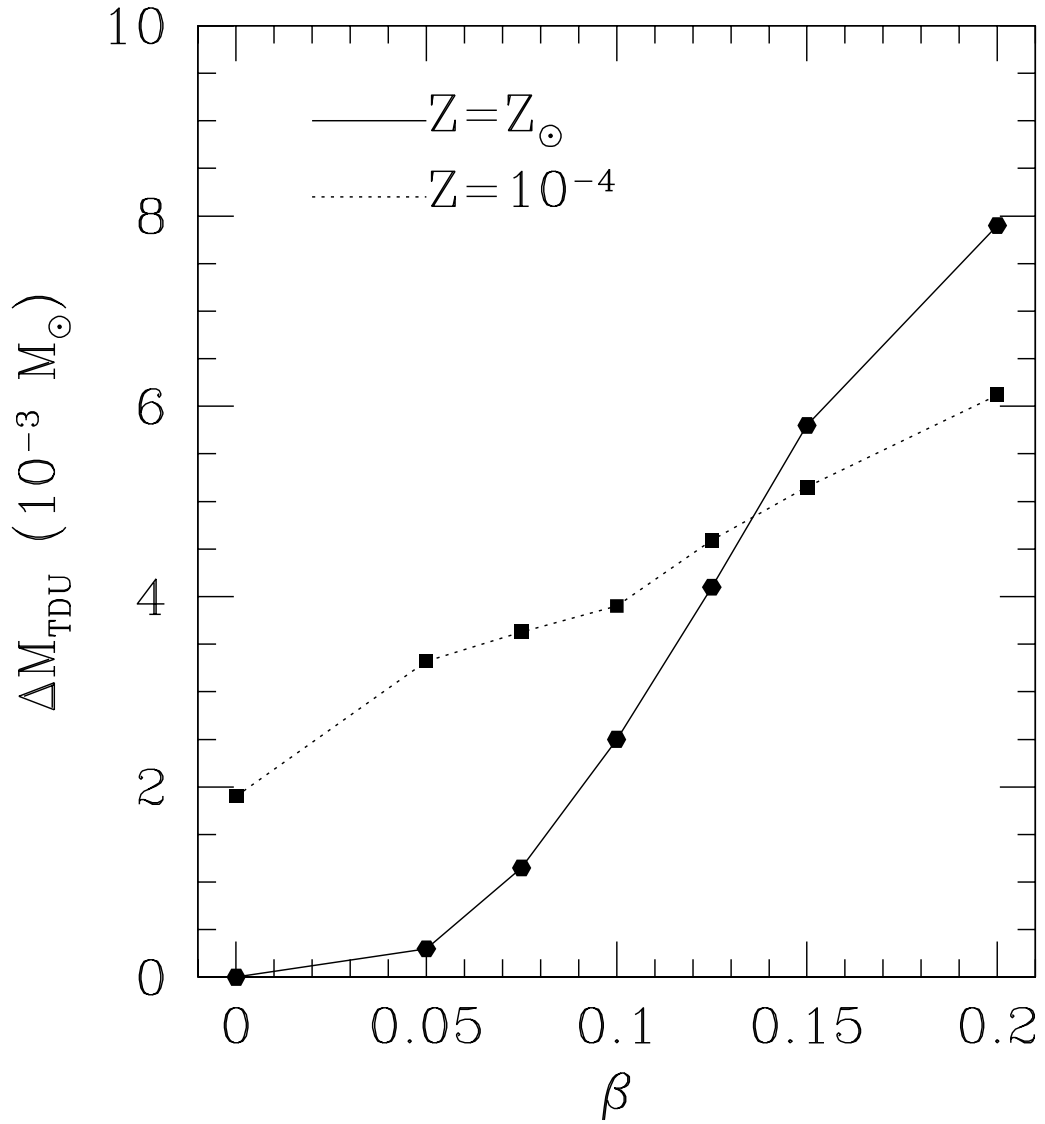


Fig. 6.— The mass portion of the He intershell that is dredged up versus the β parameter after the 3rd pulse followed by TDU of the solar metallicity model and after the 2nd pulse followed by TDU of the $Z=0.0001$ model. See text for details.

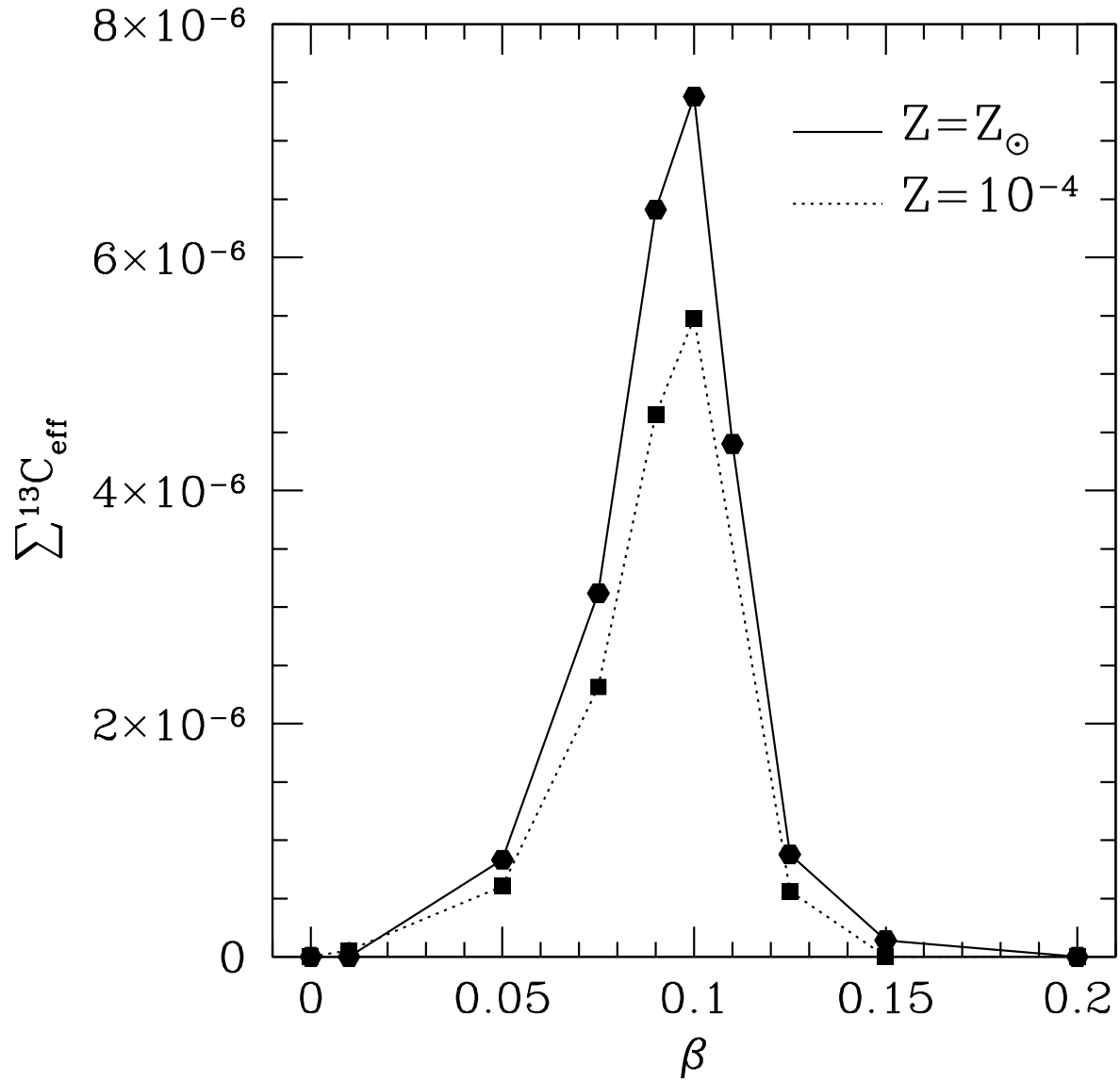


Fig. 7.— The variation with β of the effective ^{13}C mass in the pocket after the 3rd pulse followed by TDU of the solar metallicity model and after the 2nd pulse followed by TDU of the $Z=0.0001$ model. See text for details.

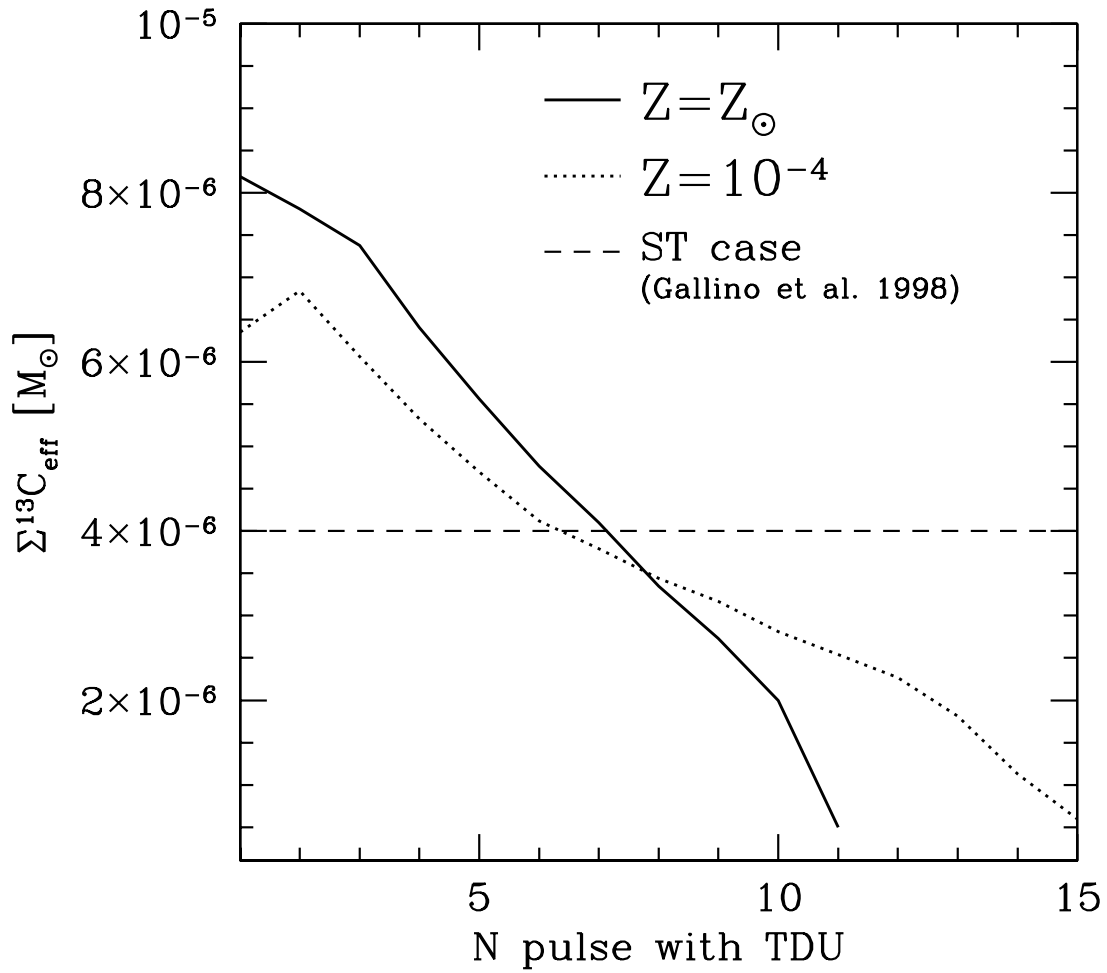


Fig. 8.— Evolution of the effective ^{13}C mass in the pockets vs. the number of pulses followed by TDU, for models at $Z=Z_{\odot}$ and $Z = 0.0001$. Note the decrease of ^{13}C in the pockets along the AGB evolution. For comparison, the ST case of Gallino et al. (1998) is reported.

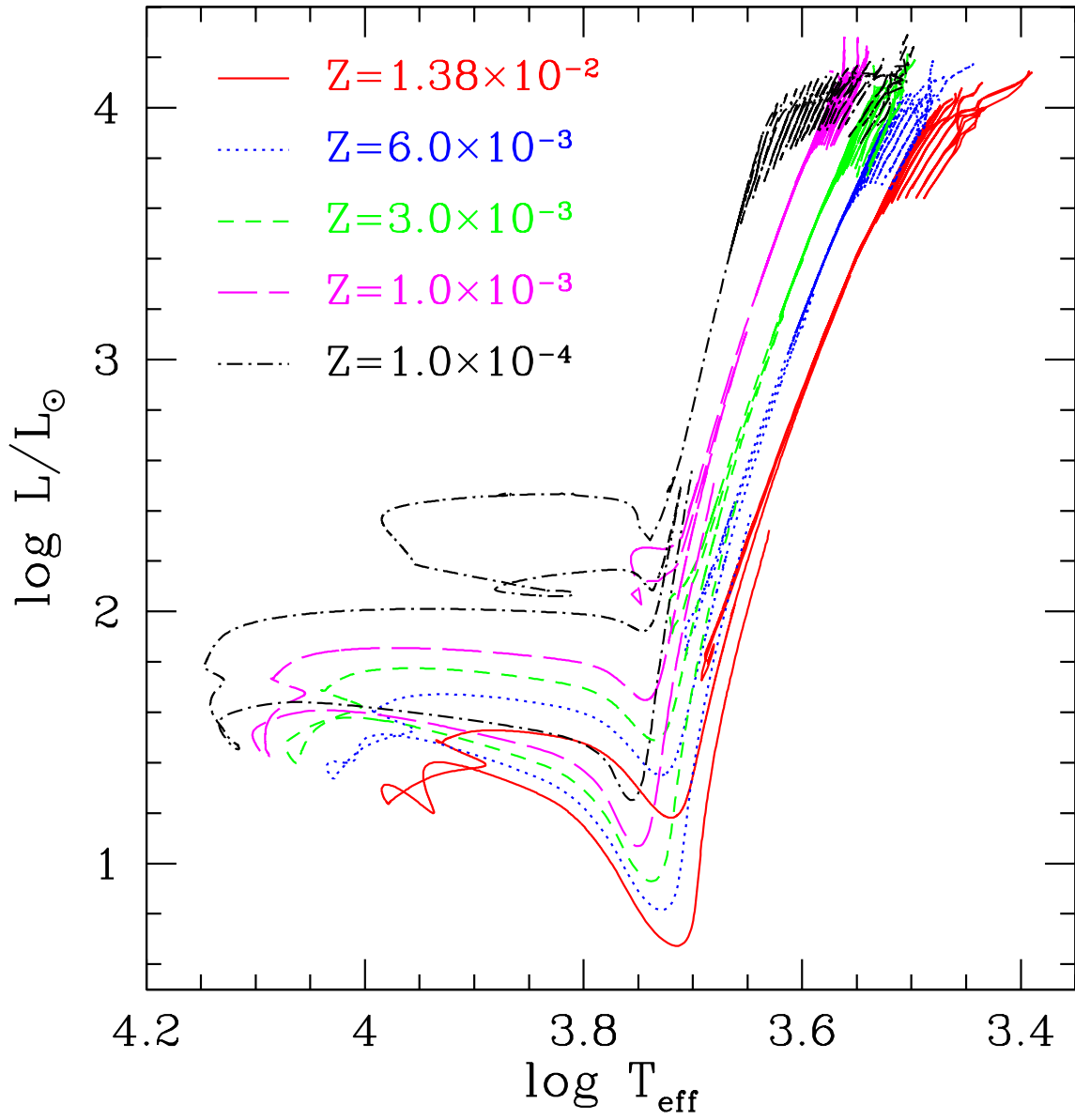


Fig. 9.— Evolutionary tracks in the HR diagram of the five $2 M_{\odot}$ models.

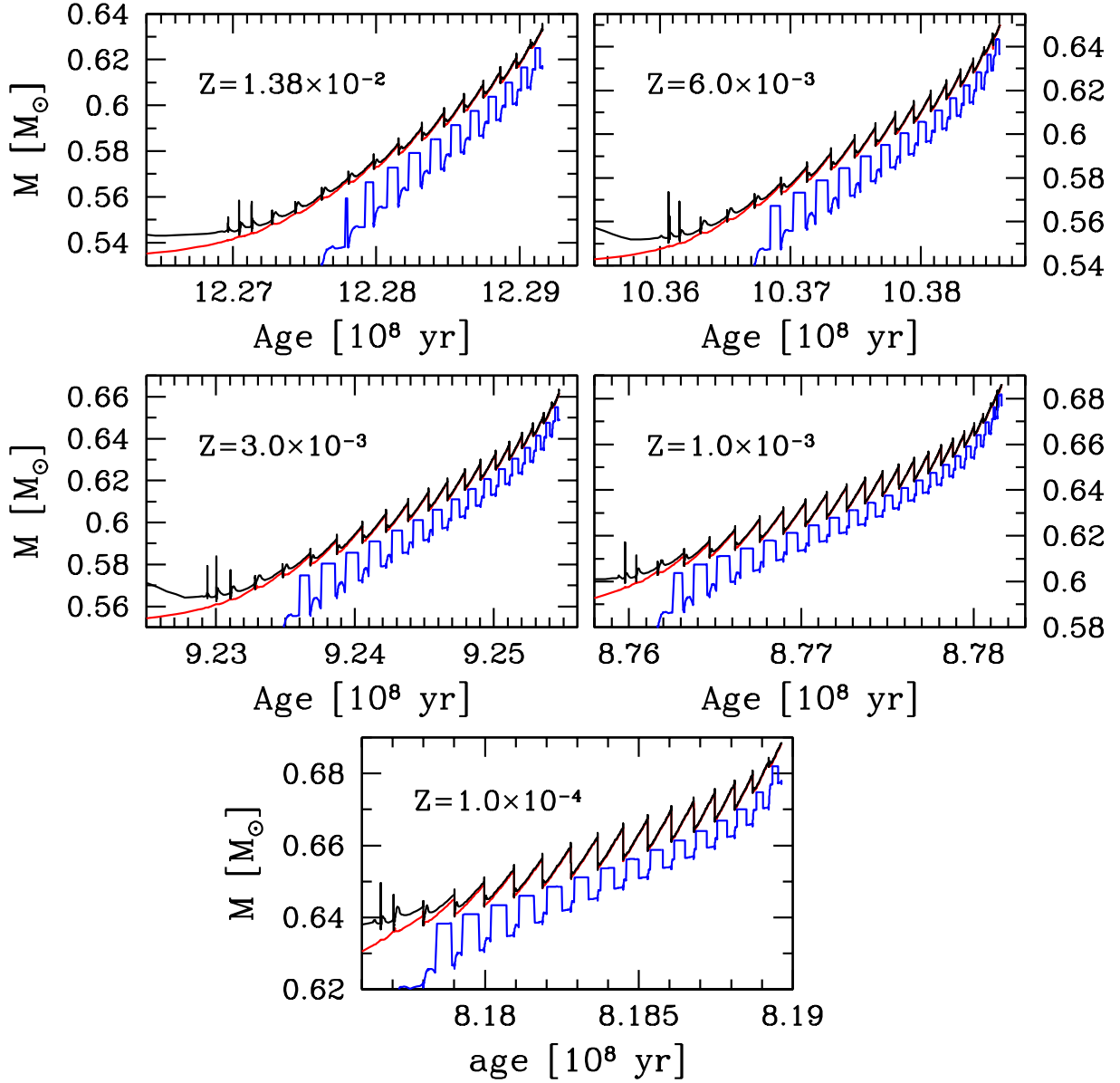


Fig. 10.— Evolution of the positions, in mass coordinates, of the inner border of the convective envelope, of the location of the maximum energy production within the H-burning shell and of the location of the maximum energy production within the He-burning shell, top to bottom line, respectively. Blue spikes correspond to the activation of the $^{13}\text{C}(\alpha, n)^{16}\text{O}$ reaction (see text for details). Each panel represents one of the five $2 M_{\odot}$ models, as labelled in the plots.

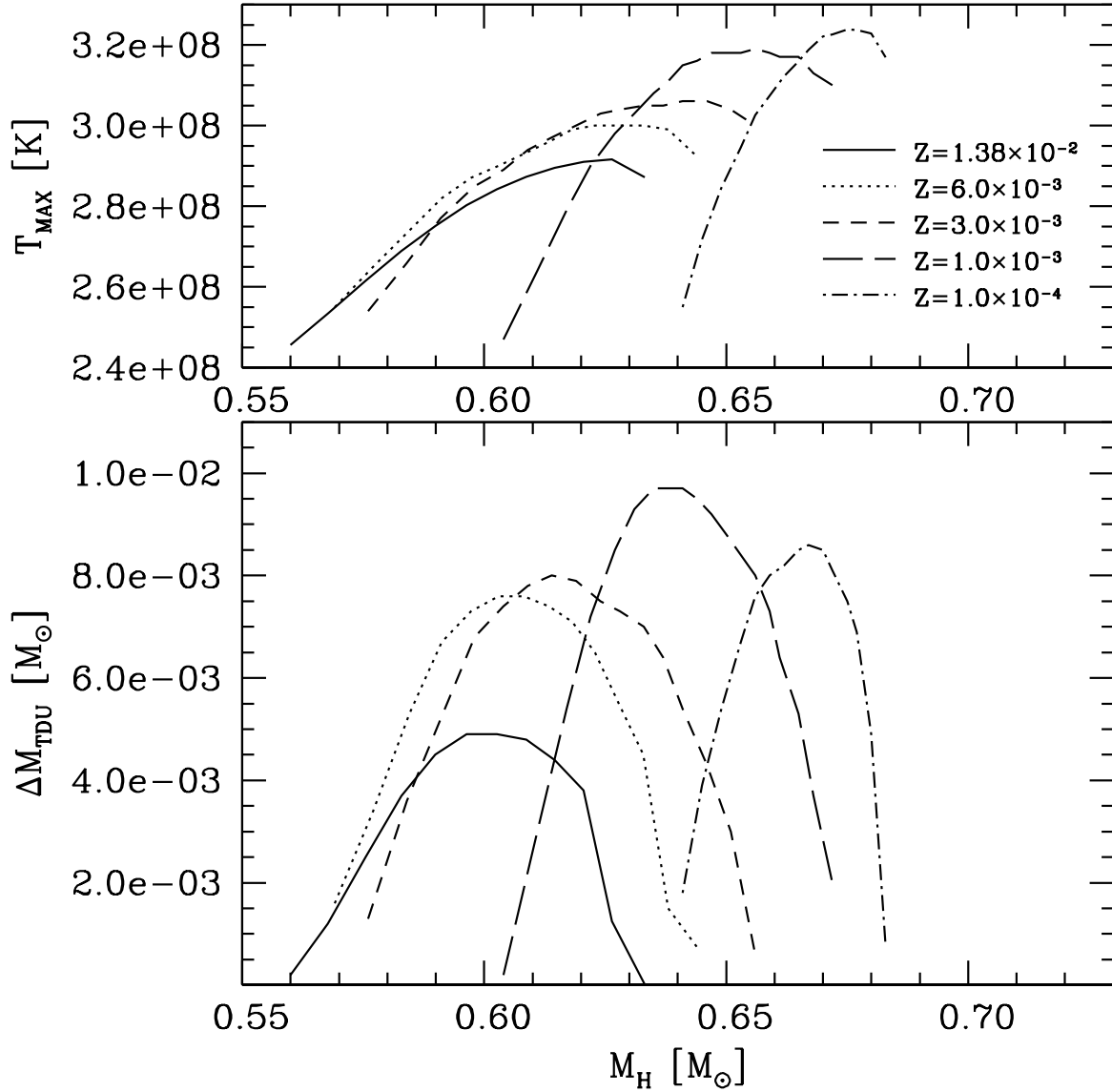


Fig. 11.— Upper panel: maximum temperature attained at the bottom of the convective zone generated by a thermal pulse versus the mass of the H-exhausted core (M_H). Lower panel: the mass of H-depleted material that is dredged up after each thermal pulse versus M_H . The five lines of each panels refer to the five different models, as labelled in the plots.

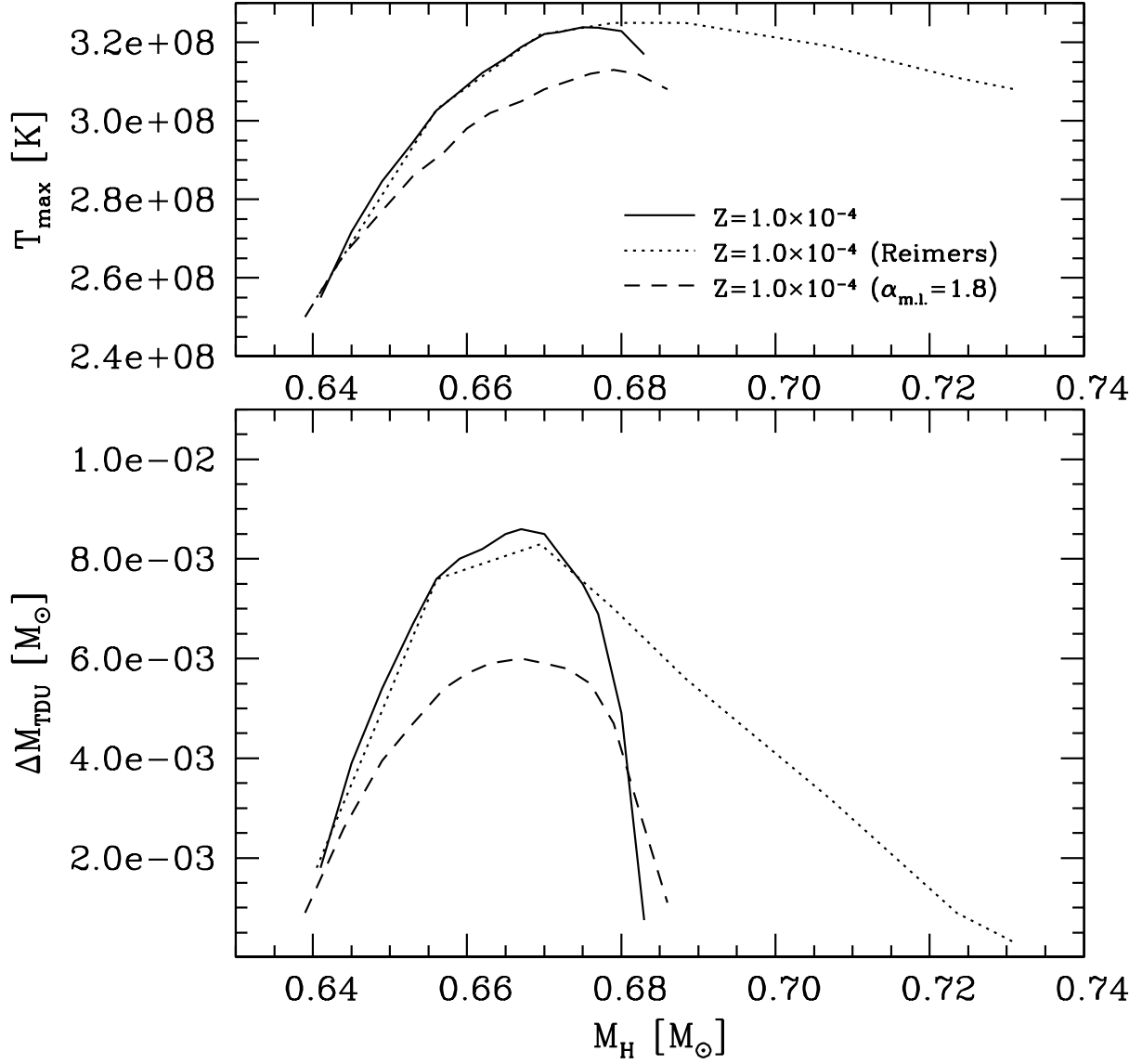


Fig. 12.— The same as in Fig. 11 for the reference $Z=0.0001$ model (solid lines) and for the two additional models with varied mass loss (dotted lines) and mixing length (dashed lines).

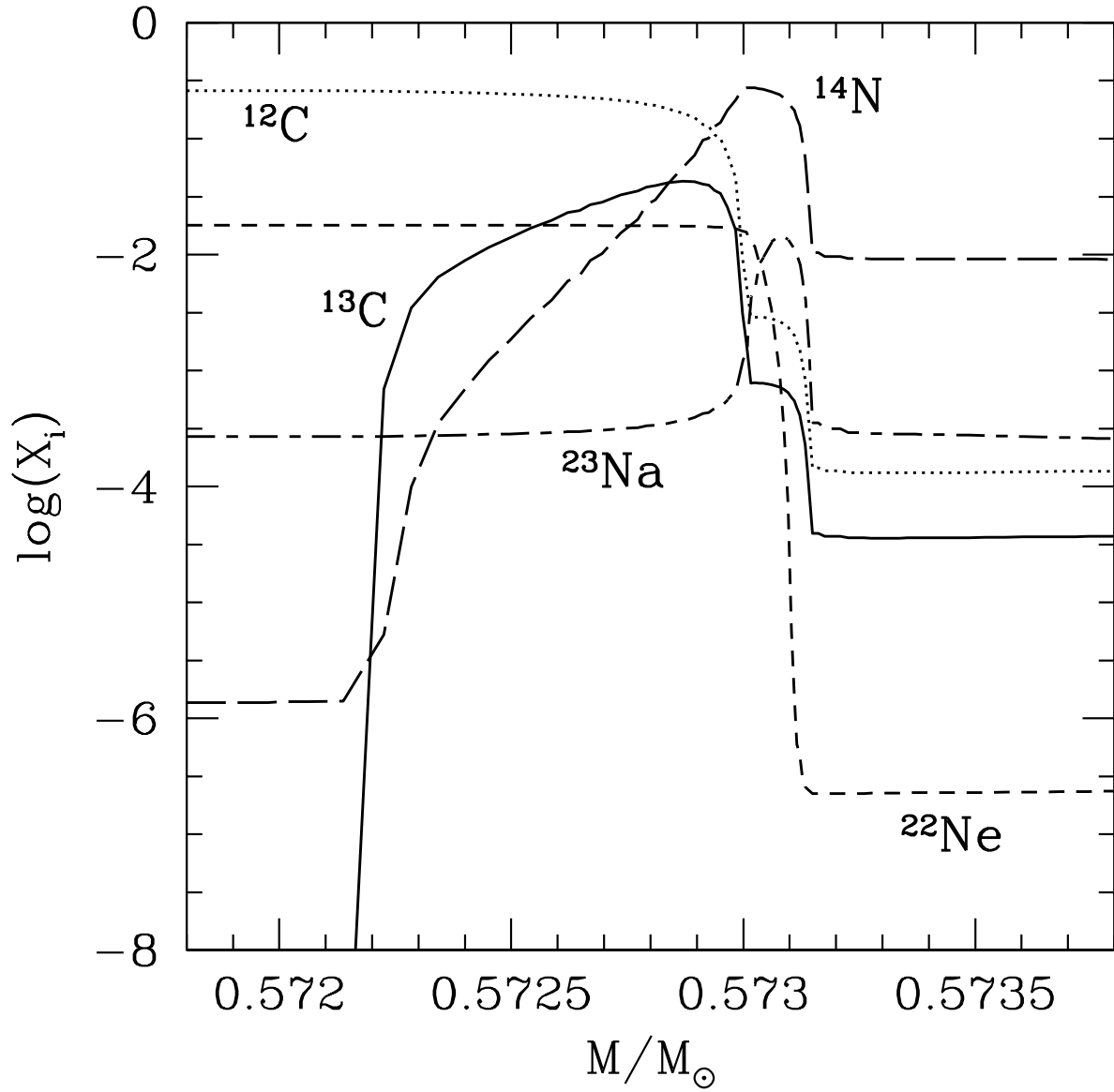


Fig. 13.— Mass fractions of selected isotopes in the third ^{13}C pocket of the solar metallicity model. The ^{14}N pocket and the ^{23}Na pocket clearly appear in the figure. See text for details.

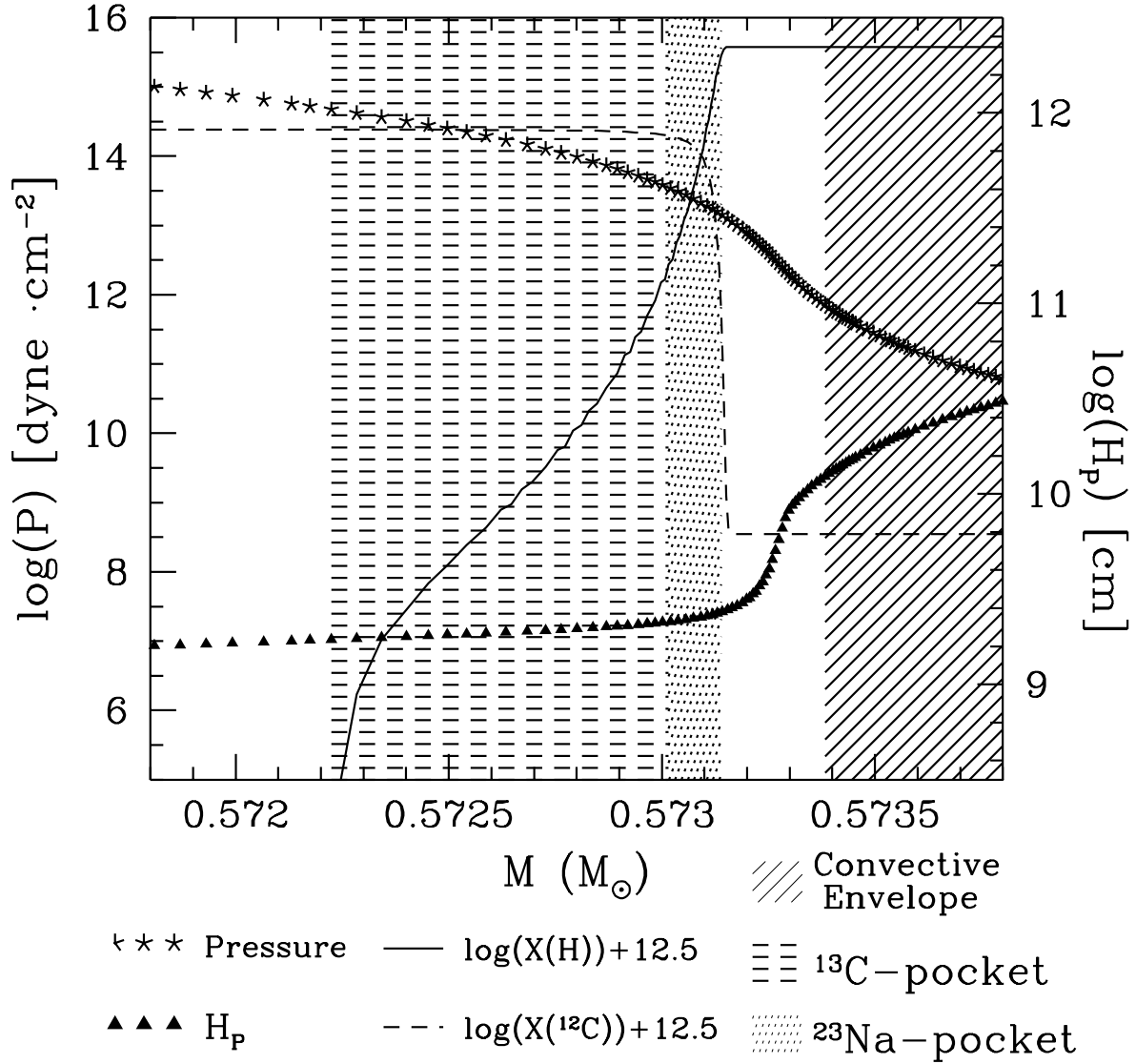


Fig. 14.— Variations of the pressure and of the pressure scale height (H_p) in the core-envelope transition region at the time of the maximum penetration of the 3rd TDU of the solar metallicity model. Solid and dashed lines represents the H and the ^{12}C profiles, respectively (abundances have been shifted upward in order to match the pressure scale axis). Slanting dashed area shows the envelope region, whilst the horizontal and the vertical dashed areas mark the ^{13}C and the ^{23}Na pockets (the ^{14}N pocket is not reported in the plot).

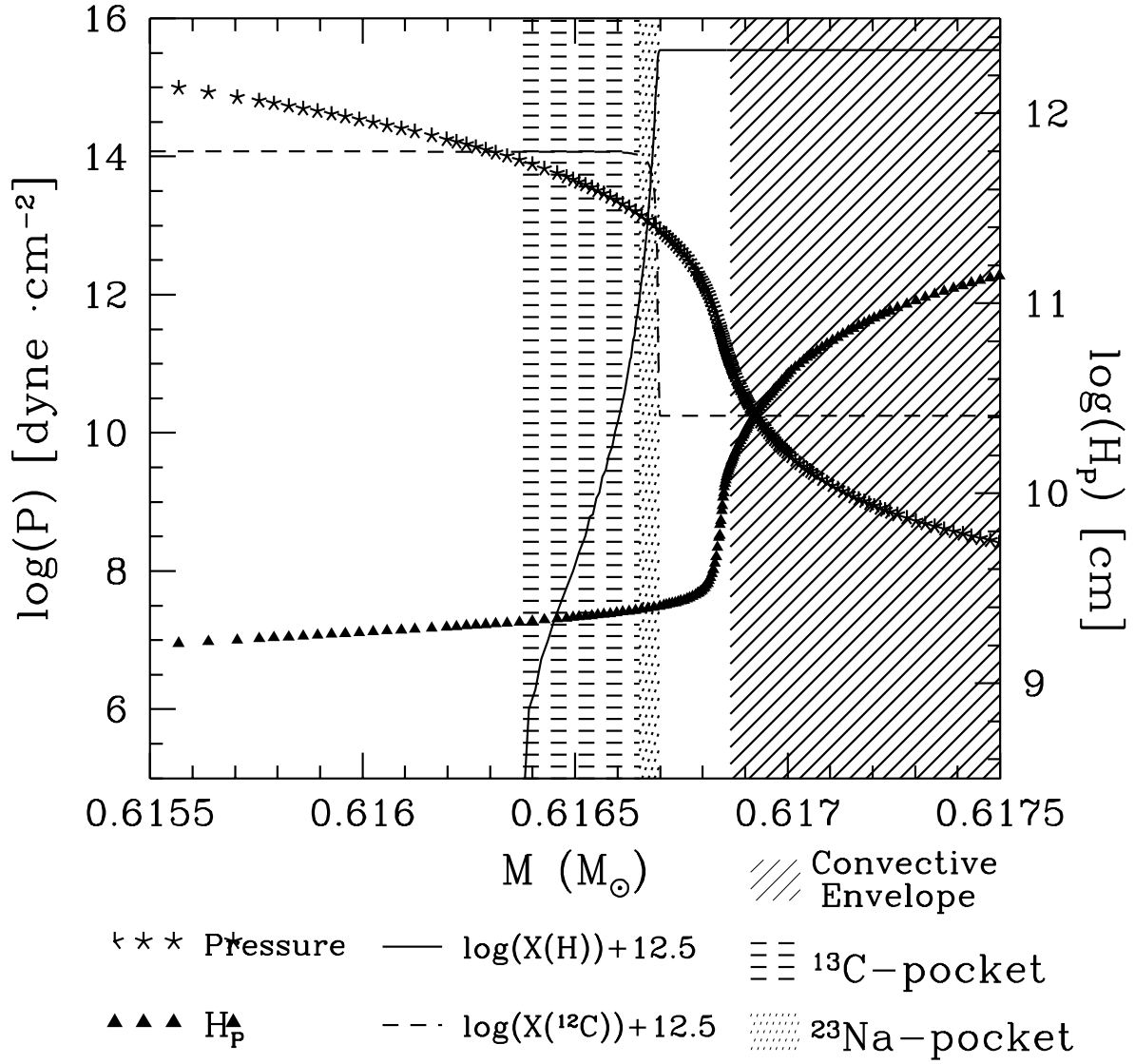


Fig. 15.— As in Fig. 14, but relative to the 11th TDU of the solar metallicity model.

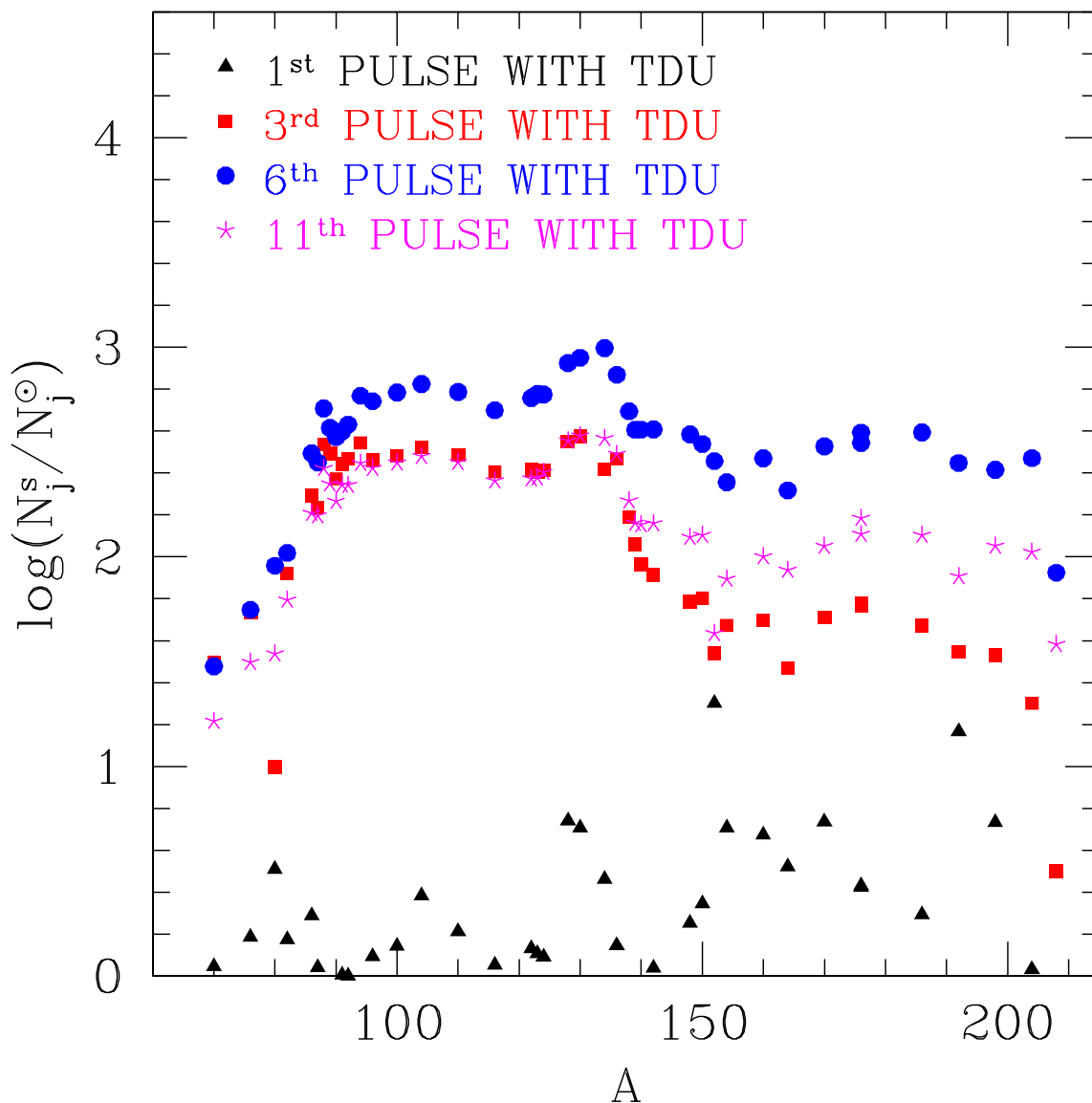


Fig. 16.— Production factors of nuclei whose synthesis is mainly ascribed to the s process (namely, nuclei whose s process contribution is larger than 80%) within the He intershell at the quenching of the convective shells generated by the TPs before the 1st, 3rd, 6th and 11th TDU episodes of the solar metallicity model. The abundances in the He intershell are the result of the mixing of three zones: the deeper layer saw the cumulative mixing of the overlapped convective zones generated by the previous TPs, the central layer, which corresponds to the last ^{13}C pocket and is heavily enriched in s-elements, and the upper layer, which corresponds to the portion of the He intershell containing the ashes produced by the H-burning during the last interpulse period, with a low s-enhancement. The decreases of the production factors in the late AGB is due to the shrinkage of the ^{13}C pockets

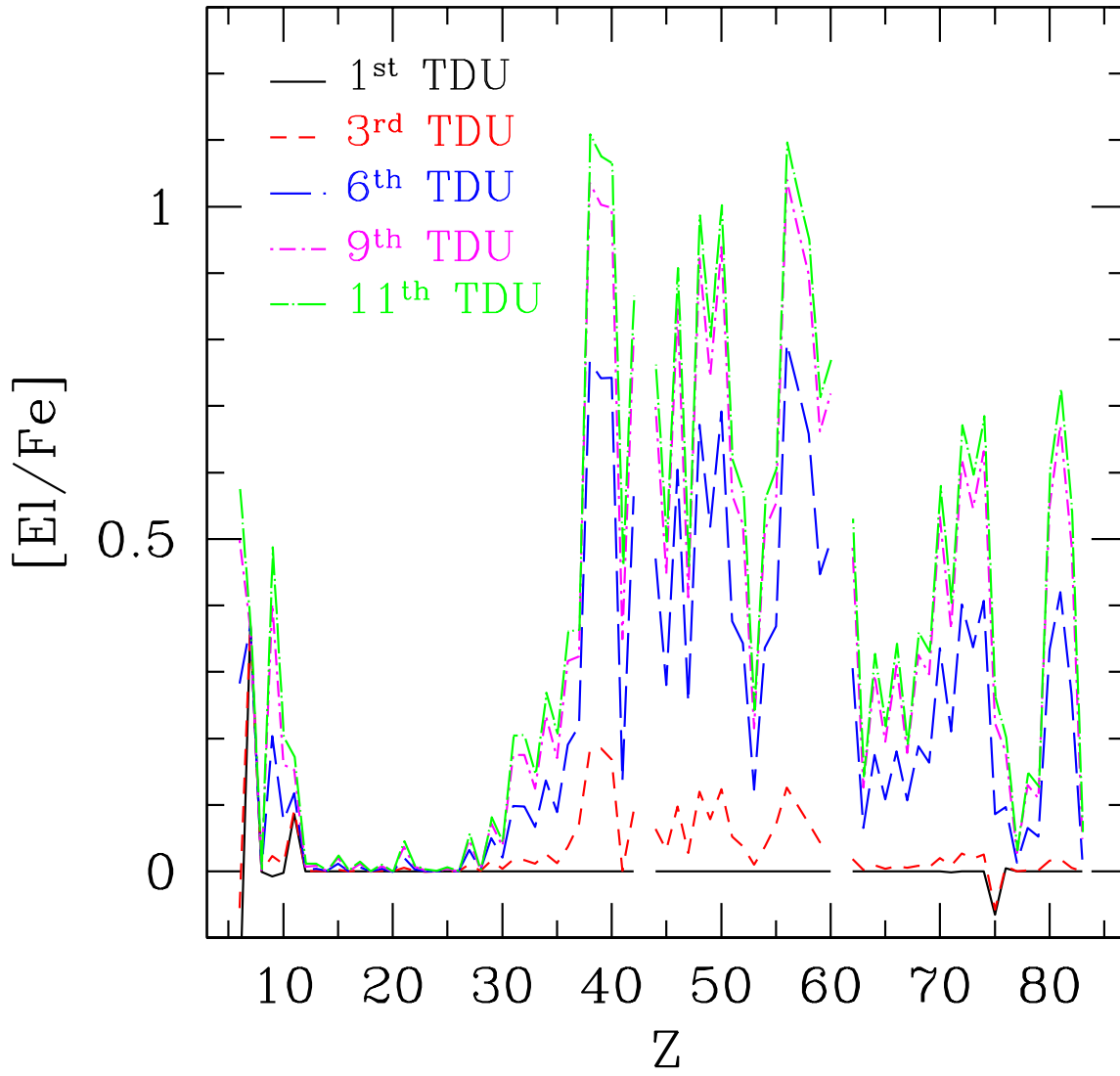


Fig. 17.— Elemental surface composition of the solar metallicity model as it results after selected third dredge up episodes (see labels inside the plot).

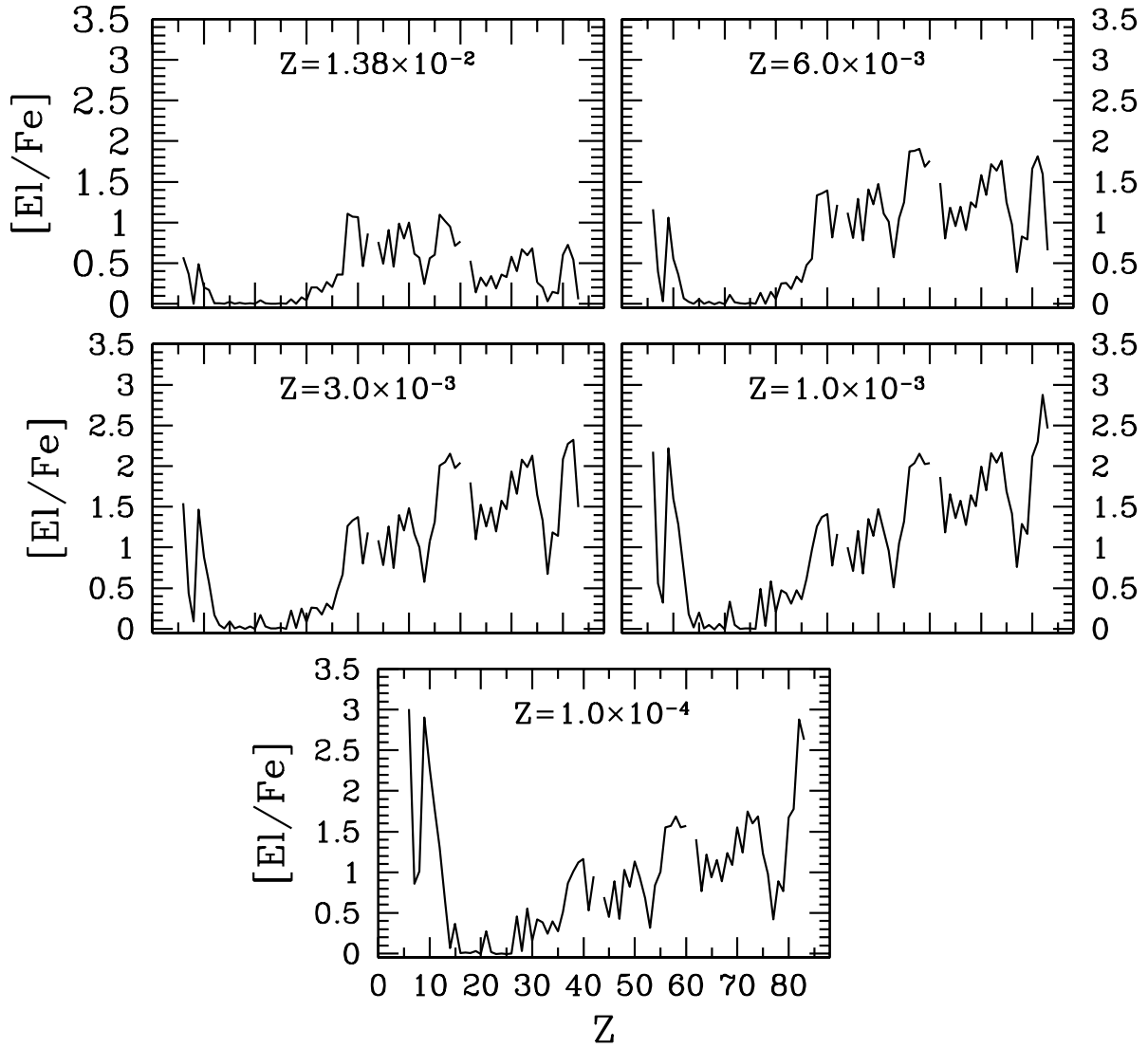


Fig. 18.— Final elemental surface composition of the five evolutionary sequences with different Z , as labelled in the plots.

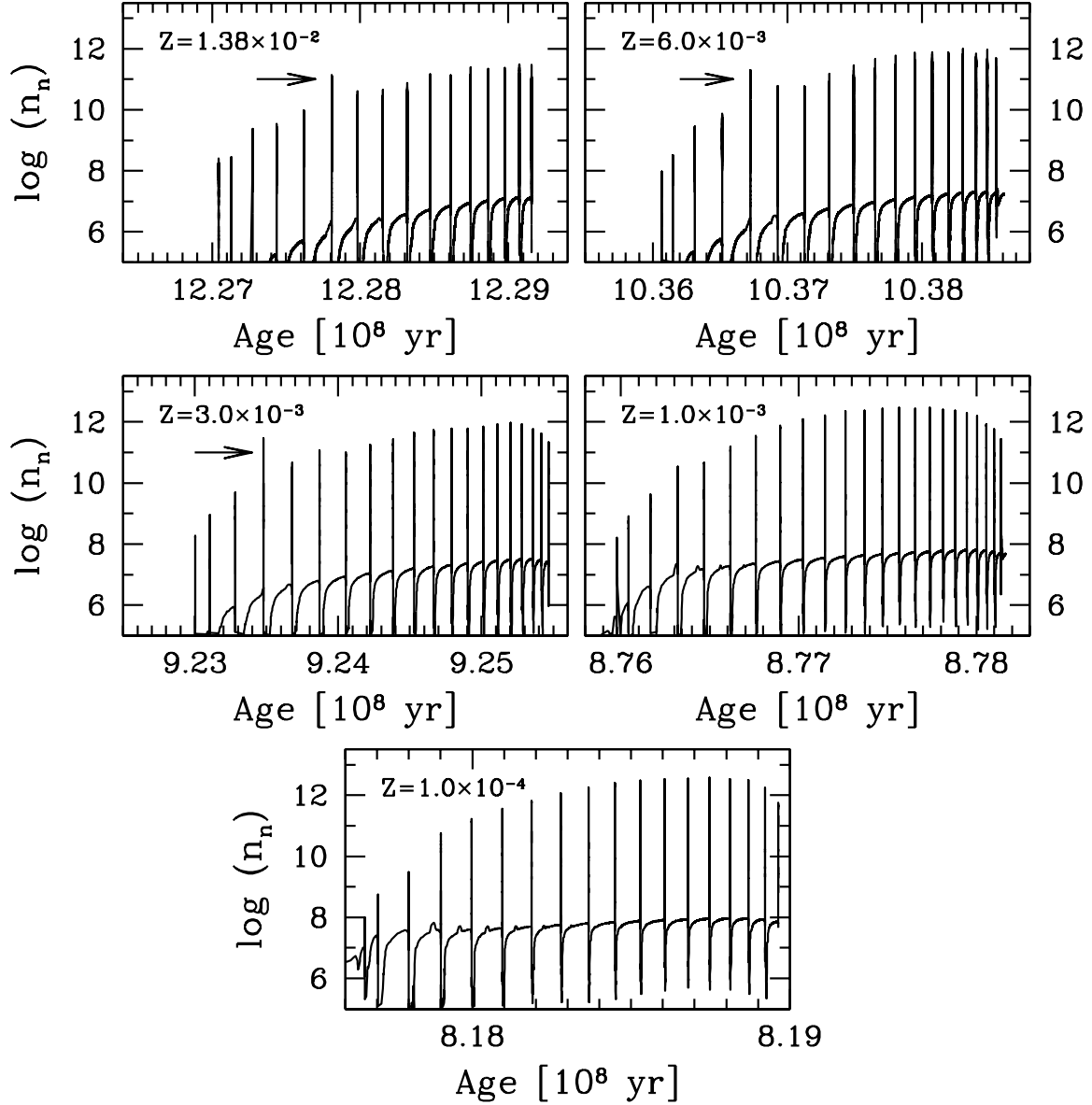


Fig. 19.— Maximum neutron densities attained in models with $M = 2M_{\odot}$ and different metallicities. In the metal-rich models, arrows mark the ingestion of the first ^{13}C pockets into the convective shells generated by the following TPs. See text for details.

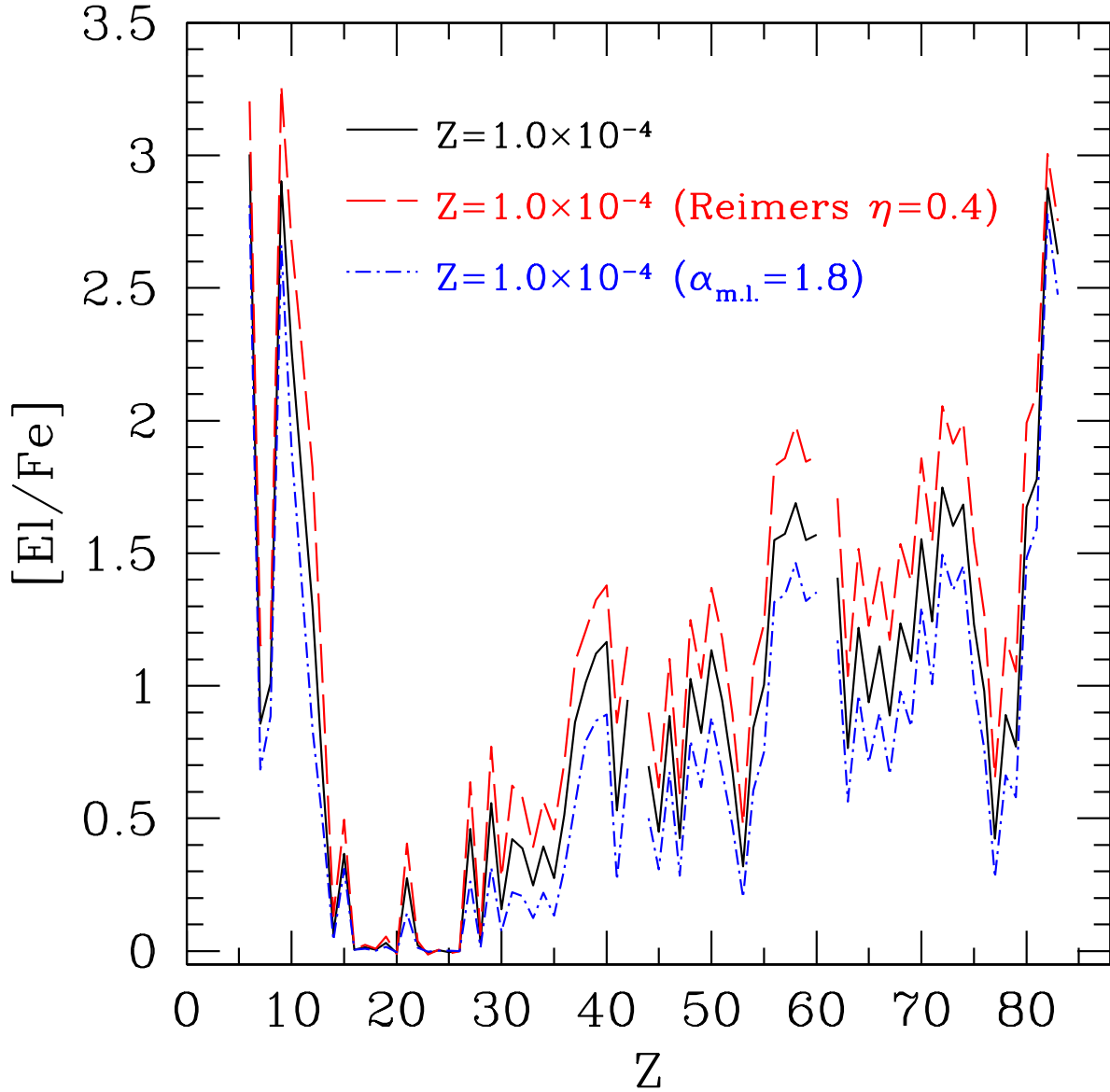


Fig. 20.— Final elemental surface composition of the $Z=0.0001$ reference model is compared with those of the two additional models obtained by adopting a different mass loss rate (Reimers $\eta = 0.4$) or by decreasing the mixing-length parameter ($\alpha_{m.l.} = 1.8$). See text for details.

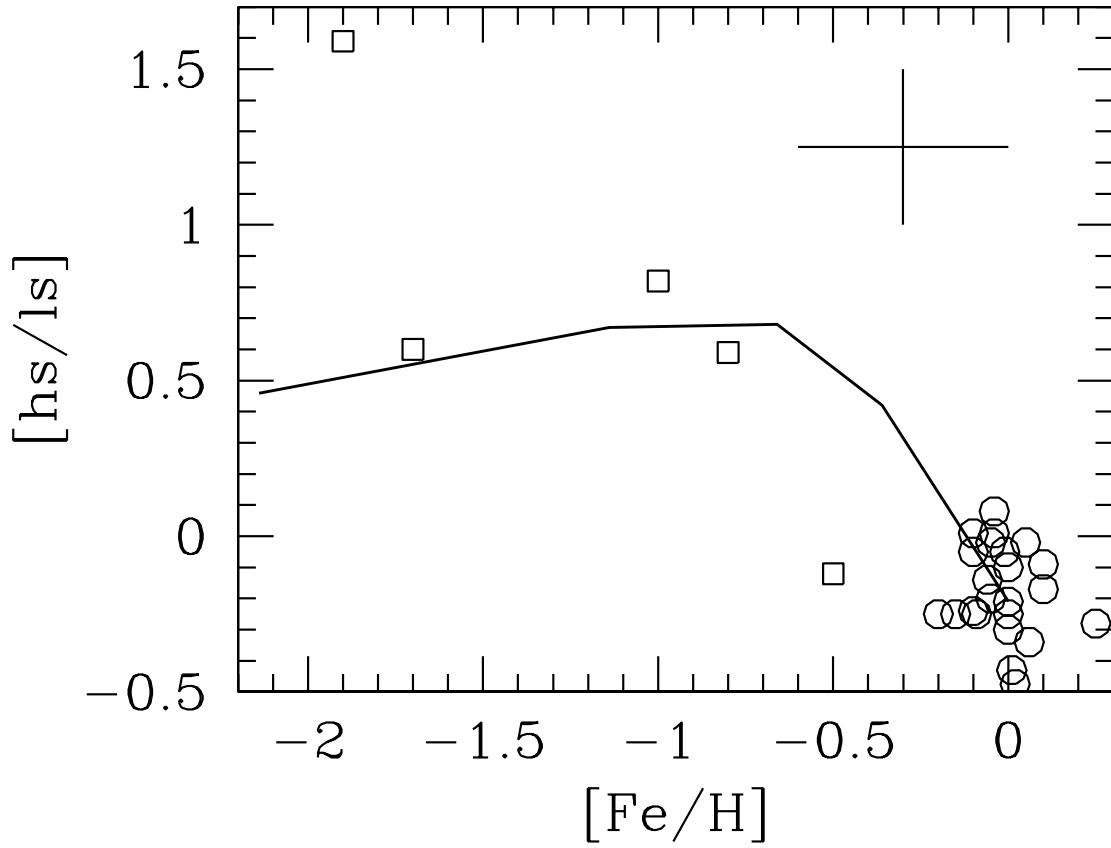


Fig. 21.— The theoretical $[\text{hs}/\text{ls}]$ index (solid curve) compared with the same ratios as observed in intrinsic Galactic (circles, Abia et al. 2002) and extragalactic (squares, de Laverny et al. 2006; Abia et al. 2008) N type C stars. Typical error bars are also reported.

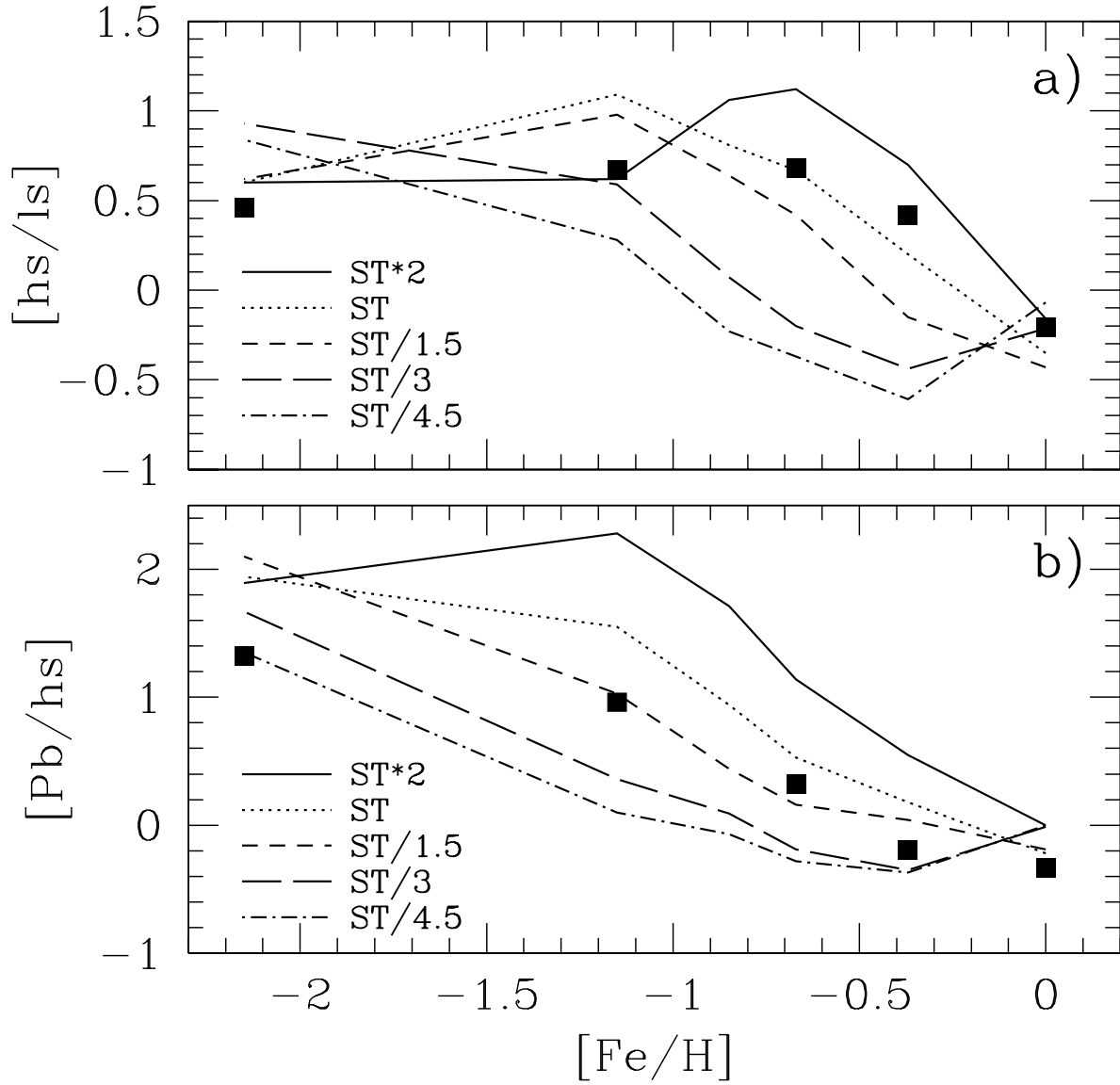


Fig. 22.— Spectroscopic indexes predicted by our new models (filled squares) compared with post-process calculations (Gallino et al. 2008; Bisterzo et al. 2008). In panel a) we report the $[hs/ls]$ index, whilst in panel b) we plot the $[Pb/hs]$ index. See text for details.

Table 17. Pulse by pulse elemental surface composition of the $Z = 0.0138$ model (online only).

[El/Fe]	TDU 1	TDU 2	TDU 3	TDU 4	TDU 5	TDU 6	TDU 7	TDU 8	TDU 9	TDU 10	TDU 11
C	-2.00E-01	-1.58E-01	-5.55E-02	6.72E-02	1.84E-01	2.83E-01	3.65E-01	4.36E-01	4.98E-01	5.54E-01	5.75E-01
N	3.72E-01	3.72E-01	3.72E-01	3.71E-01	3.71E-01	3.69E-01	3.68E-01	3.67E-01	3.66E-01	3.65E-01	3.65E-01
O	-5.16E-04	-5.27E-04	-9.26E-05	6.71E-04	1.50E-03	2.13E-03	2.43E-03	2.44E-03	2.20E-03	1.73E-03	1.36E-03
F	-7.81E-03	-2.14E-03	2.30E-02	7.03E-02	1.34E-01	2.04E-01	2.72E-01	3.38E-01	4.02E-01	4.63E-01	4.88E-01
Ne	-2.55E-03	4.12E-04	1.05E-02	2.77E-02	5.05E-02	7.63E-02	1.03E-01	1.31E-01	1.60E-01	1.90E-01	2.02E-01
Na	8.62E-02	8.78E-02	9.19E-02	9.87E-02	1.08E-01	1.18E-01	1.29E-01	1.40E-01	1.53E-01	1.66E-01	1.72E-01
Mg	-1.92E-07	4.70E-05	2.60E-04	6.82E-04	1.36E-03	2.34E-03	3.59E-03	5.16E-03	7.10E-03	9.44E-03	1.06E-02
Al	1.72E-04	4.57E-04	9.36E-04	1.76E-03	2.92E-03	4.26E-03	5.68E-03	7.10E-03	8.54E-03	9.99E-03	1.06E-02
Si	4.52E-07	2.82E-05	1.34E-04	2.72E-04	4.19E-04	5.65E-04	7.01E-04	8.25E-04	9.51E-04	1.07E-03	1.12E-03
P	1.25E-06	4.24E-04	2.16E-03	4.94E-03	8.24E-03	1.16E-02	1.47E-02	1.76E-02	2.02E-02	2.26E-02	2.35E-02
S	-1.24E-06	6.36E-06	4.25E-05	9.76E-05	1.64E-04	2.32E-04	2.98E-04	3.55E-04	4.13E-04	4.63E-04	4.82E-04
Cl	6.89E-07	2.86E-04	1.30E-03	2.79E-03	4.49E-03	6.28E-03	8.08E-03	9.91E-03	1.17E-02	1.36E-02	1.42E-02
Ar	1.18E-06	-3.61E-05	-1.07E-04	-1.84E-04	-2.49E-04	-2.95E-04	-3.38E-04	-3.88E-04	-4.43E-04	-5.10E-04	-5.42E-04
K	-2.58E-04	-1.87E-05	7.40E-04	1.77E-03	2.89E-03	4.04E-03	5.19E-03	6.36E-03	7.58E-03	8.81E-03	9.53E-03
Ca	1.41E-05	-3.27E-05	-1.32E-04	-2.34E-04	-3.19E-04	-3.75E-04	-4.26E-04	-4.82E-04	-5.42E-04	-6.16E-04	-6.66E-04

Table 17—Continued

[El/Fe]	TDU 1	TDU 2	TDU 3	TDU 4	TDU 5	TDU 6	TDU 7	TDU 8	TDU 9	TDU 10	TDU 11
Sc	1.16E-06	1.80E-03	5.79E-03	1.07E-02	1.59E-02	2.11E-02	2.64E-02	3.17E-02	3.73E-02	4.30E-02	4.53E-02
Ti	9.27E-07	6.62E-05	4.86E-04	1.29E-03	2.36E-03	3.54E-03	4.69E-03	5.77E-03	6.78E-03	7.70E-03	8.03E-03
V	8.69E-07	-1.25E-04	-3.21E-04	-4.23E-04	-3.43E-04	-7.78E-05	3.16E-04	7.88E-04	1.32E-03	1.88E-03	2.11E-03
Cr	7.69E-07	-1.55E-06	8.29E-06	2.82E-05	5.44E-05	8.85E-05	1.20E-04	1.46E-04	1.75E-04	2.03E-04	2.10E-04
Mn	1.96E-06	-9.30E-05	-1.94E-04	-1.44E-04	1.56E-04	7.38E-04	1.56E-03	2.58E-03	3.79E-03	5.13E-03	5.72E-03
Fe	0.00E+00	0.00E+00	0.00E+00	0.00E+00	0.00E+00	0.00E+00	0.00E+00	0.00E+00	0.00E+00	0.00E+00	0.00E+00
Co	1.22E-06	3.07E-03	1.08E-02	1.92E-02	2.65E-02	3.25E-02	3.76E-02	4.24E-02	4.74E-02	5.26E-02	5.67E-02
Ni	2.51E-06	9.49E-05	5.58E-04	1.12E-03	1.63E-03	2.05E-03	2.35E-03	2.57E-03	2.72E-03	2.81E-03	2.74E-03
Cu	2.07E-06	4.25E-03	1.59E-02	2.88E-02	4.05E-02	5.03E-02	5.85E-02	6.59E-02	7.25E-02	7.88E-02	8.12E-02
Zn	6.38E-07	5.21E-04	3.68E-03	8.82E-03	1.48E-02	2.09E-02	2.68E-02	3.24E-02	3.76E-02	4.24E-02	4.41E-02
Ga	1.31E-06	3.53E-03	1.76E-02	4.14E-02	6.95E-02	9.87E-02	1.26E-01	1.52E-01	1.75E-01	1.96E-01	2.03E-01
Ge	1.09E-06	3.47E-03	1.72E-02	4.04E-02	6.82E-02	9.74E-02	1.25E-01	1.52E-01	1.75E-01	1.97E-01	2.04E-01
As	-2.59E-06	2.25E-03	1.13E-02	2.71E-02	4.64E-02	6.71E-02	8.73E-02	1.07E-01	1.24E-01	1.41E-01	1.46E-01
Se	2.66E-07	5.27E-03	2.65E-02	6.01E-02	9.81E-02	1.37E-01	1.72E-01	2.05E-01	2.35E-01	2.60E-01	2.69E-01
Br	-1.53E-06	2.29E-03	1.27E-02	3.29E-02	6.01E-02	8.93E-02	1.18E-01	1.45E-01	1.71E-01	1.94E-01	2.07E-01

Table 17—Continued

[El/Fe]	TDU 1	TDU 2	TDU 3	TDU 4	TDU 5	TDU 6	TDU 7	TDU 8	TDU 9	TDU 10	TDU 11
Kr	-1.24E-06	7.41E-03	3.71E-02	8.45E-02	1.38E-01	1.90E-01	2.38E-01	2.79E-01	3.17E-01	3.49E-01	3.60E-01
Rb	-7.85E-07	1.84E-02	7.11E-02	1.26E-01	1.75E-01	2.19E-01	2.57E-01	2.92E-01	3.23E-01	3.52E-01	3.62E-01
Sr	1.27E-06	2.02E-02	1.81E-01	4.13E-01	6.13E-01	7.67E-01	8.80E-01	9.67E-01	1.04E+00	1.09E+00	1.11E+00
Y	-3.40E-07	2.18E-02	1.85E-01	4.05E-01	5.95E-01	7.42E-01	8.51E-01	9.35E-01	1.00E+00	1.06E+00	1.08E+00
Zr	1.75E-08	1.45E-02	1.68E-01	3.95E-01	5.93E-01	7.42E-01	8.51E-01	9.33E-01	9.98E-01	1.05E+00	1.07E+00
Nb	-1.34E-06	-1.78E-04	4.65E-04	1.87E-02	6.66E-02	1.36E-01	2.10E-01	2.83E-01	3.50E-01	4.09E-01	8.61E-01
Mo	1.11E-06	4.02E-03	9.07E-02	2.59E-01	4.29E-01	5.65E-01	6.66E-01	7.42E-01	8.03E-01	8.51E-01	8.67E-01
Ru	6.44E-07	1.56E-03	6.41E-02	1.98E-01	3.47E-01	4.71E-01	5.66E-01	6.40E-01	6.98E-01	7.45E-01	7.62E-01
Rh	-8.37E-07	5.96E-04	3.23E-02	1.06E-01	1.97E-01	2.80E-01	3.48E-01	4.03E-01	4.48E-01	4.84E-01	4.96E-01
Pd	1.88E-06	2.32E-03	9.79E-02	2.82E-01	4.64E-01	6.04E-01	7.07E-01	7.84E-01	8.45E-01	8.93E-01	9.08E-01
Ag	-1.06E-06	4.42E-04	2.80E-02	9.42E-02	1.77E-01	2.54E-01	3.18E-01	3.69E-01	4.12E-01	4.47E-01	4.60E-01
Cd	1.54E-06	3.05E-03	1.20E-01	3.28E-01	5.24E-01	6.72E-01	7.79E-01	8.59E-01	9.22E-01	9.71E-01	9.87E-01
In	3.78E-07	1.78E-03	7.84E-02	2.32E-01	3.90E-01	5.18E-01	6.14E-01	6.86E-01	7.44E-01	7.89E-01	8.04E-01
Sn	-1.82E-07	2.85E-03	1.24E-01	3.42E-01	5.42E-01	6.92E-01	7.99E-01	8.78E-01	9.39E-01	9.87E-01	1.00E+00
Sb	-3.84E-07	1.01E-03	5.25E-02	1.57E-01	2.75E-01	3.76E-01	4.55E-01	5.17E-01	5.66E-01	6.06E-01	6.19E-01

Table 17—Continued

[El/Fe]	TDU 1	TDU 2	TDU 3	TDU 4	TDU 5	TDU 6	TDU 7	TDU 8	TDU 9	TDU 10	TDU 11
Te	-1.11E-06	4.15E-04	3.77E-02	1.32E-01	2.45E-01	3.43E-01	4.19E-01	4.76E-01	5.22E-01	5.58E-01	5.70E-01
I	-7.01E-07	-6.82E-05	1.04E-02	3.99E-02	8.14E-02	1.23E-01	1.60E-01	1.90E-01	2.15E-01	2.36E-01	2.43E-01
Xe	6.06E-07	2.84E-04	3.68E-02	1.29E-01	2.40E-01	3.37E-01	4.11E-01	4.69E-01	5.14E-01	5.50E-01	5.61E-01
Cs	-8.75E-07	6.77E-04	7.06E-02	1.69E-01	2.75E-01	3.68E-01	4.44E-01	5.04E-01	5.54E-01	5.94E-01	6.06E-01
Ba	1.34E-06	8.19E-04	1.26E-01	3.95E-01	6.30E-01	7.94E-01	9.05E-01	9.83E-01	1.04E+00	1.08E+00	1.10E+00
La	3.04E-06	3.47E-04	9.84E-02	3.42E-01	5.67E-01	7.27E-01	8.35E-01	9.11E-01	9.66E-01	1.01E+00	1.02E+00
Ce	1.27E-06	1.65E-04	7.25E-02	2.87E-01	5.00E-01	6.58E-01	7.66E-01	8.42E-01	8.98E-01	9.38E-01	9.51E-01
Pr	3.04E-07	4.76E-05	4.42E-02	1.72E-01	3.22E-01	4.47E-01	5.41E-01	6.10E-01	6.62E-01	7.02E-01	7.14E-01
Nd	1.85E-06	4.00E-05	4.21E-02	1.90E-01	3.60E-01	4.97E-01	5.95E-01	6.66E-01	7.19E-01	7.58E-01	7.69E-01
Sm	3.19E-07	-4.58E-05	1.86E-02	9.80E-02	2.06E-01	3.05E-01	3.83E-01	4.42E-01	4.87E-01	5.20E-01	5.30E-01
Eu	-1.83E-06	-1.98E-04	2.64E-03	1.67E-02	3.98E-02	6.56E-02	8.93E-02	1.09E-01	1.26E-01	1.39E-01	1.43E-01
Gd	5.50E-07	-7.72E-05	8.97E-03	5.04E-02	1.14E-01	1.75E-01	2.26E-01	2.65E-01	2.96E-01	3.20E-01	3.27E-01
Tb	-3.14E-07	-1.69E-04	4.25E-03	2.80E-02	6.68E-02	1.08E-01	1.44E-01	1.72E-01	1.95E-01	2.12E-01	2.18E-01
Dy	-1.13E-05	-1.17E-04	7.88E-03	4.95E-02	1.15E-01	1.80E-01	2.34E-01	2.77E-01	3.10E-01	3.34E-01	3.43E-01
Ho	4.64E-05	-6.19E-05	5.41E-03	3.39E-02	7.14E-02	1.07E-01	1.39E-01	1.61E-01	1.78E-01	1.92E-01	1.90E-01

Table 17—Continued

[El/Fe]	TDU 1	TDU 2	TDU 3	TDU 4	TDU 5	TDU 6	TDU 7	TDU 8	TDU 9	TDU 10	TDU 11
Er	7.22E-07	-7.44E-05	8.42E-03	5.15E-02	1.19E-01	1.88E-01	2.46E-01	2.91E-01	3.25E-01	3.52E-01	3.60E-01
Tm	2.01E-07	-1.37E-04	6.03E-03	4.16E-02	1.01E-01	1.64E-01	2.18E-01	2.62E-01	2.96E-01	3.22E-01	3.30E-01
Yb	9.04E-07	5.43E-05	2.01E-02	1.07E-01	2.26E-01	3.35E-01	4.20E-01	4.84E-01	5.33E-01	5.69E-01	5.80E-01
Lu	-1.14E-03	-1.24E-03	8.79E-03	5.78E-02	1.34E-01	2.10E-01	2.74E-01	3.25E-01	3.65E-01	3.95E-01	4.04E-01
Hf	2.39E-04	5.17E-04	2.68E-02	1.35E-01	2.77E-01	4.02E-01	4.97E-01	5.67E-01	6.20E-01	6.59E-01	6.71E-01
Ta	-1.45E-06	1.28E-04	1.90E-02	1.03E-01	2.24E-01	3.37E-01	4.26E-01	4.94E-01	5.46E-01	5.85E-01	5.96E-01
W	6.97E-08	4.22E-04	2.55E-02	1.35E-01	2.79E-01	4.07E-01	5.05E-01	5.77E-01	6.32E-01	6.72E-01	6.85E-01
Re	-6.54E-02	-6.54E-02	-5.75E-02	-2.72E-02	2.65E-02	8.61E-02	1.40E-01	1.86E-01	2.23E-01	2.53E-01	2.62E-01
Os	4.68E-03	4.60E-03	7.73E-03	2.71E-02	6.02E-02	9.70E-02	1.30E-01	1.57E-01	1.79E-01	1.96E-01	2.02E-01
Ir	-2.11E-06	-1.92E-04	-1.67E-04	2.30E-03	7.32E-03	1.34E-02	1.91E-02	2.39E-02	2.77E-02	3.05E-02	3.12E-02
Pt	7.70E-07	-8.61E-05	1.81E-03	1.49E-02	3.84E-02	6.56E-02	9.08E-02	1.12E-01	1.30E-01	1.44E-01	1.48E-01
Au	1.64E-06	-1.43E-04	1.27E-03	1.11E-02	2.96E-02	5.22E-02	7.41E-02	9.34E-02	1.10E-01	1.23E-01	1.27E-01
Hg	4.20E-06	3.68E-04	1.63E-02	9.73E-02	2.18E-01	3.34E-01	4.26E-01	4.96E-01	5.49E-01	5.90E-01	6.02E-01
Tl	7.47E-07	9.63E-04	1.88E-02	1.23E-01	2.78E-01	4.20E-01	5.30E-01	6.11E-01	6.70E-01	7.14E-01	7.26E-01
Pb	-1.19E-07	1.55E-04	5.12E-03	5.36E-02	1.54E-01	2.66E-01	3.61E-01	4.35E-01	4.90E-01	5.31E-01	5.43E-01

Table 17—Continued

[El/Fe]	TDU 1	TDU 2	TDU 3	TDU 4	TDU 5	TDU 6	TDU 7	TDU 8	TDU 9	TDU 10	TDU 11
Bi	5.21E-07	-2.18E-06	1.11E-04	2.10E-03	8.10E-03	1.76E-02	2.84E-02	3.91E-02	4.87E-02	5.68E-02	5.95E-02

Table 18. Pulse by pulse elemental surface composition of the $Z = 0.006$ model (online only).

[El/Fe]	TDU 1	TDU 2	TDU 3	TDU 4	TDU 5	TDU 6	TDU 7	TDU 8	TDU 9	TDU 10	TDU 11	TDU 12	TDU 13	TDU 14
C	-9.26E-02	1.47E-01	3.69E-01	5.41E-01	6.70E-01	7.71E-01	8.53E-01	9.22E-01	9.82E-01	1.03E+00	1.08E+00	1.13E+00	1.15E+00	1.17E+00
N	3.94E-01	3.94E-01	3.93E-01	3.92E-01	3.90E-01	3.89E-01	3.87E-01	3.86E-01	3.84E-01	3.83E-01	3.82E-01	3.82E-01	3.86E-01	3.97E-01
O	-4.65E-04	2.02E-03	6.21E-03	1.09E-02	1.50E-02	1.84E-02	2.10E-02	2.31E-02	2.48E-02	2.62E-02	2.74E-02	2.86E-02	2.90E-02	2.90E-02
F	-8.65E-03	4.79E-02	1.51E-01	2.70E-01	3.87E-01	4.96E-01	5.95E-01	6.87E-01	7.73E-01	8.51E-01	9.24E-01	9.98E-01	1.03E+00	1.06E+00
Ne	4.94E-04	1.82E-02	5.16E-02	9.57E-02	1.45E-01	1.97E-01	2.51E-01	3.04E-01	3.57E-01	4.09E-01	4.60E-01	5.13E-01	5.39E-01	5.58E-01
Na	1.14E-01	1.19E-01	1.27E-01	1.38E-01	1.52E-01	1.67E-01	1.85E-01	2.05E-01	2.28E-01	2.53E-01	2.82E-01	3.16E-01	3.37E-01	3.58E-01
Mg	1.58E-04	7.25E-04	1.92E-03	3.86E-03	6.57E-03	1.01E-02	1.46E-02	2.01E-02	2.68E-02	3.47E-02	4.41E-02	5.55E-02	6.22E-02	6.77E-02
Al	5.90E-04	1.63E-03	3.55E-03	6.10E-03	8.78E-03	1.15E-02	1.39E-02	1.63E-02	1.85E-02	2.04E-02	2.25E-02	2.46E-02	2.58E-02	2.72E-02
Si	5.64E-05	2.36E-04	4.79E-04	7.27E-04	9.55E-04	1.17E-03	1.38E-03	1.59E-03	1.81E-03	2.04E-03	2.28E-03	2.55E-03	2.68E-03	2.76E-03
P	7.75E-04	4.24E-03	9.83E-03	1.63E-02	2.24E-02	2.81E-02	3.32E-02	3.79E-02	4.25E-02	4.68E-02	5.11E-02	5.54E-02	5.73E-02	5.85E-02
S	1.75E-05	8.30E-05	1.91E-04	3.07E-04	4.19E-04	5.18E-04	6.06E-04	6.82E-04	7.51E-04	8.15E-04	8.71E-04	9.21E-04	9.45E-04	9.58E-04
Cl	3.74E-04	1.78E-03	3.74E-03	5.97E-03	8.20E-03	1.04E-02	1.27E-02	1.49E-02	1.72E-02	1.95E-02	2.18E-02	2.42E-02	2.54E-02	2.62E-02
Ar	-4.94E-05	-1.54E-04	-2.54E-04	-3.38E-04	-4.12E-04	-4.93E-04	-5.97E-04	-7.20E-04	-8.70E-04	-1.03E-03	-1.22E-03	-1.45E-03	-1.56E-03	-1.65E-03
K	1.55E-04	1.32E-03	2.91E-03	4.51E-03	6.25E-03	7.86E-03	9.74E-03	1.14E-02	1.33E-02	1.55E-02	1.74E-02	1.96E-02	2.10E-02	2.18E-02
Ca	-5.53E-05	-2.07E-04	-3.46E-04	-4.52E-04	-5.51E-04	-6.41E-04	-7.67E-04	-9.08E-04	-1.08E-03	-1.29E-03	-1.52E-03	-1.79E-03	-1.96E-03	-2.07E-03

105

Table 18—Continued

[El/Fe]	TDU 1	TDU 2	TDU 3	TDU 4	TDU 5	TDU 6	TDU 7	TDU 8	TDU 9	TDU 10	TDU 11	TDU 12	TDU 13	TDU 14
Sc	3.06E-03	9.71E-03	1.77E-02	2.59E-02	3.42E-02	4.28E-02	5.19E-02	6.15E-02	7.17E-02	8.21E-02	9.29E-02	1.04E-01	1.10E-01	1.14E-01
Ti	1.30E-04	1.05E-03	2.81E-03	5.09E-03	7.46E-03	9.74E-03	1.19E-02	1.39E-02	1.58E-02	1.76E-02	1.93E-02	2.10E-02	2.17E-02	2.22E-02
V	-1.69E-04	-3.83E-04	-3.61E-04	1.71E-05	6.93E-04	1.54E-03	2.44E-03	3.31E-03	4.13E-03	4.87E-03	5.53E-03	6.14E-03	6.42E-03	6.60E-03
Cr	3.06E-07	2.54E-05	8.76E-05	1.71E-04	2.59E-04	3.45E-04	4.27E-04	5.01E-04	5.71E-04	6.39E-04	7.04E-04	7.72E-04	8.04E-04	8.20E-04
Mn	-1.45E-04	-3.23E-04	-2.21E-04	3.71E-04	1.48E-03	2.99E-03	4.74E-03	6.65E-03	8.62E-03	1.06E-02	1.26E-02	1.47E-02	1.57E-02	1.65E-02
Fe	0.00E+00	0.00E+00	0.00E+00	0.00E+00	0.00E+00	0.00E+00	0.00E+00	0.00E+00	0.00E+00	0.00E+00	0.00E+00	0.00E+00	0.00E+00	0.00E+00
Co	5.40E-03	1.76E-02	3.03E-02	4.03E-02	4.95E-02	5.66E-02	6.59E-02	7.36E-02	8.27E-02	9.54E-02	1.06E-01	1.18E-01	1.29E-01	1.34E-01
Ni	1.82E-04	1.05E-03	2.00E-03	2.77E-03	3.22E-03	3.49E-03	3.54E-03	3.61E-03	3.63E-03	3.50E-03	3.52E-03	3.56E-03	3.36E-03	3.35E-03
Cu	7.33E-03	2.80E-02	4.88E-02	6.51E-02	7.71E-02	8.63E-02	9.44E-02	1.02E-01	1.10E-01	1.19E-01	1.28E-01	1.39E-01	1.44E-01	1.47E-01
Zn	6.89E-04	5.33E-03	1.24E-02	1.98E-02	2.62E-02	3.17E-02	3.67E-02	4.14E-02	4.60E-02	5.06E-02	5.54E-02	6.04E-02	6.26E-02	6.43E-02
Ga	4.39E-03	2.16E-02	4.89E-02	7.83E-02	1.04E-01	1.27E-01	1.48E-01	1.68E-01	1.86E-01	2.03E-01	2.20E-01	2.37E-01	2.44E-01	2.50E-01
Ge	4.33E-03	2.02E-02	4.59E-02	7.46E-02	1.01E-01	1.25E-01	1.47E-01	1.67E-01	1.87E-01	2.06E-01	2.25E-01	2.44E-01	2.52E-01	2.57E-01
As	2.85E-03	1.31E-02	3.03E-02	5.01E-02	6.86E-02	8.59E-02	1.02E-01	1.18E-01	1.33E-01	1.47E-01	1.62E-01	1.77E-01	1.83E-01	1.87E-01
Se	6.89E-03	3.08E-02	6.63E-02	1.05E-01	1.39E-01	1.69E-01	1.97E-01	2.23E-01	2.49E-01	2.72E-01	2.96E-01	3.19E-01	3.27E-01	3.34E-01
Br	3.00E-03	1.48E-02	3.82E-02	6.43E-02	9.34E-02	1.17E-01	1.45E-01	1.65E-01	1.86E-01	2.10E-01	2.29E-01	2.47E-01	2.61E-01	2.68E-01

Table 18—Continued

[El/Fe]	TDU 1	TDU 2	TDU 3	TDU 4	TDU 5	TDU 6	TDU 7	TDU 8	TDU 9	TDU 10	TDU 11	TDU 12	TDU 13	TDU 14
Kr	1.13E-02	4.92E-02	1.05E-01	1.63E-01	2.13E-01	2.57E-01	2.96E-01	3.31E-01	3.64E-01	3.95E-01	4.25E-01	4.54E-01	4.66E-01	4.74E-01
Rb	2.88E-02	9.82E-02	1.64E-01	2.19E-01	2.64E-01	3.04E-01	3.42E-01	3.79E-01	4.17E-01	4.55E-01	4.93E-01	5.31E-01	5.48E-01	5.57E-01
Sr	4.65E-02	2.56E-01	5.13E-01	7.17E-01	8.60E-01	9.66E-01	1.05E+00	1.12E+00	1.17E+00	1.22E+00	1.27E+00	1.31E+00	1.32E+00	1.33E+00
Y	5.73E-02	2.90E-01	5.38E-01	7.33E-01	8.72E-01	9.77E-01	1.06E+00	1.13E+00	1.19E+00	1.24E+00	1.29E+00	1.33E+00	1.35E+00	1.36E+00
Zr	5.21E-02	2.99E-01	5.68E-01	7.74E-01	9.18E-01	1.02E+00	1.11E+00	1.18E+00	1.23E+00	1.28E+00	1.33E+00	1.37E+00	1.38E+00	1.39E+00
Nb	-2.33E-04	3.83E-03	5.46E-02	1.33E-01	2.56E-01	3.41E-01	4.51E-01	5.14E-01	5.77E-01	6.59E-01	7.03E-01	7.46E-01	7.98E-01	1.05E-01
Mo	2.14E-02	1.90E-01	4.22E-01	6.18E-01	7.60E-01	8.66E-01	9.48E-01	1.01E+00	1.07E+00	1.12E+00	1.16E+00	1.20E+00	1.21E+00	1.22E+00
Ru	9.51E-03	1.39E-01	3.41E-01	5.22E-01	6.62E-01	7.66E-01	8.50E-01	9.15E-01	9.71E-01	1.02E+00	1.06E+00	1.10E+00	1.11E+00	1.12E+00
Rh	4.16E-03	7.20E-02	1.94E-01	3.20E-01	4.25E-01	5.08E-01	5.77E-01	6.33E-01	6.81E-01	7.23E-01	7.59E-01	7.92E-01	8.06E-01	8.13E-01
Pd	1.38E-02	2.04E-01	4.61E-01	6.71E-01	8.19E-01	9.29E-01	1.01E+00	1.08E+00	1.14E+00	1.19E+00	1.23E+00	1.27E+00	1.28E+00	1.29E+00
Ag	3.31E-03	6.31E-02	1.75E-01	2.94E-01	3.95E-01	4.76E-01	5.43E-01	5.98E-01	6.46E-01	6.88E-01	7.24E-01	7.57E-01	7.72E-01	7.79E-01
Cd	1.88E-02	2.50E-01	5.34E-01	7.56E-01	9.12E-01	1.03E+00	1.12E+00	1.19E+00	1.25E+00	1.30E+00	1.34E+00	1.38E+00	1.40E+00	1.41E+00
In	1.13E-02	1.72E-01	4.01E-01	5.98E-01	7.42E-01	8.51E-01	9.37E-01	1.01E+00	1.07E+00	1.11E+00	1.16E+00	1.20E+00	1.21E+00	1.22E+00
Sn	2.30E-02	2.88E-01	5.91E-01	8.19E-01	9.78E-01	1.09E+00	1.18E+00	1.25E+00	1.31E+00	1.36E+00	1.41E+00	1.45E+00	1.46E+00	1.47E+00
Sb	1.06E-02	1.46E-01	3.32E-01	5.00E-01	6.31E-01	7.35E-01	8.19E-01	8.89E-01	9.49E-01	1.00E+00	1.04E+00	1.09E+00	1.10E+00	1.11E+00

Table 18—Continued

[El/Fe]	TDU 1	TDU 2	TDU 3	TDU 4	TDU 5	TDU 6	TDU 7	TDU 8	TDU 9	TDU 10	TDU 11	TDU 12	TDU 13	TDU 14
Te	5.64E-03	1.12E-01	2.92E-01	4.60E-01	5.88E-01	6.85E-01	7.61E-01	8.22E-01	8.73E-01	9.16E-01	9.54E-01	9.88E-01	1.00E+00	1.01E+00
I	1.13E-03	3.40E-02	1.03E-01	1.85E-01	2.59E-01	3.23E-01	3.76E-01	4.22E-01	4.61E-01	4.96E-01	5.26E-01	5.54E-01	5.66E-01	5.72E-01
Xe	4.72E-03	1.22E-01	3.11E-01	4.85E-01	6.18E-01	7.19E-01	7.98E-01	8.62E-01	9.15E-01	9.61E-01	1.00E+00	1.04E+00	1.05E+00	1.06E+00
Cs	9.88E-03	2.42E-01	4.34E-01	5.96E-01	7.28E-01	8.40E-01	9.31E-01	1.01E+00	1.08E+00	1.13E+00	1.18E+00	1.22E+00	1.24E+00	1.25E+00
Ba	1.06E-02	5.27E-01	9.56E-01	1.23E+00	1.40E+00	1.53E+00	1.61E+00	1.68E+00	1.74E+00	1.78E+00	1.82E+00	1.85E+00	1.87E+00	1.87E+00
La	5.61E-03	5.39E-01	9.78E-01	1.25E+00	1.43E+00	1.55E+00	1.63E+00	1.70E+00	1.75E+00	1.79E+00	1.83E+00	1.86E+00	1.87E+00	1.88E+00
Ce	2.97E-03	5.73E-01	1.03E+00	1.30E+00	1.48E+00	1.60E+00	1.68E+00	1.74E+00	1.79E+00	1.83E+00	1.86E+00	1.89E+00	1.90E+00	1.91E+00
Pr	1.96E-03	4.29E-01	8.05E-01	1.06E+00	1.23E+00	1.35E+00	1.44E+00	1.50E+00	1.56E+00	1.60E+00	1.64E+00	1.67E+00	1.68E+00	1.69E+00
Nd	1.45E-03	4.80E-01	9.03E-01	1.17E+00	1.34E+00	1.46E+00	1.54E+00	1.60E+00	1.64E+00	1.68E+00	1.71E+00	1.74E+00	1.75E+00	1.76E+00
Sm	6.49E-04	3.15E-01	6.73E-01	9.24E-01	1.09E+00	1.20E+00	1.28E+00	1.33E+00	1.38E+00	1.41E+00	1.44E+00	1.47E+00	1.48E+00	1.49E+00
Eu	-1.52E-04	7.48E-02	2.14E-01	3.57E-01	4.73E-01	5.58E-01	6.21E-01	6.70E-01	7.08E-01	7.39E-01	7.65E-01	7.89E-01	7.98E-01	8.04E-01
Gd	2.58E-04	1.91E-01	4.67E-01	6.73E-01	8.14E-01	9.11E-01	9.81E-01	1.04E+00	1.08E+00	1.11E+00	1.14E+00	1.17E+00	1.18E+00	1.19E+00
Tb	-5.67E-05	1.13E-01	3.19E-01	5.01E-01	6.31E-01	7.20E-01	7.83E-01	8.30E-01	8.67E-01	8.96E-01	9.21E-01	9.44E-01	9.53E-01	9.59E-01
Dy	1.28E-04	1.78E-01	4.73E-01	6.87E-01	8.44E-01	9.42E-01	1.01E+00	1.06E+00	1.10E+00	1.13E+00	1.16E+00	1.18E+00	1.19E+00	1.20E+00
Ho	7.99E-05	1.36E-01	2.87E-01	5.02E-01	5.79E-01	6.73E-01	7.33E-01	7.82E-01	8.29E-01	8.47E-01	8.73E-01	8.98E-01	9.03E-01	9.08E-01

Table 18—Continued

[El/Fe]	TDU 1	TDU 2	TDU 3	TDU 4	TDU 5	TDU 6	TDU 7	TDU 8	TDU 9	TDU 10	TDU 11	TDU 12	TDU 13	TDU 14
Er	1.51E-04	1.90E-01	4.87E-01	7.17E-01	8.73E-01	9.78E-01	1.05E+00	1.11E+00	1.15E+00	1.18E+00	1.21E+00	1.24E+00	1.25E+00	1.25E+00
Tm	-3.08E-05	1.46E-01	4.25E-01	6.61E-01	8.24E-01	9.32E-01	1.00E+00	1.06E+00	1.10E+00	1.13E+00	1.15E+00	1.17E+00	1.18E+00	1.19E+00
Yb	5.28E-04	3.73E-01	7.62E-01	1.02E+00	1.19E+00	1.30E+00	1.38E+00	1.44E+00	1.48E+00	1.52E+00	1.55E+00	1.57E+00	1.58E+00	1.59E+00
Lu	-9.41E-04	2.33E-01	5.57E-01	7.97E-01	9.61E-01	1.07E+00	1.15E+00	1.20E+00	1.24E+00	1.28E+00	1.30E+00	1.33E+00	1.34E+00	1.34E+00
Hf	1.03E-03	4.85E-01	8.95E-01	1.16E+00	1.33E+00	1.44E+00	1.52E+00	1.57E+00	1.62E+00	1.65E+00	1.68E+00	1.70E+00	1.71E+00	1.72E+00
Ta	4.02E-04	3.99E-01	8.00E-01	1.07E+00	1.24E+00	1.36E+00	1.44E+00	1.49E+00	1.54E+00	1.57E+00	1.60E+00	1.63E+00	1.64E+00	1.64E+00
W	8.37E-04	4.92E-01	9.24E-01	1.19E+00	1.36E+00	1.48E+00	1.56E+00	1.61E+00	1.66E+00	1.69E+00	1.72E+00	1.75E+00	1.76E+00	1.76E+00
Re	-6.11E-02	1.64E-01	4.38E-01	6.62E-01	8.27E-01	9.43E-01	1.03E+00	1.09E+00	1.14E+00	1.17E+00	1.21E+00	1.23E+00	1.24E+00	1.25E+00
Os	4.33E-03	1.23E-01	3.37E-01	5.20E-01	6.50E-01	7.40E-01	8.04E-01	8.51E-01	8.87E-01	9.16E-01	9.40E-01	9.62E-01	9.70E-01	9.75E-01
Ir	-2.65E-04	2.16E-02	7.54E-02	1.40E-01	1.98E-01	2.45E-01	2.81E-01	3.09E-01	3.32E-01	3.50E-01	3.66E-01	3.80E-01	3.86E-01	3.89E-01
Pt	-7.59E-05	8.15E-02	2.50E-01	4.09E-01	5.28E-01	6.11E-01	6.70E-01	7.13E-01	7.47E-01	7.73E-01	7.96E-01	8.16E-01	8.23E-01	8.28E-01
Au	-1.70E-04	6.77E-02	2.14E-01	3.63E-01	4.82E-01	5.67E-01	6.28E-01	6.73E-01	7.08E-01	7.36E-01	7.58E-01	7.78E-01	7.86E-01	7.91E-01
Hg	6.03E-04	4.33E-01	8.53E-01	1.12E+00	1.29E+00	1.40E+00	1.47E+00	1.53E+00	1.57E+00	1.60E+00	1.62E+00	1.65E+00	1.66E+00	1.66E+00
Tl	1.31E-03	5.27E-01	1.00E+00	1.28E+00	1.46E+00	1.57E+00	1.64E+00	1.69E+00	1.73E+00	1.76E+00	1.78E+00	1.80E+00	1.81E+00	1.81E+00
Pb	3.05E-04	3.15E-01	7.41E-01	1.03E+00	1.21E+00	1.33E+00	1.41E+00	1.46E+00	1.50E+00	1.54E+00	1.56E+00	1.58E+00	1.59E+00	1.59E+00

Table 18—Continued

[El/Fe]	TDU 1	TDU 2	TDU 3	TDU 4	TDU 5	TDU 6	TDU 7	TDU 8	TDU 9	TDU 10	TDU 11	TDU 12	TDU 13	TDU 14
Bi	9.93E-06	1.68E-02	8.52E-02	1.93E-01	3.02E-01	3.91E-01	4.61E-01	5.15E-01	5.57E-01	5.91E-01	6.19E-01	6.43E-01	6.53E-01	6.58E-01

Table 19. Pulse by pulse elemental surface composition of the $Z = 0.003$ model (online only).

[El/Fe]	TDU 1	TDU 2	TDU 3	TDU 4	TDU 5	TDU 6	TDU 7	TDU 8	TDU 9	TDU 10	TDU 11	TDU 12	TDU 13	TDU 14	TDU 15	TDU 16
C	-3.51E-02	3.41E-01	6.18E-01	8.12E-01	9.53E-01	1.06E+00	1.15E+00	1.22E+00	1.28E+00	1.33E+00	1.38E+00	1.42E+00	1.46E+00	1.50E+00	1.53E+00	1.54E+00
N	4.16E-01	4.15E-01	4.15E-01	4.14E-01	4.13E-01	4.12E-01	4.11E-01	4.10E-01	4.10E-01	4.10E-01	4.10E-01	4.10E-01	4.11E-01	4.14E-01	4.20E-01	4.38E-01
O	-1.42E-03	4.43E-03	1.41E-02	2.49E-02	3.49E-02	4.34E-02	5.05E-02	5.65E-02	6.19E-02	6.68E-02	7.14E-02	7.58E-02	8.01E-02	8.44E-02	8.87E-02	8.97E-02
F	-1.81E-02	1.03E-01	2.82E-01	4.52E-01	5.99E-01	7.27E-01	8.39E-01	9.38E-01	1.03E+00	1.11E+00	1.19E+00	1.26E+00	1.32E+00	1.39E+00	1.45E+00	1.47E+00
Ne	-8.52E-04	2.64E-02	7.96E-02	1.48E-01	2.23E-01	2.97E-01	3.70E-01	4.41E-01	5.09E-01	5.74E-01	6.36E-01	6.97E-01	7.54E-01	8.10E-01	8.63E-01	8.81E-01
Na	1.37E-01	1.41E-01	1.50E-01	1.65E-01	1.83E-01	2.05E-01	2.30E-01	2.58E-01	2.89E-01	3.23E-01	3.61E-01	4.03E-01	4.47E-01	4.95E-01	5.45E-01	5.70E-01
Mg	2.71E-04	1.29E-03	3.36E-03	6.64E-03	1.12E-02	1.72E-02	2.48E-02	3.41E-02	4.55E-02	5.89E-02	7.47E-02	9.30E-02	1.13E-01	1.36E-01	1.60E-01	1.70E-01
Al	8.66E-04	2.82E-03	6.22E-03	1.03E-02	1.44E-02	1.81E-02	2.13E-02	2.43E-02	2.70E-02	2.96E-02	3.21E-02	3.46E-02	3.70E-02	3.96E-02	4.24E-02	4.41E-02
Si	6.20E-05	3.40E-04	6.68E-04	9.82E-04	1.28E-03	1.55E-03	1.83E-03	2.10E-03	2.39E-03	2.70E-03	3.04E-03	3.40E-03	3.77E-03	4.17E-03	4.58E-03	4.71E-03
P	9.60E-04	6.39E-03	1.43E-02	2.28E-02	3.08E-02	3.80E-02	4.46E-02	5.06E-02	5.64E-02	6.19E-02	6.74E-02	7.29E-02	7.83E-02	8.37E-02	8.88E-02	9.02E-02
S	1.76E-05	1.31E-04	2.79E-04	4.30E-04	5.65E-04	6.74E-04	7.67E-04	8.42E-04	9.05E-04	9.61E-04	1.01E-03	1.06E-03	1.10E-03	1.15E-03	1.19E-03	1.20E-03
Cl	2.85E-04	1.72E-03	3.58E-03	5.64E-03	7.79E-03	9.94E-03	1.20E-02	1.42E-02	1.63E-02	1.84E-02	2.06E-02	2.28E-02	2.50E-02	2.72E-02	2.95E-02	3.02E-02
Ar	-4.74E-05	-1.49E-04	-2.47E-04	-3.38E-04	-4.40E-04	-5.68E-04	-7.19E-04	-9.07E-04	-1.12E-03	-1.35E-03	-1.61E-03	-1.89E-03	-2.19E-03	-2.49E-03	-2.81E-03	-2.91E-03
K	2.05E-04	1.75E-03	3.54E-03	5.30E-03	7.09E-03	8.93E-03	1.11E-02	1.29E-02	1.51E-02	1.73E-02	1.95E-02	2.20E-02	2.46E-02	2.71E-02	2.97E-02	3.08E-02
Ca	-5.99E-05	-2.25E-04	-3.81E-04	-5.09E-04	-6.39E-04	-7.95E-04	-1.00E-03	-1.22E-03	-1.49E-03	-1.80E-03	-2.13E-03	-2.50E-03	-2.90E-03	-3.30E-03	-3.73E-03	-3.88E-03

Table 19—Continued

[El/Fe]	TDU 1	TDU 2	TDU 3	TDU 4	TDU 5	TDU 6	TDU 7	TDU 8	TDU 9	TDU 10	TDU 11	TDU 12	TDU 13	TDU 14	TDU 15	TDU 16
Sc	3.53E-03	1.28E-02	2.27E-02	3.23E-02	4.21E-02	5.25E-02	6.35E-02	7.51E-02	8.73E-02	9.99E-02	1.13E-01	1.26E-01	1.40E-01	1.53E-01	1.66E-01	1.70E-01
Ti	1.43E-04	1.42E-03	3.59E-03	6.22E-03	8.98E-03	1.16E-02	1.42E-02	1.65E-02	1.88E-02	2.09E-02	2.30E-02	2.50E-02	2.70E-02	2.89E-02	3.06E-02	3.11E-02
V	-1.40E-04	-2.92E-04	-1.22E-04	4.82E-04	1.39E-03	2.38E-03	3.31E-03	4.12E-03	4.80E-03	5.34E-03	5.75E-03	6.04E-03	6.25E-03	6.39E-03	6.46E-03	6.48E-03
Cr	-3.04E-06	4.55E-05	1.41E-04	2.65E-04	3.99E-04	5.27E-04	6.55E-04	7.73E-04	8.87E-04	1.00E-03	1.11E-03	1.22E-03	1.34E-03	1.45E-03	1.56E-03	1.59E-03
Mn	-1.47E-04	-3.69E-04	-2.11E-04	5.92E-04	1.98E-03	3.70E-03	5.54E-03	7.35E-03	9.08E-03	1.07E-02	1.22E-02	1.36E-02	1.49E-02	1.62E-02	1.75E-02	1.80E-02
Fe	0.00E+00	0.00E+00	0.00E+00	0.00E+00	0.00E+00	0.00E+00	0.00E+00	0.00E+00	0.00E+00	0.00E+00	0.00E+00	0.00E+00	0.00E+00	0.00E+00	0.00E+00	0.00E+00
Co	6.39E-03	2.21E-02	3.71E-02	4.86E-02	5.84E-02	6.82E-02	8.19E-02	9.18E-02	1.07E-01	1.22E-01	1.38E-01	1.56E-01	1.76E-01	1.95E-01	2.14E-01	2.22E-01
Ni	2.63E-04	1.80E-03	3.33E-03	4.44E-03	5.10E-03	5.41E-03	5.42E-03	5.57E-03	5.55E-03	5.61E-03	5.81E-03	6.00E-03	6.26E-03	6.73E-03	7.20E-03	7.26E-03
Cu	9.27E-03	4.61E-02	7.82E-02	1.01E-01	1.16E-01	1.27E-01	1.37E-01	1.46E-01	1.56E-01	1.67E-01	1.80E-01	1.94E-01	2.09E-01	2.25E-01	2.42E-01	2.47E-01
Zn	8.14E-04	8.45E-03	1.85E-02	2.80E-02	3.55E-02	4.14E-02	4.62E-02	5.04E-02	5.44E-02	5.84E-02	6.26E-02	6.70E-02	7.18E-02	7.71E-02	8.24E-02	8.41E-02
Ga	3.89E-03	2.92E-02	5.94E-02	8.71E-02	1.10E-01	1.29E-01	1.45E-01	1.60E-01	1.74E-01	1.87E-01	2.01E-01	2.14E-01	2.27E-01	2.41E-01	2.54E-01	2.58E-01
Ge	3.49E-03	2.34E-02	4.84E-02	7.31E-02	9.54E-02	1.15E-01	1.32E-01	1.48E-01	1.63E-01	1.78E-01	1.92E-01	2.06E-01	2.20E-01	2.35E-01	2.48E-01	2.52E-01
As	2.20E-03	1.38E-02	2.92E-02	4.50E-02	5.98E-02	7.34E-02	8.58E-02	9.73E-02	1.08E-01	1.19E-01	1.30E-01	1.41E-01	1.51E-01	1.63E-01	1.73E-01	1.75E-01
Se	5.29E-03	3.02E-02	6.00E-02	8.92E-02	1.16E-01	1.40E-01	1.62E-01	1.82E-01	2.02E-01	2.20E-01	2.39E-01	2.56E-01	2.73E-01	2.92E-01	3.07E-01	3.11E-01
Br	2.37E-03	1.45E-02	3.28E-02	5.22E-02	7.24E-02	9.22E-02	1.15E-01	1.29E-01	1.48E-01	1.64E-01	1.78E-01	1.94E-01	2.10E-01	2.23E-01	2.36E-01	2.43E-01

Table 19—Continued

[El/Fe]	TDU 1	TDU 2	TDU 3	TDU 4	TDU 5	TDU 6	TDU 7	TDU 8	TDU 9	TDU 10	TDU 11	TDU 12	TDU 13	TDU 14	TDU 15	TDU 16
Kr	9.75E-03	5.06E-02	1.00E-01	1.46E-01	1.88E-01	2.24E-01	2.55E-01	2.84E-01	3.12E-01	3.38E-01	3.64E-01	3.88E-01	4.12E-01	4.37E-01	4.58E-01	4.64E-01
Rb	2.78E-02	1.11E-01	1.78E-01	2.28E-01	2.71E-01	3.11E-01	3.51E-01	3.90E-01	4.30E-01	4.70E-01	5.10E-01	5.49E-01	5.87E-01	6.24E-01	6.56E-01	6.64E-01
Sr	4.20E-02	2.33E-01	4.39E-01	6.04E-01	7.32E-01	8.31E-01	9.09E-01	9.72E-01	1.03E+00	1.08E+00	1.12E+00	1.16E+00	1.19E+00	1.23E+00	1.25E+00	1.26E+00
Y	5.65E-02	2.76E-01	4.82E-01	6.43E-01	7.67E-01	8.66E-01	9.46E-01	1.01E+00	1.07E+00	1.13E+00	1.17E+00	1.22E+00	1.26E+00	1.29E+00	1.32E+00	1.33E+00
Zr	6.29E-02	3.02E-01	5.24E-01	6.92E-01	8.19E-01	9.17E-01	9.96E-01	1.06E+00	1.12E+00	1.17E+00	1.22E+00	1.26E+00	1.30E+00	1.34E+00	1.37E+00	1.38E+00
Nb	9.58E-04	9.42E-03	5.04E-02	1.12E-01	1.88E-01	2.68E-01	3.83E-01	4.21E-01	4.98E-01	5.57E-01	5.98E-01	6.51E-01	7.05E-01	7.37E-01	7.74E-01	8.03E-01
Mo	3.27E-02	1.98E-01	3.88E-01	5.47E-01	6.70E-01	7.65E-01	8.41E-01	9.03E-01	9.57E-01	1.00E+00	1.05E+00	1.08E+00	1.12E+00	1.15E+00	1.18E+00	1.19E+00
Ru	1.61E-02	1.43E-01	3.06E-01	4.52E-01	5.72E-01	6.67E-01	7.47E-01	8.08E-01	8.64E-01	9.11E-01	9.52E-01	9.90E-01	1.02E+00	1.06E+00	1.08E+00	1.09E+00
Rh	6.95E-03	7.32E-02	1.70E-01	2.69E-01	3.56E-01	4.28E-01	4.89E-01	5.40E-01	5.85E-01	6.25E-01	6.61E-01	6.94E-01	7.23E-01	7.51E-01	7.75E-01	7.81E-01
Pd	2.14E-02	2.10E-01	4.20E-01	5.91E-01	7.22E-01	8.23E-01	9.04E-01	9.70E-01	1.03E+00	1.08E+00	1.12E+00	1.16E+00	1.19E+00	1.23E+00	1.25E+00	1.26E+00
Ag	5.08E-03	6.40E-02	1.53E-01	2.45E-01	3.28E-01	3.98E-01	4.58E-01	5.08E-01	5.53E-01	5.93E-01	6.28E-01	6.60E-01	6.90E-01	7.17E-01	7.41E-01	7.48E-01
Cd	2.63E-02	2.50E-01	4.87E-01	6.74E-01	8.16E-01	9.25E-01	1.01E+00	1.08E+00	1.15E+00	1.20E+00	1.25E+00	1.29E+00	1.33E+00	1.36E+00	1.39E+00	1.40E+00
In	1.48E-02	1.66E-01	3.55E-01	5.19E-01	6.51E-01	7.55E-01	8.38E-01	9.08E-01	9.67E-01	1.02E+00	1.07E+00	1.11E+00	1.14E+00	1.18E+00	1.20E+00	1.21E+00
Sn	3.68E-02	2.85E-01	5.38E-01	7.33E-01	8.79E-01	9.92E-01	1.08E+00	1.16E+00	1.22E+00	1.27E+00	1.32E+00	1.37E+00	1.41E+00	1.44E+00	1.48E+00	1.48E+00
Sb	1.94E-02	1.49E-01	3.02E-01	4.45E-01	5.67E-01	6.69E-01	7.54E-01	8.28E-01	8.92E-01	9.50E-01	1.00E+00	1.05E+00	1.09E+00	1.13E+00	1.16E+00	1.17E+00

Table 19—Continued

[El/Fe]	TDU 1	TDU 2	TDU 3	TDU 4	TDU 5	TDU 6	TDU 7	TDU 8	TDU 9	TDU 10	TDU 11	TDU 12	TDU 13	TDU 14	TDU 15	TDU 16
Te	1.12E-02	1.11E-01	2.56E-01	3.93E-01	5.04E-01	5.93E-01	6.66E-01	7.26E-01	7.79E-01	8.25E-01	8.66E-01	9.04E-01	9.37E-01	9.69E-01	9.96E-01	1.00E+00
I	2.66E-03	3.35E-02	8.83E-02	1.52E-01	2.14E-01	2.70E-01	3.19E-01	3.62E-01	4.01E-01	4.35E-01	4.67E-01	4.96E-01	5.22E-01	5.47E-01	5.69E-01	5.75E-01
Xe	1.10E-02	1.23E-01	2.77E-01	4.21E-01	5.38E-01	6.33E-01	7.11E-01	7.77E-01	8.34E-01	8.84E-01	9.29E-01	9.69E-01	1.01E+00	1.04E+00	1.07E+00	1.07E+00
Cs	1.85E-02	2.12E-01	3.79E-01	5.32E-01	6.69E-01	7.86E-01	8.81E-01	9.64E-01	1.03E+00	1.09E+00	1.15E+00	1.19E+00	1.24E+00	1.27E+00	1.30E+00	1.31E+00
Ba	3.10E-02	5.65E-01	9.56E-01	1.21E+00	1.38E+00	1.51E+00	1.61E+00	1.69E+00	1.75E+00	1.81E+00	1.86E+00	1.90E+00	1.94E+00	1.97E+00	2.00E+00	2.01E+00
La	2.13E-02	5.91E-01	9.99E-01	1.26E+00	1.43E+00	1.56E+00	1.66E+00	1.74E+00	1.80E+00	1.86E+00	1.90E+00	1.95E+00	1.98E+00	2.02E+00	2.04E+00	2.05E+00
Ce	1.34E-02	6.71E-01	1.10E+00	1.37E+00	1.55E+00	1.67E+00	1.77E+00	1.85E+00	1.91E+00	1.97E+00	2.01E+00	2.05E+00	2.09E+00	2.12E+00	2.15E+00	2.15E+00
Pr	8.80E-03	5.21E-01	8.91E-01	1.14E+00	1.32E+00	1.46E+00	1.56E+00	1.64E+00	1.71E+00	1.77E+00	1.82E+00	1.87E+00	1.91E+00	1.94E+00	1.97E+00	1.98E+00
Nd	8.21E-03	5.95E-01	1.01E+00	1.27E+00	1.44E+00	1.57E+00	1.67E+00	1.74E+00	1.81E+00	1.86E+00	1.90E+00	1.94E+00	1.98E+00	2.01E+00	2.03E+00	2.04E+00
Sm	4.89E-03	4.35E-01	8.03E-01	1.05E+00	1.22E+00	1.34E+00	1.43E+00	1.50E+00	1.56E+00	1.61E+00	1.66E+00	1.70E+00	1.73E+00	1.77E+00	1.79E+00	1.80E+00
Eu	6.43E-04	1.17E-01	2.90E-01	4.51E-01	5.80E-01	6.79E-01	7.58E-01	8.23E-01	8.78E-01	9.25E-01	9.67E-01	1.01E+00	1.04E+00	1.07E+00	1.09E+00	1.10E+00
Gd	2.55E-03	2.82E-01	5.76E-01	7.82E-01	9.31E-01	1.05E+00	1.14E+00	1.21E+00	1.28E+00	1.33E+00	1.38E+00	1.42E+00	1.46E+00	1.49E+00	1.52E+00	1.53E+00
Tb	1.15E-03	1.77E-01	4.16E-01	6.02E-01	7.35E-01	8.34E-01	9.11E-01	9.75E-01	1.03E+00	1.08E+00	1.12E+00	1.16E+00	1.19E+00	1.22E+00	1.25E+00	1.26E+00
Dy	2.24E-03	2.78E-01	5.88E-01	8.06E-01	9.58E-01	1.07E+00	1.15E+00	1.22E+00	1.27E+00	1.32E+00	1.36E+00	1.40E+00	1.43E+00	1.46E+00	1.48E+00	1.49E+00
Ho	8.11E-04	1.51E-01	3.78E-01	5.89E-01	7.22E-01	8.17E-01	8.75E-01	9.42E-01	9.90E-01	1.03E+00	1.08E+00	1.11E+00	1.14E+00	1.17E+00	1.19E+00	1.20E+00

Table 19—Continued

[El/Fe]	TDU 1	TDU 2	TDU 3	TDU 4	TDU 5	TDU 6	TDU 7	TDU 8	TDU 9	TDU 10	TDU 11	TDU 12	TDU 13	TDU 14	TDU 15	TDU 16
Er	2.07E-03	2.85E-01	6.12E-01	8.46E-01	1.01E+00	1.13E+00	1.22E+00	1.29E+00	1.35E+00	1.40E+00	1.44E+00	1.48E+00	1.51E+00	1.54E+00	1.57E+00	1.57E+00
Tm	1.23E-03	2.21E-01	5.48E-01	7.94E-01	9.57E-01	1.07E+00	1.15E+00	1.22E+00	1.27E+00	1.31E+00	1.35E+00	1.38E+00	1.41E+00	1.44E+00	1.46E+00	1.47E+00
Yb	4.19E-03	5.06E-01	9.06E-01	1.17E+00	1.34E+00	1.47E+00	1.56E+00	1.64E+00	1.70E+00	1.75E+00	1.80E+00	1.84E+00	1.87E+00	1.90E+00	1.92E+00	1.93E+00
Lu	7.71E-04	3.29E-01	6.86E-01	9.36E-01	1.11E+00	1.23E+00	1.32E+00	1.39E+00	1.45E+00	1.49E+00	1.53E+00	1.57E+00	1.60E+00	1.63E+00	1.65E+00	1.66E+00
Hf	5.19E-03	6.55E-01	1.06E+00	1.32E+00	1.49E+00	1.62E+00	1.71E+00	1.79E+00	1.85E+00	1.90E+00	1.94E+00	1.98E+00	2.02E+00	2.05E+00	2.07E+00	2.08E+00
Ta	2.99E-03	5.59E-01	9.75E-01	1.24E+00	1.42E+00	1.55E+00	1.64E+00	1.71E+00	1.77E+00	1.82E+00	1.86E+00	1.90E+00	1.93E+00	1.96E+00	1.98E+00	1.99E+00
W	3.89E-03	6.77E-01	1.11E+00	1.38E+00	1.55E+00	1.68E+00	1.78E+00	1.85E+00	1.91E+00	1.96E+00	2.00E+00	2.04E+00	2.07E+00	2.10E+00	2.12E+00	2.13E+00
Re	-5.86E-02	2.89E-01	6.10E-01	8.57E-01	1.04E+00	1.17E+00	1.27E+00	1.35E+00	1.42E+00	1.47E+00	1.51E+00	1.55E+00	1.58E+00	1.61E+00	1.64E+00	1.65E+00
Os	4.65E-03	2.04E-01	4.63E-01	6.62E-01	8.06E-01	9.13E-01	9.97E-01	1.06E+00	1.12E+00	1.17E+00	1.21E+00	1.24E+00	1.28E+00	1.30E+00	1.33E+00	1.33E+00
Ir	-1.69E-04	4.08E-02	1.20E-01	2.08E-01	2.88E-01	3.56E-01	4.13E-01	4.62E-01	5.03E-01	5.39E-01	5.71E-01	6.00E-01	6.25E-01	6.48E-01	6.68E-01	6.73E-01
Pt	1.92E-04	1.47E-01	3.67E-01	5.49E-01	6.84E-01	7.85E-01	8.64E-01	9.27E-01	9.80E-01	1.03E+00	1.06E+00	1.10E+00	1.13E+00	1.16E+00	1.18E+00	1.18E+00
Au	1.09E-05	1.23E-01	3.25E-01	5.08E-01	6.49E-01	7.54E-01	8.34E-01	8.98E-01	9.49E-01	9.92E-01	1.03E+00	1.06E+00	1.09E+00	1.11E+00	1.13E+00	1.14E+00
Hg	1.52E-03	6.41E-01	1.08E+00	1.34E+00	1.52E+00	1.65E+00	1.74E+00	1.81E+00	1.87E+00	1.92E+00	1.96E+00	2.00E+00	2.03E+00	2.05E+00	2.08E+00	2.08E+00
Tl	1.75E-03	7.92E-01	1.27E+00	1.56E+00	1.74E+00	1.86E+00	1.95E+00	2.02E+00	2.08E+00	2.12E+00	2.16E+00	2.20E+00	2.22E+00	2.25E+00	2.27E+00	2.27E+00
Pb	4.89E-04	9.40E-01	1.45E+00	1.74E+00	1.91E+00	2.02E+00	2.09E+00	2.15E+00	2.19E+00	2.22E+00	2.25E+00	2.27E+00	2.29E+00	2.31E+00	2.32E+00	2.32E+00

Table 19—Continued

[El/Fe]	TDU 1	TDU 2	TDU 3	TDU 4	TDU 5	TDU 6	TDU 7	TDU 8	TDU 9	TDU 10	TDU 11	TDU 12	TDU 13	TDU 14	TDU 15	TDU 16
Bi	1.98E-05	2.93E-01	6.44E-01	8.91E-01	1.05E+00	1.17E+00	1.24E+00	1.30E+00	1.34E+00	1.38E+00	1.41E+00	1.43E+00	1.46E+00	1.47E+00	1.49E+00	1.50E+00

Table 20. Pulse by pulse elemental surface composition of the $Z = 0.001$ model (online only).

[El/Fe]	TDU 1	TDU 2	TDU 3	TDU 4	TDU 5	TDU 6	TDU 7	TDU 8	TDU 9	TDU 10	TDU 11	TDU 12	TDU 13	TDU 15	TDU 17	TDU 19
C	-2.13E-01	5.67E-01	9.88E-01	1.25E+00	1.43E+00	1.56E+00	1.66E+00	1.74E+00	1.80E+00	1.86E+00	1.91E+00	1.95E+00	1.99E+00	2.06E+00	2.13E+00	2.18E+00
N	4.59E-01	4.59E-01	4.58E-01	4.58E-01	4.58E-01	4.59E-01	4.59E-01	4.61E-01	4.62E-01	4.65E-01	4.68E-01	4.72E-01	4.76E-01	4.88E-01	5.09E-01	5.56E-01
O	-9.12E-03	4.42E-03	3.39E-02	7.04E-02	1.05E-01	1.35E-01	1.59E-01	1.79E-01	1.96E-01	2.12E-01	2.27E-01	2.40E-01	2.53E-01	2.78E-01	3.02E-01	3.22E-01
F	-3.85E-02	3.32E-01	6.98E-01	9.50E-01	1.14E+00	1.28E+00	1.40E+00	1.51E+00	1.60E+00	1.68E+00	1.76E+00	1.83E+00	1.89E+00	2.02E+00	2.13E+00	2.22E+00
Ne	-5.32E-03	5.01E-02	1.75E-01	3.21E-01	4.64E-01	5.98E-01	7.21E-01	8.32E-01	9.32E-01	1.03E+00	1.11E+00	1.19E+00	1.26E+00	1.39E+00	1.51E+00	1.60E+00
Na	1.67E-01	1.73E-01	1.94E-01	2.32E-01	2.82E-01	3.41E-01	4.06E-01	4.75E-01	5.46E-01	6.20E-01	6.94E-01	7.69E-01	8.43E-01	9.94E-01	1.15E+00	1.28E+00
Mg	9.40E-05	1.12E-03	5.20E-03	1.47E-02	3.06E-02	5.35E-02	8.36E-02	1.21E-01	1.65E-01	2.16E-01	2.70E-01	3.27E-01	3.85E-01	5.04E-01	6.22E-01	7.19E-01
Al	2.91E-03	1.16E-02	2.74E-02	4.38E-02	5.73E-02	6.79E-02	7.65E-02	8.40E-02	9.08E-02	9.79E-02	1.05E-01	1.12E-01	1.20E-01	1.38E-01	1.58E-01	1.79E-01
Si	7.01E-06	4.65E-04	1.14E-03	1.88E-03	2.63E-03	3.37E-03	4.12E-03	4.92E-03	5.77E-03	6.71E-03	7.68E-03	8.69E-03	9.75E-03	1.20E-02	1.43E-02	1.63E-02
P	2.56E-06	7.25E-03	2.10E-02	3.81E-02	5.48E-02	6.93E-02	8.16E-02	9.28E-02	1.03E-01	1.14E-01	1.24E-01	1.34E-01	1.44E-01	1.63E-01	1.82E-01	1.96E-01
S	2.56E-06	1.44E-04	3.88E-04	6.56E-04	8.91E-04	1.07E-03	1.19E-03	1.29E-03	1.38E-03	1.47E-03	1.56E-03	1.66E-03	1.76E-03	1.95E-03	2.18E-03	2.38E-03
Cl	1.53E-05	9.81E-04	2.56E-03	4.63E-03	6.96E-03	9.36E-03	1.19E-02	1.44E-02	1.69E-02	1.96E-02	2.22E-02	2.49E-02	2.76E-02	3.30E-02	3.87E-02	4.37E-02
Ar	2.56E-06	-6.86E-05	-1.54E-04	-2.75E-04	-4.76E-04	-7.66E-04	-1.14E-03	-1.57E-03	-1.97E-03	-2.46E-03	-2.91E-03	-3.37E-03	-3.82E-03	-4.73E-03	-5.64E-03	-6.41E-03
K	-1.91E-04	1.52E-03	3.90E-03	6.37E-03	8.89E-03	1.18E-02	1.48E-02	1.83E-02	2.11E-02	2.59E-02	2.98E-02	3.38E-02	3.78E-02	4.60E-02	5.41E-02	6.09E-02
Ca	1.37E-05	-1.73E-04	-3.89E-04	-6.12E-04	-8.98E-04	-1.30E-03	-1.80E-03	-2.38E-03	-2.99E-03	-3.65E-03	-4.31E-03	-4.97E-03	-5.64E-03	-7.01E-03	-8.36E-03	-9.51E-03

Table 20—Continued

[El/Fe]	TDU 1	TDU 2	TDU 3	TDU 4	TDU 5	TDU 6	TDU 7	TDU 8	TDU 9	TDU 10	TDU 11	TDU 12	TDU 13	TDU 15	TDU 17	TDU 19
Sc	1.83E-05	1.49E-02	3.06E-02	4.56E-02	6.16E-02	7.93E-02	9.90E-02	1.20E-01	1.42E-01	1.65E-01	1.88E-01	2.10E-01	2.31E-01	2.71E-01	3.08E-01	3.35E-01
Ti	2.56E-06	1.08E-03	3.21E-03	6.04E-03	9.05E-03	1.19E-02	1.45E-02	1.71E-02	1.95E-02	2.21E-02	2.47E-02	2.72E-02	2.97E-02	3.47E-02	4.00E-02	4.42E-02
V	7.19E-06	-6.72E-05	2.34E-04	9.95E-04	1.82E-03	2.33E-03	2.44E-03	2.29E-03	1.99E-03	1.61E-03	1.20E-03	7.66E-04	3.29E-04	-6.33E-04	-1.49E-03	-2.17E-03
Cr	2.56E-06	3.27E-05	1.25E-04	2.73E-04	4.48E-04	6.42E-04	8.35E-04	1.04E-03	1.24E-03	1.46E-03	1.69E-03	1.91E-03	2.15E-03	2.61E-03	3.08E-03	3.46E-03
Mn	1.48E-05	-2.21E-04	3.09E-05	1.12E-03	2.68E-03	4.13E-03	5.16E-03	5.79E-03	6.12E-03	6.26E-03	6.28E-03	6.24E-03	6.16E-03	6.06E-03	6.23E-03	6.94E-03
Fe	0.00E+00	0.00E+00	0.00E+00	0.00E+00	0.00E+00	0.00E+00	0.00E+00	0.00E+00	0.00E+00	0.00E+00	0.00E+00	0.00E+00	0.00E+00	0.00E+00	0.00E+00	0.00E+00
Co	7.54E-06	2.01E-02	4.16E-02	5.89E-02	7.57E-02	9.95E-02	1.28E-01	1.63E-01	1.99E-01	2.38E-01	2.74E-01	3.08E-01	3.41E-01	4.01E-01	4.53E-01	4.90E-01
Ni	3.02E-06	2.25E-03	5.00E-03	7.13E-03	8.45E-03	9.24E-03	1.00E-02	1.10E-02	1.23E-02	1.39E-02	1.58E-02	1.78E-02	1.99E-02	2.45E-02	2.93E-02	3.35E-02
Cu	1.11E-05	6.56E-02	1.24E-01	1.64E-01	1.92E-01	2.15E-01	2.39E-01	2.66E-01	2.95E-01	3.30E-01	3.64E-01	3.97E-01	4.29E-01	4.90E-01	5.44E-01	5.83E-01
Zn	2.56E-06	1.15E-02	3.24E-02	5.29E-02	6.81E-02	7.90E-02	8.74E-02	9.49E-02	1.02E-01	1.11E-01	1.20E-01	1.30E-01	1.40E-01	1.61E-01	1.83E-01	2.02E-01
Ga	8.70E-06	4.04E-02	9.26E-02	1.39E-01	1.74E-01	2.02E-01	2.27E-01	2.48E-01	2.69E-01	2.91E-01	3.13E-01	3.35E-01	3.58E-01	4.00E-01	4.43E-01	4.75E-01
Ge	2.56E-06	2.95E-02	7.10E-02	1.13E-01	1.48E-01	1.75E-01	2.00E-01	2.21E-01	2.41E-01	2.62E-01	2.83E-01	3.04E-01	3.24E-01	3.63E-01	4.04E-01	4.35E-01
As	-4.84E-06	1.53E-02	3.88E-02	6.59E-02	9.00E-02	1.09E-01	1.27E-01	1.43E-01	1.58E-01	1.75E-01	1.90E-01	2.06E-01	2.22E-01	2.51E-01	2.84E-01	3.09E-01
Se	5.91E-06	2.58E-02	6.38E-02	1.08E-01	1.48E-01	1.79E-01	2.09E-01	2.35E-01	2.58E-01	2.84E-01	3.07E-01	3.30E-01	3.54E-01	3.95E-01	4.41E-01	4.73E-01
Br	-9.21E-06	9.82E-03	2.93E-02	5.49E-02	8.14E-02	1.09E-01	1.31E-01	1.54E-01	1.75E-01	1.98E-01	2.18E-01	2.38E-01	2.59E-01	2.96E-01	3.32E-01	3.61E-01

Table 20—Continued

[El/Fe]	TDU 1	TDU 2	TDU 3	TDU 4	TDU 5	TDU 6	TDU 7	TDU 8	TDU 9	TDU 10	TDU 11	TDU 12	TDU 13	TDU 15	TDU 17	TDU 19
Kr	6.63E-06	3.08E-02	8.16E-02	1.41E-01	1.93E-01	2.34E-01	2.71E-01	3.05E-01	3.35E-01	3.67E-01	3.97E-01	4.26E-01	4.56E-01	5.09E-01	5.67E-01	6.11E-01
Rb	2.56E-06	7.17E-02	1.45E-01	2.23E-01	3.03E-01	3.77E-01	4.47E-01	5.10E-01	5.65E-01	6.21E-01	6.71E-01	7.17E-01	7.64E-01	8.42E-01	9.18E-01	9.74E-01
Sr	6.38E-06	7.82E-02	2.70E-01	4.75E-01	6.27E-01	7.22E-01	7.94E-01	8.52E-01	9.00E-01	9.46E-01	9.86E-01	1.02E+00	1.06E+00	1.13E+00	1.20E+00	1.26E+00
Y	2.56E-06	1.04E-01	2.99E-01	5.01E-01	6.60E-01	7.66E-01	8.47E-01	9.15E-01	9.72E-01	1.03E+00	1.07E+00	1.11E+00	1.16E+00	1.23E+00	1.31E+00	1.37E+00
Zr	2.56E-06	1.38E-01	3.52E-01	5.48E-01	6.94E-01	7.95E-01	8.73E-01	9.40E-01	9.97E-01	1.05E+00	1.10E+00	1.14E+00	1.19E+00	1.27E+00	1.35E+00	1.41E+00
Nb	-1.21E-05	1.21E-05	1.47E-02	4.43E-02	8.74E-02	1.63E-01	2.14E-01	2.81E-01	3.42E-01	4.08E-01	4.61E-01	5.12E-01	5.64E-01	6.48E-01	7.16E-01	7.77E-01
Mo	5.72E-06	9.16E-02	2.61E-01	4.23E-01	5.41E-01	6.22E-01	6.84E-01	7.39E-01	7.87E-01	8.34E-01	8.76E-01	9.17E-01	9.57E-01	1.03E+00	1.11E+00	1.16E+00
Ru	-2.34E-06	5.74E-02	1.93E-01	3.41E-01	4.53E-01	5.32E-01	5.87E-01	6.34E-01	6.75E-01	7.13E-01	7.48E-01	7.81E-01	8.14E-01	8.76E-01	9.47E-01	1.00E+00
Rh	-1.52E-05	2.72E-02	9.94E-02	1.90E-01	2.65E-01	3.19E-01	3.60E-01	3.96E-01	4.27E-01	4.57E-01	4.85E-01	5.13E-01	5.40E-01	5.93E-01	6.57E-01	7.08E-01
Pd	1.19E-05	7.93E-02	2.60E-01	4.43E-01	5.76E-01	6.67E-01	7.32E-01	7.87E-01	8.35E-01	8.79E-01	9.21E-01	9.59E-01	9.97E-01	1.07E+00	1.15E+00	1.20E+00
Ag	-1.61E-05	2.03E-02	8.12E-02	1.62E-01	2.31E-01	2.84E-01	3.24E-01	3.61E-01	3.94E-01	4.26E-01	4.56E-01	4.85E-01	5.15E-01	5.70E-01	6.34E-01	6.81E-01
Cd	8.25E-06	9.19E-02	3.01E-01	5.09E-01	6.61E-01	7.66E-01	8.40E-01	9.03E-01	9.56E-01	1.01E+00	1.05E+00	1.09E+00	1.13E+00	1.21E+00	1.29E+00	1.35E+00
In	-8.46E-06	5.37E-02	2.04E-01	3.76E-01	5.09E-01	6.04E-01	6.71E-01	7.27E-01	7.74E-01	8.19E-01	8.59E-01	8.97E-01	9.34E-01	1.00E+00	1.08E+00	1.14E+00
Sn	3.77E-06	1.19E-01	3.48E-01	5.63E-01	7.16E-01	8.29E-01	9.12E-01	9.82E-01	1.04E+00	1.10E+00	1.15E+00	1.20E+00	1.24E+00	1.32E+00	1.41E+00	1.47E+00
Sb	-1.09E-05	6.31E-02	1.88E-01	3.35E-01	4.58E-01	5.59E-01	6.38E-01	7.09E-01	7.71E-01	8.28E-01	8.82E-01	9.30E-01	9.77E-01	1.06E+00	1.15E+00	1.21E+00

Table 20—Continued

[El/Fe]	TDU 1	TDU 2	TDU 3	TDU 4	TDU 5	TDU 6	TDU 7	TDU 8	TDU 9	TDU 10	TDU 11	TDU 12	TDU 13	TDU 15	TDU 17	TDU 19
Te	1.16E-06	4.37E-02	1.50E-01	2.71E-01	3.65E-01	4.39E-01	4.96E-01	5.47E-01	5.92E-01	6.36E-01	6.77E-01	7.16E-01	7.55E-01	8.25E-01	9.02E-01	9.58E-01
I	-1.97E-05	1.24E-02	4.85E-02	9.92E-02	1.44E-01	1.81E-01	2.10E-01	2.37E-01	2.62E-01	2.86E-01	3.11E-01	3.34E-01	3.59E-01	4.06E-01	4.62E-01	5.08E-01
Xe	6.72E-06	5.53E-02	1.74E-01	3.08E-01	4.12E-01	4.94E-01	5.58E-01	6.14E-01	6.64E-01	7.12E-01	7.57E-01	7.99E-01	8.41E-01	9.16E-01	9.96E-01	1.05E+00
Cs	-2.35E-06	8.73E-02	2.37E-01	4.19E-01	5.65E-01	6.78E-01	7.62E-01	8.33E-01	8.93E-01	9.49E-01	1.00E+00	1.05E+00	1.09E+00	1.17E+00	1.26E+00	1.32E+00
Ba	5.06E-06	3.00E-01	6.98E-01	9.91E-01	1.17E+00	1.30E+00	1.39E+00	1.47E+00	1.53E+00	1.59E+00	1.65E+00	1.70E+00	1.75E+00	1.84E+00	1.93E+00	1.99E+00
La	2.56E-06	3.10E-01	7.24E-01	1.03E+00	1.21E+00	1.34E+00	1.43E+00	1.51E+00	1.57E+00	1.63E+00	1.69E+00	1.74E+00	1.80E+00	1.89E+00	1.97E+00	2.03E+00
Ce	6.55E-07	3.56E-01	8.03E-01	1.12E+00	1.31E+00	1.45E+00	1.54E+00	1.62E+00	1.69E+00	1.75E+00	1.81E+00	1.87E+00	1.92E+00	2.01E+00	2.10E+00	2.15E+00
Pr	-2.57E-06	2.41E-01	6.09E-01	9.20E-01	1.13E+00	1.28E+00	1.38E+00	1.47E+00	1.54E+00	1.61E+00	1.67E+00	1.73E+00	1.78E+00	1.88E+00	1.97E+00	2.02E+00
Nd	2.56E-06	3.04E-01	7.18E-01	1.02E+00	1.22E+00	1.35E+00	1.44E+00	1.52E+00	1.58E+00	1.64E+00	1.70E+00	1.75E+00	1.80E+00	1.90E+00	1.98E+00	2.04E+00
Sm	-4.37E-06	2.59E-01	5.91E-01	8.46E-01	1.02E+00	1.14E+00	1.24E+00	1.32E+00	1.39E+00	1.45E+00	1.51E+00	1.57E+00	1.63E+00	1.72E+00	1.81E+00	1.86E+00
Eu	-2.54E-05	6.15E-02	1.86E-01	3.25E-01	4.39E-01	5.33E-01	6.10E-01	6.78E-01	7.36E-01	7.95E-01	8.51E-01	9.05E-01	9.56E-01	1.05E+00	1.13E+00	1.18E+00
Gd	7.94E-06	1.65E-01	3.97E-01	6.11E-01	7.75E-01	9.01E-01	9.99E-01	1.08E+00	1.16E+00	1.23E+00	1.29E+00	1.35E+00	1.41E+00	1.51E+00	1.60E+00	1.65E+00
Tb	-1.26E-05	9.74E-02	2.67E-01	4.27E-01	5.57E-01	6.61E-01	7.46E-01	8.21E-01	8.87E-01	9.50E-01	1.01E+00	1.07E+00	1.13E+00	1.22E+00	1.31E+00	1.36E+00
Dy	-2.15E-05	1.66E-01	4.12E-01	6.12E-01	7.53E-01	8.64E-01	9.49E-01	1.03E+00	1.09E+00	1.16E+00	1.22E+00	1.28E+00	1.34E+00	1.44E+00	1.52E+00	1.58E+00
Ho	9.25E-05	9.92E-02	2.57E-01	4.16E-01	5.45E-01	6.21E-01	7.14E-01	7.80E-01	8.54E-01	8.87E-01	9.51E-01	1.01E+00	1.05E+00	1.14E+00	1.23E+00	1.28E+00

Table 20—Continued

[El/Fe]	TDU 1	TDU 2	TDU 3	TDU 4	TDU 5	TDU 6	TDU 7	TDU 8	TDU 9	TDU 10	TDU 11	TDU 12	TDU 13	TDU 15	TDU 17	TDU 19
Er	1.21E-05	1.88E-01	4.57E-01	6.82E-01	8.34E-01	9.45E-01	1.03E+00	1.10E+00	1.17E+00	1.23E+00	1.29E+00	1.35E+00	1.41E+00	1.50E+00	1.59E+00	1.64E+00
Tm	-4.63E-06	1.45E-01	4.04E-01	6.11E-01	7.45E-01	8.42E-01	9.18E-01	9.86E-01	1.05E+00	1.10E+00	1.16E+00	1.22E+00	1.27E+00	1.37E+00	1.45E+00	1.51E+00
Yb	1.32E-05	3.49E-01	7.20E-01	9.92E-01	1.17E+00	1.29E+00	1.38E+00	1.46E+00	1.52E+00	1.58E+00	1.64E+00	1.70E+00	1.76E+00	1.85E+00	1.94E+00	1.99E+00
Lu	-8.88E-04	2.09E-01	5.17E-01	7.62E-01	9.20E-01	1.03E+00	1.11E+00	1.18E+00	1.24E+00	1.30E+00	1.36E+00	1.42E+00	1.47E+00	1.56E+00	1.64E+00	1.70E+00
Hf	1.92E-04	4.66E-01	8.57E-01	1.13E+00	1.32E+00	1.44E+00	1.53E+00	1.61E+00	1.68E+00	1.74E+00	1.81E+00	1.86E+00	1.92E+00	2.02E+00	2.10E+00	2.16E+00
Ta	-5.97E-06	3.81E-01	7.78E-01	1.05E+00	1.23E+00	1.35E+00	1.43E+00	1.51E+00	1.57E+00	1.63E+00	1.69E+00	1.75E+00	1.80E+00	1.90E+00	1.98E+00	2.04E+00
W	2.56E-06	4.80E-01	9.04E-01	1.19E+00	1.37E+00	1.49E+00	1.57E+00	1.64E+00	1.71E+00	1.77E+00	1.82E+00	1.88E+00	1.93E+00	2.03E+00	2.11E+00	2.16E+00
Re	-6.34E-02	1.63E-01	4.63E-01	7.22E-01	8.96E-01	1.01E+00	1.10E+00	1.17E+00	1.23E+00	1.29E+00	1.35E+00	1.40E+00	1.45E+00	1.55E+00	1.63E+00	1.69E+00
Os	4.54E-03	1.26E-01	3.25E-01	5.12E-01	6.54E-01	7.58E-01	8.38E-01	9.07E-01	9.67E-01	1.03E+00	1.08E+00	1.14E+00	1.19E+00	1.28E+00	1.36E+00	1.41E+00
Ir	-2.16E-05	2.35E-02	7.51E-02	1.42E-01	2.07E-01	2.63E-01	3.11E-01	3.57E-01	3.98E-01	4.41E-01	4.84E-01	5.27E-01	5.68E-01	6.45E-01	7.13E-01	7.59E-01
Pt	1.41E-05	9.52E-02	2.58E-01	4.15E-01	5.40E-01	6.37E-01	7.13E-01	7.81E-01	8.41E-01	9.00E-01	9.58E-01	1.01E+00	1.07E+00	1.16E+00	1.24E+00	1.29E+00
Au	-3.15E-06	7.59E-02	2.31E-01	3.89E-01	5.07E-01	5.93E-01	6.56E-01	7.12E-01	7.62E-01	8.11E-01	8.60E-01	9.08E-01	9.55E-01	1.04E+00	1.11E+00	1.17E+00
Hg	2.34E-05	4.00E-01	8.35E-01	1.14E+00	1.33E+00	1.45E+00	1.54E+00	1.61E+00	1.67E+00	1.73E+00	1.79E+00	1.84E+00	1.89E+00	1.98E+00	2.06E+00	2.12E+00
Tl	1.36E-06	4.53E-01	9.66E-01	1.29E+00	1.50E+00	1.63E+00	1.72E+00	1.80E+00	1.86E+00	1.92E+00	1.98E+00	2.03E+00	2.08E+00	2.17E+00	2.25E+00	2.30E+00
Pb	2.56E-06	1.16E+00	1.78E+00	2.11E+00	2.32E+00	2.45E+00	2.54E+00	2.60E+00	2.65E+00	2.70E+00	2.73E+00	2.76E+00	2.78E+00	2.83E+00	2.86E+00	2.87E+00

Table 20—Continued

[El/Fe]	TDU 1	TDU 2	TDU 3	TDU 4	TDU 5	TDU 6	TDU 7	TDU 8	TDU 9	TDU 10	TDU 11	TDU 12	TDU 13	TDU 15	TDU 17	TDU 19
Bi	2.56E-06	8.43E-01	1.33E+00	1.63E+00	1.84E+00	1.98E+00	2.09E+00	2.16E+00	2.23E+00	2.28E+00	2.32E+00	2.35E+00	2.37E+00	2.42E+00	2.44E+00	2.46E+00

Table 21. Pulse by pulse elemental surface composition of the $Z = 0.0001$ model (online only).

[El/Fe]	TDU 1	TDU 2	TDU 3	TDU 4	TDU 5	TDU 6	TDU 7	TDU 8	TDU 9	TDU 10	TDU 11	TDU 12	TDU 13	TDU 14	TDU 15
C	1.15E+00	1.72E+00	2.04E+00	2.26E+00	2.41E+00	2.52E+00	2.61E+00	2.69E+00	2.75E+00	2.81E+00	2.86E+00	2.90E+00	2.95E+00	2.99E+00	3.00E+00
N	4.93E-01	4.95E-01	5.01E-01	5.11E-01	5.23E-01	5.39E-01	5.56E-01	5.75E-01	5.95E-01	6.17E-01	6.41E-01	6.68E-01	7.01E-01	7.51E-01	8.58E-01
O	-9.15E-04	1.49E-01	3.30E-01	4.82E-01	5.95E-01	6.79E-01	7.43E-01	7.95E-01	8.38E-01	8.76E-01	9.09E-01	9.40E-01	9.71E-01	1.00E+00	1.01E+00
F	-8.31E-02	1.16E+00	1.65E+00	1.94E+00	2.13E+00	2.27E+00	2.37E+00	2.47E+00	2.54E+00	2.62E+00	2.68E+00	2.75E+00	2.82E+00	2.88E+00	2.90E+00
Ne	-3.48E-03	4.30E-01	8.19E-01	1.09E+00	1.30E+00	1.46E+00	1.60E+00	1.71E+00	1.82E+00	1.91E+00	2.00E+00	2.08E+00	2.17E+00	2.24E+00	2.27E+00
Na	2.22E-01	2.38E-01	3.73E-01	5.77E-01	7.70E-01	9.34E-01	1.07E+00	1.19E+00	1.30E+00	1.40E+00	1.49E+00	1.58E+00	1.66E+00	1.74E+00	1.77E+00
Mg	-2.92E-04	2.39E-03	3.81E-02	1.18E-01	2.31E-01	3.60E-01	4.92E-01	6.21E-01	7.43E-01	8.59E-01	9.67E-01	1.07E+00	1.17E+00	1.27E+00	1.30E+00
Al	7.02E-03	2.28E-02	6.55E-02	1.29E-01	1.94E-01	2.53E-01	3.04E-01	3.51E-01	3.95E-01	4.37E-01	4.80E-01	5.23E-01	5.69E-01	6.15E-01	6.37E-01
Si	9.10E-04	2.55E-03	4.95E-03	8.07E-03	1.18E-02	1.61E-02	2.08E-02	2.58E-02	3.12E-02	3.69E-02	4.28E-02	4.91E-02	5.63E-02	6.35E-02	6.61E-02
P	2.27E-05	6.64E-03	2.90E-02	6.19E-02	9.92E-02	1.37E-01	1.72E-01	2.06E-01	2.36E-01	2.64E-01	2.90E-01	3.14E-01	3.39E-01	3.60E-01	3.67E-01
S	4.87E-07	8.39E-05	3.32E-04	7.02E-04	1.14E-03	1.60E-03	2.05E-03	2.48E-03	2.88E-03	3.26E-03	3.61E-03	3.93E-03	4.26E-03	4.55E-03	4.65E-03
Cl	9.84E-05	5.73E-04	1.30E-03	2.14E-03	3.03E-03	4.03E-03	5.06E-03	6.14E-03	7.35E-03	8.57E-03	9.79E-03	1.10E-02	1.24E-02	1.37E-02	1.42E-02
Ar	-6.15E-06	9.16E-06	6.10E-05	1.65E-04	3.34E-04	5.73E-04	8.92E-04	1.24E-03	1.65E-03	2.09E-03	2.59E-03	3.16E-03	3.61E-03	4.17E-03	4.38E-03
K	-1.40E-04	2.88E-04	1.14E-03	2.43E-03	4.16E-03	6.13E-03	8.29E-03	1.10E-02	1.40E-02	1.69E-02	1.96E-02	2.19E-02	2.64E-02	3.00E-02	3.14E-02
Ca	5.81E-06	-9.99E-05	-3.36E-04	-6.80E-04	-1.12E-03	-1.62E-03	-2.18E-03	-2.78E-03	-3.39E-03	-4.03E-03	-4.69E-03	-5.37E-03	-6.13E-03	-6.88E-03	-7.16E-03

Table 21—Continued

[El/Fe]	TDU 1	TDU 2	TDU 3	TDU 4	TDU 5	TDU 6	TDU 7	TDU 8	TDU 9	TDU 10	TDU 11	TDU 12	TDU 13	TDU 14	TDU 15
Sc	4.96E-04	4.95E-03	1.34E-02	2.58E-02	4.22E-02	6.24E-02	8.56E-02	1.11E-01	1.38E-01	1.64E-01	1.90E-01	2.15E-01	2.41E-01	2.66E-01	2.75E-01
Ti	5.91E-06	5.15E-04	1.45E-03	2.70E-03	4.14E-03	5.68E-03	7.29E-03	8.99E-03	1.09E-02	1.28E-02	1.47E-02	1.65E-02	1.87E-02	2.07E-02	2.15E-02
V	1.10E-04	3.24E-04	3.04E-04	7.60E-05	-3.39E-04	-9.21E-04	-1.62E-03	-2.36E-03	-3.07E-03	-3.81E-03	-4.61E-03	-5.46E-03	-6.39E-03	-7.36E-03	-7.71E-03
Cr	-7.02E-07	2.27E-05	7.59E-05	1.56E-04	2.66E-04	3.96E-04	5.45E-04	7.10E-04	8.86E-04	1.07E-03	1.26E-03	1.46E-03	1.68E-03	1.91E-03	2.01E-03
Mn	2.61E-04	1.09E-03	1.83E-03	2.28E-03	2.40E-03	2.21E-03	1.72E-03	1.04E-03	2.18E-04	-6.77E-04	-1.63E-03	-2.62E-03	-3.69E-03	-4.70E-03	-4.93E-03
Fe	0.00E+00	0.00E+00	0.00E+00	0.00E+00	0.00E+00	0.00E+00	0.00E+00	0.00E+00	0.00E+00	0.00E+00	0.00E+00	0.00E+00	0.00E+00	0.00E+00	0.00E+00
Co	7.18E-05	3.49E-03	1.60E-02	3.97E-02	7.34E-02	1.13E-01	1.58E-01	2.04E-01	2.49E-01	2.92E-01	3.33E-01	3.72E-01	4.12E-01	4.47E-01	4.60E-01
Ni	-1.88E-06	1.28E-05	1.46E-04	5.74E-04	1.46E-03	2.92E-03	4.89E-03	7.32E-03	1.02E-02	1.34E-02	1.68E-02	2.05E-02	2.45E-02	2.87E-02	3.04E-02
Cu	2.20E-04	4.26E-03	1.63E-02	3.85E-02	7.31E-02	1.20E-01	1.74E-01	2.32E-01	2.90E-01	3.46E-01	3.98E-01	4.44E-01	4.97E-01	5.42E-01	5.57E-01
Zn	-1.06E-05	1.22E-03	4.09E-03	8.41E-03	1.42E-02	2.26E-02	3.34E-02	4.58E-02	6.21E-02	7.84E-02	9.55E-02	1.13E-01	1.31E-01	1.50E-01	1.57E-01
Ga	1.60E-04	7.75E-03	2.09E-02	3.87E-02	5.94E-02	8.74E-02	1.22E-01	1.58E-01	2.06E-01	2.50E-01	2.92E-01	3.32E-01	3.72E-01	4.10E-01	4.22E-01
Ge	2.74E-05	8.36E-03	2.23E-02	4.11E-02	6.06E-02	8.66E-02	1.17E-01	1.49E-01	1.94E-01	2.33E-01	2.71E-01	3.06E-01	3.41E-01	3.75E-01	3.87E-01
As	-1.93E-04	4.57E-03	1.27E-02	2.43E-02	3.58E-02	5.13E-02	7.00E-02	8.90E-02	1.18E-01	1.43E-01	1.68E-01	1.91E-01	2.15E-01	2.38E-01	2.46E-01
Se	3.48E-05	1.20E-02	2.97E-02	5.41E-02	7.68E-02	1.06E-01	1.39E-01	1.71E-01	2.19E-01	2.58E-01	2.93E-01	3.24E-01	3.56E-01	3.86E-01	3.95E-01
Br	-2.61E-04	4.72E-03	1.27E-02	2.52E-02	3.88E-02	5.56E-02	7.63E-02	9.80E-02	1.30E-01	1.58E-01	1.84E-01	2.09E-01	2.35E-01	2.61E-01	2.74E-01

Table 21—Continued

[El/Fe]	TDU 1	TDU 2	TDU 3	TDU 4	TDU 5	TDU 6	TDU 7	TDU 8	TDU 9	TDU 10	TDU 11	TDU 12	TDU 13	TDU 14	TDU 15
Kr	9.98E-05	1.76E-02	4.51E-02	8.36E-02	1.20E-01	1.61E-01	2.07E-01	2.52E-01	3.12E-01	3.60E-01	4.00E-01	4.36E-01	4.71E-01	5.03E-01	5.14E-01
Rb	2.02E-05	2.40E-02	7.17E-02	1.48E-01	2.25E-01	3.09E-01	3.96E-01	4.78E-01	5.75E-01	6.51E-01	7.10E-01	7.59E-01	8.08E-01	8.49E-01	8.63E-01
Sr	1.19E-04	1.41E-01	2.81E-01	4.21E-01	5.17E-01	6.00E-01	6.70E-01	7.38E-01	8.11E-01	8.64E-01	9.04E-01	9.37E-01	9.74E-01	1.00E+00	1.01E+00
Y	8.69E-06	1.41E-01	2.96E-01	4.52E-01	5.66E-01	6.62E-01	7.41E-01	8.19E-01	9.00E-01	9.60E-01	1.00E+00	1.04E+00	1.08E+00	1.11E+00	1.12E+00
Zr	9.89E-06	1.40E-01	2.97E-01	4.52E-01	5.75E-01	6.77E-01	7.59E-01	8.42E-01	9.28E-01	9.92E-01	1.04E+00	1.08E+00	1.12E+00	1.16E+00	1.17E+00
Nb	-3.65E-04	-5.82E-04	4.29E-03	1.94E-02	5.12E-02	8.52E-02	1.31E-01	1.81E-01	2.36E-01	2.90E-01	3.42E-01	3.91E-01	4.39E-01	4.93E-01	5.30E-01
Mo	7.02E-05	8.91E-02	1.98E-01	3.09E-01	4.07E-01	4.91E-01	5.61E-01	6.35E-01	7.13E-01	7.76E-01	8.25E-01	8.63E-01	9.04E-01	9.37E-01	9.47E-01
Ru	-1.36E-04	5.86E-02	1.35E-01	2.13E-01	2.84E-01	3.42E-01	3.90E-01	4.42E-01	4.99E-01	5.47E-01	5.88E-01	6.20E-01	6.55E-01	6.85E-01	6.96E-01
Rh	-3.11E-04	3.11E-02	7.38E-02	1.21E-01	1.65E-01	2.02E-01	2.33E-01	2.68E-01	3.06E-01	3.41E-01	3.70E-01	3.93E-01	4.19E-01	4.41E-01	4.50E-01
Pd	1.96E-04	9.85E-02	2.16E-01	3.28E-01	4.23E-01	4.98E-01	5.56E-01	6.16E-01	6.79E-01	7.32E-01	7.75E-01	8.08E-01	8.44E-01	8.75E-01	8.86E-01
Ag	-3.48E-04	2.63E-02	6.37E-02	1.06E-01	1.47E-01	1.83E-01	2.14E-01	2.48E-01	2.87E-01	3.20E-01	3.48E-01	3.70E-01	3.95E-01	4.18E-01	4.26E-01
Cd	1.47E-04	1.19E-01	2.64E-01	3.97E-01	5.11E-01	5.96E-01	6.62E-01	7.33E-01	8.05E-01	8.63E-01	9.09E-01	9.44E-01	9.84E-01	1.02E+00	1.03E+00
In	-1.88E-04	7.72E-02	1.82E-01	2.85E-01	3.77E-01	4.47E-01	5.02E-01	5.61E-01	6.24E-01	6.75E-01	7.16E-01	7.46E-01	7.83E-01	8.12E-01	8.23E-01
Sn	2.64E-05	1.25E-01	2.85E-01	4.33E-01	5.65E-01	6.62E-01	7.36E-01	8.14E-01	8.95E-01	9.59E-01	1.01E+00	1.05E+00	1.09E+00	1.12E+00	1.13E+00
Sb	-2.49E-04	5.89E-02	1.58E-01	2.67E-01	3.82E-01	4.71E-01	5.44E-01	6.21E-01	7.02E-01	7.68E-01	8.19E-01	8.56E-01	8.99E-01	9.34E-01	9.46E-01

Table 21—Continued

[El/Fe]	TDU 1	TDU 2	TDU 3	TDU 4	TDU 5	TDU 6	TDU 7	TDU 8	TDU 9	TDU 10	TDU 11	TDU 12	TDU 13	TDU 14	TDU 15
Te	-3.36E-05	4.12E-02	1.04E-01	1.74E-01	2.50E-01	3.11E-01	3.63E-01	4.19E-01	4.81E-01	5.33E-01	5.74E-01	6.05E-01	6.41E-01	6.71E-01	6.80E-01
I	-4.12E-04	1.30E-02	3.52E-02	6.10E-02	9.17E-02	1.17E-01	1.40E-01	1.67E-01	1.98E-01	2.27E-01	2.51E-01	2.69E-01	2.91E-01	3.11E-01	3.18E-01
Xe	1.25E-04	5.94E-02	1.49E-01	2.42E-01	3.41E-01	4.15E-01	4.77E-01	5.42E-01	6.12E-01	6.73E-01	7.21E-01	7.57E-01	7.97E-01	8.31E-01	8.42E-01
Cs	-1.19E-04	7.15E-02	1.95E-01	3.20E-01	4.50E-01	5.42E-01	6.15E-01	6.90E-01	7.67E-01	8.32E-01	8.81E-01	9.17E-01	9.59E-01	9.93E-01	1.00E+00
Ba	6.13E-05	2.58E-01	5.33E-01	7.36E-01	9.21E-01	1.04E+00	1.13E+00	1.21E+00	1.29E+00	1.36E+00	1.41E+00	1.45E+00	1.50E+00	1.54E+00	1.55E+00
La	-4.48E-06	2.65E-01	5.44E-01	7.49E-01	9.37E-01	1.05E+00	1.15E+00	1.23E+00	1.31E+00	1.38E+00	1.43E+00	1.47E+00	1.52E+00	1.56E+00	1.57E+00
Ce	2.41E-06	3.17E-01	6.26E-01	8.43E-01	1.04E+00	1.16E+00	1.26E+00	1.34E+00	1.42E+00	1.49E+00	1.54E+00	1.59E+00	1.63E+00	1.67E+00	1.69E+00
Pr	-1.07E-04	2.25E-01	4.98E-01	7.08E-01	9.01E-01	1.02E+00	1.12E+00	1.21E+00	1.29E+00	1.35E+00	1.40E+00	1.45E+00	1.50E+00	1.54E+00	1.55E+00
Nd	-4.98E-06	2.58E-01	5.38E-01	7.44E-01	9.27E-01	1.04E+00	1.14E+00	1.23E+00	1.30E+00	1.37E+00	1.42E+00	1.47E+00	1.52E+00	1.56E+00	1.57E+00
Sm	-1.09E-04	1.64E-01	3.78E-01	5.63E-01	7.40E-01	8.61E-01	9.64E-01	1.05E+00	1.13E+00	1.20E+00	1.26E+00	1.30E+00	1.35E+00	1.39E+00	1.41E+00
Eu	-4.44E-04	3.36E-02	9.75E-02	1.73E-01	2.66E-01	3.40E-01	4.09E-01	4.72E-01	5.34E-01	5.87E-01	6.33E-01	6.72E-01	7.15E-01	7.51E-01	7.65E-01
Gd	6.74E-06	8.95E-02	2.40E-01	3.91E-01	5.51E-01	6.69E-01	7.71E-01	8.59E-01	9.40E-01	1.01E+00	1.06E+00	1.11E+00	1.16E+00	1.21E+00	1.22E+00
Tb	-2.43E-04	4.84E-02	1.37E-01	2.38E-01	3.56E-01	4.49E-01	5.34E-01	6.10E-01	6.81E-01	7.42E-01	7.94E-01	8.39E-01	8.85E-01	9.24E-01	9.39E-01
Dy	-6.82E-05	8.11E-02	2.08E-01	3.41E-01	4.90E-01	5.98E-01	6.98E-01	7.85E-01	8.67E-01	9.35E-01	9.91E-01	1.04E+00	1.09E+00	1.13E+00	1.15E+00
Ho	1.65E-05	4.87E-02	1.46E-01	2.44E-01	3.30E-01	4.43E-01	5.27E-01	5.96E-01	6.53E-01	7.15E-01	7.72E-01	8.17E-01	8.52E-01	8.78E-01	8.89E-01

Table 21—Continued

[El/Fe]	TDU 1	TDU 2	TDU 3	TDU 4	TDU 5	TDU 6	TDU 7	TDU 8	TDU 9	TDU 10	TDU 11	TDU 12	TDU 13	TDU 14	TDU 15
Er	1.89E-04	1.05E-01	2.57E-01	4.03E-01	5.55E-01	6.71E-01	7.74E-01	8.64E-01	9.47E-01	1.02E+00	1.08E+00	1.13E+00	1.18E+00	1.22E+00	1.23E+00
Tm	3.42E-05	8.02E-02	1.97E-01	3.15E-01	4.45E-01	5.49E-01	6.44E-01	7.29E-01	8.09E-01	8.77E-01	9.34E-01	9.85E-01	1.03E+00	1.08E+00	1.09E+00
Yb	3.10E-04	2.18E-01	4.64E-01	6.58E-01	8.37E-01	9.65E-01	1.08E+00	1.17E+00	1.26E+00	1.33E+00	1.39E+00	1.44E+00	1.50E+00	1.54E+00	1.55E+00
Lu	-1.11E-03	1.25E-01	2.95E-01	4.44E-01	5.91E-01	7.00E-01	7.97E-01	8.81E-01	9.60E-01	1.03E+00	1.09E+00	1.14E+00	1.19E+00	1.23E+00	1.24E+00
Hf	4.02E-04	3.03E-01	6.09E-01	8.28E-01	1.02E+00	1.16E+00	1.27E+00	1.36E+00	1.45E+00	1.52E+00	1.58E+00	1.64E+00	1.69E+00	1.73E+00	1.75E+00
Ta	-8.80E-05	2.41E-01	5.11E-01	7.12E-01	8.94E-01	1.02E+00	1.13E+00	1.22E+00	1.31E+00	1.38E+00	1.44E+00	1.49E+00	1.54E+00	1.59E+00	1.60E+00
W	-1.47E-05	2.92E-01	5.88E-01	7.99E-01	9.81E-01	1.11E+00	1.22E+00	1.31E+00	1.39E+00	1.46E+00	1.52E+00	1.57E+00	1.63E+00	1.67E+00	1.68E+00
Re	-7.45E-02	5.86E-02	2.49E-01	4.11E-01	5.65E-01	6.78E-01	7.79E-01	8.64E-01	9.44E-01	1.01E+00	1.07E+00	1.12E+00	1.17E+00	1.21E+00	1.23E+00
Os	4.98E-03	6.95E-02	1.78E-01	2.86E-01	4.01E-01	4.91E-01	5.76E-01	6.50E-01	7.20E-01	7.81E-01	8.34E-01	8.81E-01	9.28E-01	9.67E-01	9.81E-01
Ir	-4.27E-04	9.94E-03	3.32E-02	6.32E-02	1.02E-01	1.39E-01	1.77E-01	2.15E-01	2.54E-01	2.90E-01	3.23E-01	3.54E-01	3.85E-01	4.13E-01	4.23E-01
Pt	1.81E-04	4.45E-02	1.25E-01	2.15E-01	3.17E-01	4.03E-01	4.85E-01	5.59E-01	6.29E-01	6.90E-01	7.43E-01	7.91E-01	8.38E-01	8.77E-01	8.90E-01
Au	-9.42E-06	4.07E-02	1.10E-01	1.85E-01	2.68E-01	3.39E-01	4.08E-01	4.71E-01	5.33E-01	5.86E-01	6.34E-01	6.78E-01	7.21E-01	7.58E-01	7.70E-01
Hg	6.84E-04	3.19E-01	6.27E-01	8.43E-01	1.02E+00	1.14E+00	1.24E+00	1.32E+00	1.40E+00	1.46E+00	1.52E+00	1.57E+00	1.62E+00	1.66E+00	1.67E+00
Tl	-6.60E-06	3.96E-01	7.25E-01	9.47E-01	1.13E+00	1.25E+00	1.36E+00	1.44E+00	1.51E+00	1.57E+00	1.63E+00	1.67E+00	1.72E+00	1.76E+00	1.78E+00
Pb	9.70E-06	1.46E+00	1.95E+00	2.21E+00	2.37E+00	2.49E+00	2.58E+00	2.64E+00	2.69E+00	2.74E+00	2.78E+00	2.81E+00	2.84E+00	2.87E+00	2.88E+00

Table 21—Continued

[El/Fe]	TDU 1	TDU 2	TDU 3	TDU 4	TDU 5	TDU 6	TDU 7	TDU 8	TDU 9	TDU 10	TDU 11	TDU 12	TDU 13	TDU 14	TDU 15
Bi	-5.59E-07	9.88E-01	1.50E+00	1.80E+00	2.00E+00	2.14E+00	2.25E+00	2.33E+00	2.40E+00	2.46E+00	2.50E+00	2.55E+00	2.59E+00	2.62E+00	2.63E+00

Table 22. Final elemental surface composition of the 5 reference models at different metallicities (online only).

[El/Fe]	$Z = 1.38 \times 10^{-2}$	$Z = 6.0 \times 10^{-3}$	$Z = 3.0 \times 10^{-3}$	$Z = 1.0 \times 10^{-3}$	$Z = 1.0 \times 10^{-4}$
C	5.75E-01	1.17E+00	1.54E+00	2.18E+00	3.00E+00
N	3.65E-01	3.97E-01	4.38E-01	5.56E-01	8.58E-01
O	1.36E-03	2.90E-02	8.97E-02	3.22E-01	1.01E+00
F	4.88E-01	1.06E+00	1.47E+00	2.22E+00	2.90E+00
Ne	2.02E-01	5.58E-01	8.81E-01	1.60E+00	2.27E+00
Na	1.72E-01	3.58E-01	5.70E-01	1.28E+00	1.77E+00
Mg	1.06E-02	6.77E-02	1.70E-01	7.19E-01	1.30E+00
Al	1.06E-02	2.72E-02	4.41E-02	1.79E-01	6.37E-01
Si	1.12E-03	2.76E-03	4.71E-03	1.63E-02	6.61E-02
P	2.35E-02	5.85E-02	9.02E-02	1.96E-01	3.67E-01
S	4.82E-04	9.58E-04	1.20E-03	2.38E-03	4.65E-03
Cl	1.42E-02	2.62E-02	3.02E-02	4.37E-02	1.42E-02
Ar	-5.42E-04	-1.65E-03	-2.91E-03	-6.41E-03	4.38E-03
K	9.53E-03	2.18E-02	3.08E-02	6.09E-02	3.14E-02
Ca	-6.66E-04	-2.07E-03	-3.88E-03	-9.51E-03	-7.16E-03
Sc	4.53E-02	1.14E-01	1.70E-01	3.35E-01	2.75E-01
Ti	8.03E-03	2.22E-02	3.11E-02	4.42E-02	2.15E-02
V	2.11E-03	6.60E-03	6.48E-03	-2.17E-03	-7.71E-03
Cr	2.10E-04	8.20E-04	1.59E-03	3.46E-03	2.01E-03
Mn	5.72E-03	1.65E-02	1.80E-02	6.94E-03	-4.93E-03
Fe	0.00E+00	0.00E+00	0.00E+00	0.00E+00	0.00E+00

Table 22—Continued

[El/Fe]	$Z = 1.38 \times 10^{-2}$	$Z = 6.0 \times 10^{-3}$	$Z = 3.0 \times 10^{-3}$	$Z = 1.0 \times 10^{-3}$	$Z = 1.0 \times 10^{-4}$
Co	5.67E-02	1.34E-01	2.22E-01	4.90E-01	4.60E-01
Ni	2.74E-03	3.35E-03	7.26E-03	3.35E-02	3.04E-02
Cu	8.12E-02	1.47E-01	2.47E-01	5.83E-01	5.57E-01
Zn	4.41E-02	6.43E-02	8.41E-02	2.02E-01	1.57E-01
Ga	2.03E-01	2.50E-01	2.58E-01	4.75E-01	4.22E-01
Ge	2.04E-01	2.57E-01	2.52E-01	4.35E-01	3.87E-01
As	1.46E-01	1.87E-01	1.75E-01	3.09E-01	2.46E-01
Se	2.69E-01	3.34E-01	3.11E-01	4.73E-01	3.95E-01
Br	2.07E-01	2.68E-01	2.43E-01	3.61E-01	2.74E-01
Kr	3.60E-01	4.74E-01	4.64E-01	6.11E-01	5.14E-01
Rb	3.62E-01	5.57E-01	6.64E-01	9.74E-01	8.63E-01
Sr	1.11E+00	1.33E+00	1.26E+00	1.26E+00	1.01E+00
Y	1.08E+00	1.36E+00	1.33E+00	1.37E+00	1.12E+00
Zr	1.07E+00	1.39E+00	1.38E+00	1.41E+00	1.17E+00
Nb	4.61E-01	8.19E-01	8.03E-01	7.77E-01	5.30E-01
Mo	8.67E-01	1.22E+00	1.19E+00	1.16E+00	9.47E-01
Ru	7.62E-01	1.12E+00	1.09E+00	1.00E+00	6.96E-01
Rh	4.96E-01	8.13E-01	7.81E-01	7.08E-01	4.50E-01
Pd	9.08E-01	1.29E+00	1.26E+00	1.20E+00	8.86E-01
Ag	4.60E-01	7.79E-01	7.48E-01	6.81E-01	4.26E-01
Cd	9.87E-01	1.41E+00	1.40E+00	1.35E+00	1.03E+00

Table 22—Continued

[El/Fe]	$Z = 1.38 \times 10^{-2}$	$Z = 6.0 \times 10^{-3}$	$Z = 3.0 \times 10^{-3}$	$Z = 1.0 \times 10^{-3}$	$Z = 1.0 \times 10^{-4}$
In	8.04E-01	1.22E+00	1.21E+00	1.14E+00	8.23E-01
Sn	1.00E+00	1.47E+00	1.48E+00	1.47E+00	1.13E+00
Sb	6.19E-01	1.11E+00	1.17E+00	1.21E+00	9.46E-01
Te	5.70E-01	1.01E+00	1.00E+00	9.58E-01	6.80E-01
I	2.43E-01	5.72E-01	5.75E-01	5.08E-01	3.18E-01
Xe	5.61E-01	1.06E+00	1.07E+00	1.05E+00	8.42E-01
Cs	6.06E-01	1.25E+00	1.31E+00	1.32E+00	1.00E+00
Ba	1.10E+00	1.87E+00	2.01E+00	1.99E+00	1.55E+00
La	1.02E+00	1.88E+00	2.05E+00	2.03E+00	1.57E+00
Ce	9.51E-01	1.91E+00	2.15E+00	2.15E+00	1.69E+00
Pr	7.14E-01	1.69E+00	1.98E+00	2.02E+00	1.55E+00
Nd	7.69E-01	1.76E+00	2.04E+00	2.04E+00	1.57E+00
Sm	5.30E-01	1.49E+00	1.80E+00	1.86E+00	1.41E+00
Eu	1.43E-01	8.04E-01	1.10E+00	1.18E+00	7.65E-01
Gd	3.27E-01	1.19E+00	1.53E+00	1.65E+00	1.22E+00
Tb	2.18E-01	9.59E-01	1.26E+00	1.36E+00	9.39E-01
Dy	3.43E-01	1.20E+00	1.49E+00	1.58E+00	1.15E+00
Ho	1.90E-01	9.08E-01	1.20E+00	1.28E+00	8.89E-01
Er	3.60E-01	1.25E+00	1.57E+00	1.64E+00	1.23E+00
Tm	3.30E-01	1.19E+00	1.47E+00	1.51E+00	1.09E+00
Yb	5.80E-01	1.59E+00	1.93E+00	1.99E+00	1.55E+00

Table 22—Continued

[El/Fe]	$Z = 1.38 \times 10^{-2}$	$Z = 6.0 \times 10^{-3}$	$Z = 3.0 \times 10^{-3}$	$Z = 1.0 \times 10^{-3}$	$Z = 1.0 \times 10^{-4}$
Lu	4.04E-01	1.34E+00	1.66E+00	1.70E+00	1.24E+00
Hf	6.71E-01	1.72E+00	2.08E+00	2.16E+00	1.75E+00
Ta	5.96E-01	1.64E+00	1.99E+00	2.04E+00	1.60E+00
W	6.85E-01	1.76E+00	2.13E+00	2.16E+00	1.68E+00
Re	2.62E-01	1.25E+00	1.65E+00	1.69E+00	1.23E+00
Os	2.02E-01	9.75E-01	1.33E+00	1.41E+00	9.81E-01
Ir	3.12E-02	3.89E-01	6.73E-01	7.59E-01	4.23E-01
Pt	1.48E-01	8.28E-01	1.18E+00	1.29E+00	8.90E-01
Au	1.27E-01	7.91E-01	1.14E+00	1.17E+00	7.70E-01
Hg	6.02E-01	1.66E+00	2.08E+00	2.12E+00	1.67E+00
Tl	7.26E-01	1.81E+00	2.27E+00	2.30E+00	1.78E+00
Pb	5.43E-01	1.59E+00	2.32E+00	2.87E+00	2.88E+00
Bi	5.95E-02	6.58E-01	1.50E+00	2.46E+00	2.63E+00

Table 23. Stellar yields of the 5 reference models at different metallicities (online only).

Isotope	$Z = 1.38 \times 10^{-2}$	$Z = 6.0 \times 10^{-3}$	$Z = 3.0 \times 10^{-3}$	$Z = 1.0 \times 10^{-3}$	$Z = 1.0 \times 10^{-4}$
^1H	-4.06E-02	-7.05E-02	-8.21E-02	-1.16E-01	-9.92E-02
^2H	-3.77E-05	-3.79E-05	-3.86E-05	-5.42E-05	-5.39E-05
^3He	3.77E-04	3.35E-04	3.03E-04	2.59E-04	1.83E-04
^4He	3.23E-02	5.14E-02	6.31E-02	8.85E-02	7.99E-02
^6Li	-9.09E-10	-3.87E-10	-1.97E-10	-6.38E-11	-6.80E-12
^7Li	-1.29E-08	-5.43E-09	-2.70E-09	-7.86E-10	-1.60E-11
^7Be	2.39E-17	6.06E-17	4.60E-16	1.47E-16	8.07E-17
^9Be	-2.39E-10	-1.02E-10	-5.22E-11	-1.69E-11	-1.75E-12
^{10}B	-1.20E-09	-5.15E-10	-2.63E-10	-8.59E-11	-8.99E-12
^{11}B	-5.20E-09	-2.23E-09	-1.15E-09	-3.75E-10	-3.94E-11
^{12}C	5.84E-03	1.28E-02	1.64E-02	2.23E-02	1.71E-02
^{13}C	5.16E-05	2.03E-05	1.01E-05	3.63E-06	6.97E-07
^{14}C	2.07E-10	1.02E-09	1.65E-09	3.83E-09	2.80E-09
^{14}N	1.31E-03	6.03E-04	3.45E-04	1.52E-04	3.40E-05
^{15}N	-2.03E-06	-9.21E-07	-4.88E-07	-1.65E-07	-2.07E-08
^{16}O	-1.04E-05	1.70E-04	2.98E-04	4.47E-04	4.03E-04
^{17}O	3.32E-05	2.33E-05	1.68E-05	7.09E-06	9.33E-07
^{18}O	-5.65E-06	-2.78E-06	-1.53E-06	-5.08E-07	-3.20E-08
^{19}F	8.17E-07	1.61E-06	2.23E-06	3.97E-06	2.44E-06
^{20}Ne	-2.34E-06	1.33E-06	6.48E-06	2.80E-05	1.17E-05
^{21}Ne	8.15E-08	2.56E-07	3.94E-07	1.00E-06	5.54E-07

Table 23—Continued

Isotope	$Z = 1.38 \times 10^{-2}$	$Z = 6.0 \times 10^{-3}$	$Z = 3.0 \times 10^{-3}$	$Z = 1.0 \times 10^{-3}$	$Z = 1.0 \times 10^{-4}$
²² Ne	7.06E-04	1.21E-03	1.54E-03	2.69E-03	1.41E-03
²³ Na	1.95E-05	1.77E-05	1.77E-05	3.25E-05	1.38E-05
²⁴ Mg	9.94E-06	2.40E-05	3.32E-05	7.33E-05	2.64E-05
²⁵ Mg	7.10E-07	6.21E-06	1.28E-05	4.36E-05	2.55E-05
²⁶ Mg	3.16E-06	7.11E-06	8.17E-06	3.14E-05	3.21E-05
²⁶ Al	3.06E-07	1.24E-07	6.62E-08	5.40E-08	3.18E-08
²⁷ Al	1.00E-06	1.38E-06	1.25E-06	1.88E-06	1.43E-06
²⁸ Si	-1.01E-07	-1.27E-07	-1.08E-07	2.48E-07	6.81E-07
²⁹ Si	8.53E-08	1.49E-07	1.69E-07	1.97E-07	6.12E-08
³⁰ Si	5.24E-07	5.92E-07	5.88E-07	5.99E-07	9.89E-08
³² Si	4.12E-16	4.20E-15	1.24E-14	2.88E-14	3.42E-14
³¹ P	3.53E-07	3.97E-07	3.23E-07	2.42E-07	8.53E-08
³² P	1.22E-19	1.24E-18	3.68E-18	8.51E-18	1.01E-17
³² S	-6.76E-07	-7.54E-07	-6.74E-07	-5.54E-07	-2.33E-08
³³ S	8.49E-08	1.06E-07	7.94E-08	3.95E-08	3.63E-09
³⁴ S	2.53E-07	2.94E-07	2.84E-07	2.49E-07	1.31E-08
³⁶ S	2.05E-08	2.17E-08	1.92E-08	1.56E-08	1.67E-09
³⁵ Cl	-2.00E-08	-2.00E-08	-1.60E-08	-1.08E-08	-1.00E-09
³⁶ Cl	1.38E-09	1.42E-09	9.66E-10	4.34E-10	3.95E-11
³⁷ Cl	1.82E-07	1.45E-07	8.83E-08	4.05E-08	1.80E-09
³⁶ Ar	-4.64E-07	-4.73E-07	-3.92E-07	-2.91E-07	-1.07E-08

Table 23—Continued

Isotope	$Z = 1.38 \times 10^{-2}$	$Z = 6.0 \times 10^{-3}$	$Z = 3.0 \times 10^{-3}$	$Z = 1.0 \times 10^{-3}$	$Z = 1.0 \times 10^{-4}$
³⁸ Ar	1.28E-07	1.25E-07	1.07E-07	8.60E-08	9.35E-09
³⁹ Ar	3.59E-12	9.41E-12	1.10E-11	7.74E-12	9.88E-13
⁴⁰ Ar	2.04E-08	2.10E-08	1.69E-08	1.28E-08	7.03E-10
³⁹ K	3.14E-08	2.50E-08	1.78E-08	1.40E-08	4.58E-10
⁴⁰ K	7.10E-09	9.23E-09	6.93E-09	3.53E-09	2.14E-10
⁴¹ K	3.87E-08	3.94E-08	2.78E-08	1.49E-08	1.13E-09
⁴⁰ Ca	-2.85E-07	-2.91E-07	-2.41E-07	-1.80E-07	-1.68E-08
⁴¹ Ca	3.90E-09	3.38E-09	2.05E-09	8.58E-10	8.14E-11
⁴² Ca	2.43E-08	2.29E-08	1.79E-08	1.25E-08	1.10E-09
⁴³ Ca	4.59E-09	4.30E-09	3.59E-09	3.00E-09	2.82E-10
⁴⁴ Ca	2.20E-08	1.78E-08	1.00E-08	4.89E-09	3.65E-10
⁴⁶ Ca	1.24E-09	1.24E-09	1.38E-09	1.87E-09	1.82E-10
⁴⁸ Ca	-1.60E-10	-1.74E-10	-1.41E-10	-9.51E-11	-8.90E-12
⁴⁵ Sc	4.41E-09	4.89E-09	3.97E-09	2.97E-09	2.65E-10
⁴⁶ Ti	7.54E-09	6.39E-09	3.35E-09	8.34E-10	3.63E-11
⁴⁷ Ti	-1.97E-10	-3.36E-10	-4.36E-10	-4.38E-10	-5.03E-11
⁴⁸ Ti	-1.70E-08	-1.93E-08	-1.70E-08	-1.23E-08	-1.10E-09
⁴⁹ Ti	1.89E-08	2.20E-08	1.65E-08	8.60E-09	6.05E-10
⁵⁰ Ti	4.42E-08	5.85E-08	4.61E-08	2.29E-08	1.45E-09
⁵⁰ V	-1.30E-11	-1.46E-11	-1.16E-11	-7.24E-12	-5.98E-13
⁵¹ V	7.92E-10	1.69E-09	8.58E-10	-4.69E-10	-8.96E-11

Table 23—Continued

Isotope	$Z = 1.38 \times 10^{-2}$	$Z = 6.0 \times 10^{-3}$	$Z = 3.0 \times 10^{-3}$	$Z = 1.0 \times 10^{-3}$	$Z = 1.0 \times 10^{-4}$
⁵⁰ Cr	-1.05E-08	-1.17E-08	-9.32E-09	-5.78E-09	-4.87E-10
⁵² Cr	-5.40E-08	-5.39E-08	-4.57E-08	-3.85E-08	-3.87E-09
⁵³ Cr	-1.00E-08	-7.17E-09	-4.28E-09	-2.74E-09	-3.08E-10
⁵⁴ Cr	4.85E-08	5.44E-08	4.87E-08	3.80E-08	3.51E-09
⁵⁵ Mn	1.28E-07	1.69E-07	9.90E-08	1.90E-09	-2.31E-09
⁵⁴ Fe	-7.89E-07	-8.52E-07	-6.95E-07	-4.67E-07	-3.98E-08
⁵⁵ Fe	1.19E-12	1.62E-12	2.47E-12	3.97E-13	2.02E-14
⁵⁶ Fe	-5.39E-06	-5.92E-06	-5.15E-06	-4.07E-06	-3.78E-07
⁵⁷ Fe	1.67E-06	2.24E-06	1.89E-06	1.13E-06	8.31E-08
⁵⁸ Fe	1.95E-06	2.09E-06	2.08E-06	1.98E-06	1.92E-07
⁶⁰ Fe	5.76E-08	5.04E-08	6.35E-08	1.27E-07	1.89E-08
⁵⁹ Co	5.17E-07	5.17E-07	4.64E-07	4.55E-07	4.80E-08
⁶⁰ Co	2.02E-13	1.77E-13	2.23E-13	4.46E-13	6.63E-14
⁵⁸ Ni	-5.46E-07	-6.19E-07	-5.16E-07	-3.47E-07	-3.02E-08
⁵⁹ Ni	2.34E-08	2.60E-08	1.57E-08	4.77E-09	2.84E-10
⁶⁰ Ni	2.23E-07	2.13E-07	2.15E-07	2.01E-07	1.74E-08
⁶¹ Ni	1.66E-07	1.70E-07	1.51E-07	1.25E-07	1.20E-08
⁶² Ni	2.86E-07	2.40E-07	2.21E-07	1.98E-07	1.90E-08
⁶³ Ni	1.06E-12	3.29E-12	5.91E-12	6.71E-12	1.43E-12
⁶⁴ Ni	2.75E-07	1.91E-07	1.48E-07	1.57E-07	1.56E-08
⁶³ Cu	1.10E-07	1.01E-07	1.05E-07	1.23E-07	1.38E-08

Table 23—Continued

Isotope	$Z = 1.38 \times 10^{-2}$	$Z = 6.0 \times 10^{-3}$	$Z = 3.0 \times 10^{-3}$	$Z = 1.0 \times 10^{-3}$	$Z = 1.0 \times 10^{-4}$
⁶⁵ Cu	8.27E-08	5.88E-08	4.28E-08	3.66E-08	2.95E-09
⁶⁴ Zn	3.36E-08	1.88E-08	1.29E-08	5.32E-09	-2.42E-10
⁶⁶ Zn	8.34E-08	5.60E-08	4.03E-08	3.56E-08	2.89E-09
⁶⁷ Zn	1.87E-08	1.28E-08	9.17E-09	7.98E-09	6.71E-10
⁶⁸ Zn	1.03E-07	6.50E-08	4.23E-08	3.70E-08	3.45E-09
⁷⁰ Zn	-8.83E-11	-8.92E-11	-4.21E-11	1.86E-10	4.12E-11
⁶⁹ Ga	1.92E-08	1.10E-08	6.48E-09	5.18E-09	4.83E-10
⁷¹ Ga	2.13E-08	1.18E-08	5.76E-09	3.64E-09	3.21E-10
⁷⁰ Ge	3.50E-08	1.97E-08	1.05E-08	7.42E-09	6.77E-10
⁷² Ge	3.91E-08	2.27E-08	1.14E-08	7.22E-09	6.27E-10
⁷³ Ge	1.09E-08	6.52E-09	3.31E-09	2.12E-09	1.84E-10
⁷⁴ Ge	5.39E-08	3.11E-08	1.50E-08	9.21E-09	8.05E-10
⁷⁶ Ge	-1.45E-10	-1.38E-10	-7.56E-11	1.41E-10	2.98E-11
⁷⁵ As	4.80E-09	2.75E-09	1.30E-09	8.10E-10	7.06E-11
⁷⁶ Se	1.94E-08	1.11E-08	5.20E-09	3.04E-09	2.66E-10
⁷⁷ Se	7.78E-09	4.34E-09	1.99E-09	1.17E-09	1.04E-10
⁷⁸ Se	2.94E-08	1.69E-08	7.66E-09	4.21E-09	3.75E-10
⁷⁹ Se	3.54E-09	2.47E-09	1.24E-09	7.34E-10	9.01E-11
⁸⁰ Se	5.93E-08	3.41E-08	1.57E-08	8.52E-09	7.82E-10
⁸² Se	-2.50E-11	-4.35E-11	7.66E-12	1.33E-10	1.73E-11
⁷⁹ Br	4.80E-09	3.14E-09	1.57E-09	8.95E-10	5.66E-11

Table 23—Continued

Isotope	$Z = 1.38 \times 10^{-2}$	$Z = 6.0 \times 10^{-3}$	$Z = 3.0 \times 10^{-3}$	$Z = 1.0 \times 10^{-3}$	$Z = 1.0 \times 10^{-4}$
⁸¹ Br	1.02E-08	5.60E-09	2.36E-09	1.16E-09	1.04E-10
⁸⁰ Kr	5.36E-09	1.90E-09	4.69E-10	9.30E-11	6.24E-12
⁸¹ Kr	8.75E-10	2.29E-10	3.67E-11	7.03E-12	8.97E-13
⁸² Kr	3.87E-08	2.28E-08	9.51E-09	3.91E-09	3.30E-10
⁸³ Kr	1.27E-08	7.77E-09	3.32E-09	1.36E-09	1.12E-10
⁸⁴ Kr	8.07E-08	5.01E-08	2.28E-08	1.04E-08	8.73E-10
⁸⁶ Kr	1.91E-08	2.03E-08	1.47E-08	8.31E-09	8.22E-10
⁸⁵ Rb	1.42E-08	9.85E-09	5.32E-09	3.19E-09	3.04E-10
⁸⁷ Rb	5.99E-09	6.58E-09	6.05E-09	4.71E-09	4.60E-10
⁸⁶ Sr	4.11E-08	2.25E-08	8.13E-09	2.28E-09	1.70E-10
⁸⁷ Sr	2.67E-08	1.53E-08	5.61E-09	1.39E-09	8.75E-11
⁸⁸ Sr	5.78E-07	4.46E-07	1.94E-07	5.64E-08	3.72E-09
⁸⁹ Y	1.18E-07	1.01E-07	4.79E-08	1.55E-08	1.08E-09
⁹⁰ Zr	1.29E-07	1.14E-07	5.07E-08	1.34E-08	8.43E-10
⁹¹ Zr	3.12E-08	3.12E-08	1.56E-08	4.79E-09	3.06E-10
⁹² Zr	5.12E-08	5.09E-08	2.55E-08	8.42E-09	5.64E-10
⁹³ Zr	1.39E-08	1.30E-08	6.44E-09	2.21E-09	1.63E-10
⁹⁴ Zr	7.15E-08	7.38E-08	3.51E-08	1.03E-08	6.84E-10
⁹⁶ Zr	1.89E-09	4.66E-09	5.41E-09	4.52E-09	4.13E-10
⁹³ Nb	3.57E-09	4.13E-09	2.01E-09	5.95E-10	2.82E-11
⁹² Mo	-1.60E-11	-1.80E-11	-1.40E-11	-8.27E-12	-6.07E-13

Table 23—Continued

Isotope	$Z = 1.38 \times 10^{-2}$	$Z = 6.0 \times 10^{-3}$	$Z = 3.0 \times 10^{-3}$	$Z = 1.0 \times 10^{-3}$	$Z = 1.0 \times 10^{-4}$
⁹⁴ Mo	5.69E-10	4.40E-10	1.18E-10	3.01E-12	-2.69E-13
⁹⁵ Mo	6.99E-09	7.93E-09	4.13E-09	1.32E-09	8.48E-11
⁹⁶ Mo	1.49E-08	1.52E-08	6.88E-09	1.87E-09	1.25E-10
⁹⁷ Mo	5.16E-09	5.27E-09	2.38E-09	6.90E-10	4.96E-11
⁹⁸ Mo	1.86E-08	1.97E-08	8.84E-09	2.07E-09	1.33E-10
¹⁰⁰ Mo	1.62E-10	6.08E-10	6.24E-10	3.01E-10	1.72E-11
⁹⁹ Tc	7.25E-10	6.89E-10	3.06E-10	7.92E-11	6.94E-12
⁹⁶ Ru	-6.21E-12	-6.46E-12	-4.49E-12	-2.26E-12	-1.78E-13
⁹⁸ Ru	-1.01E-12	-1.30E-12	-1.14E-12	-7.29E-13	-6.02E-14
⁹⁹ Ru	1.83E-09	2.04E-09	9.26E-10	2.03E-10	1.06E-11
¹⁰⁰ Ru	9.32E-09	9.84E-09	4.39E-09	9.48E-10	5.43E-11
¹⁰¹ Ru	2.01E-09	2.16E-09	9.98E-10	2.30E-10	1.28E-11
¹⁰² Ru	1.03E-08	1.13E-08	5.22E-09	1.23E-09	6.54E-11
¹⁰⁴ Ru	1.73E-10	7.03E-10	6.42E-10	2.57E-10	1.36E-11
¹⁰³ Rh	2.14E-09	2.38E-09	1.11E-09	2.60E-10	1.36E-11
¹⁰⁴ Pd	7.04E-09	7.44E-09	3.32E-09	7.58E-10	3.95E-11
¹⁰⁵ Pd	1.81E-09	1.98E-09	9.26E-10	2.26E-10	1.17E-11
¹⁰⁶ Pd	8.26E-09	9.16E-09	4.27E-09	1.07E-09	5.62E-11
¹⁰⁷ Pd	1.56E-09	1.70E-09	7.88E-10	1.99E-10	1.08E-11
¹⁰⁸ Pd	1.02E-08	1.17E-08	5.45E-09	1.33E-09	7.20E-11
¹¹⁰ Pd	1.57E-10	7.12E-10	6.98E-10	2.99E-10	1.68E-11

Table 23—Continued

Isotope	$Z = 1.38 \times 10^{-2}$	$Z = 6.0 \times 10^{-3}$	$Z = 3.0 \times 10^{-3}$	$Z = 1.0 \times 10^{-3}$	$Z = 1.0 \times 10^{-4}$
¹⁰⁷ Ag	6.27E-11	9.60E-11	4.32E-11	6.92E-12	-1.43E-14
¹⁰⁹ Ag	2.64E-09	2.99E-09	1.39E-09	3.36E-10	1.82E-11
¹⁰⁸ Cd	4.38E-11	2.62E-11	5.98E-12	-2.82E-14	-2.04E-14
¹¹⁰ Cd	8.68E-09	9.75E-09	4.42E-09	1.00E-09	5.52E-11
¹¹¹ Cd	2.91E-09	3.36E-09	1.60E-09	3.87E-10	2.19E-11
¹¹² Cd	1.07E-08	1.28E-08	6.16E-09	1.48E-09	8.43E-11
¹¹³ Cd	3.13E-09	3.74E-09	1.80E-09	4.30E-10	2.45E-11
¹¹⁴ Cd	1.53E-08	1.87E-08	9.13E-09	2.20E-09	1.22E-10
¹¹⁶ Cd	2.58E-10	1.15E-09	1.37E-09	8.39E-10	5.09E-11
¹¹³ In	-7.30E-13	-6.66E-13	-4.32E-13	-2.08E-13	-1.61E-14
¹¹⁵ In	3.02E-09	3.76E-09	1.86E-09	4.52E-10	2.50E-11
¹¹⁴ Sn	-1.16E-12	-1.44E-12	-1.13E-12	-6.33E-13	-5.09E-14
¹¹⁵ Sn	-5.68E-13	-7.01E-13	-5.62E-13	-3.25E-13	-2.63E-14
¹¹⁶ Sn	2.10E-08	2.57E-08	1.21E-08	2.70E-09	1.42E-10
¹¹⁷ Sn	6.33E-09	7.87E-09	3.86E-09	9.84E-10	5.31E-11
¹¹⁸ Sn	2.75E-08	3.68E-08	1.87E-08	4.89E-09	2.64E-10
¹¹⁹ Sn	8.36E-09	1.11E-08	5.54E-09	1.44E-09	7.79E-11
¹²⁰ Sn	4.27E-08	6.13E-08	3.16E-08	8.42E-09	4.57E-10
¹²² Sn	2.79E-10	1.45E-09	2.21E-09	2.20E-09	1.73E-10
¹²⁴ Sn	-3.97E-12	6.44E-12	3.90E-11	1.49E-10	2.14E-11
¹²¹ Sb	3.23E-09	4.68E-09	2.44E-09	6.62E-10	3.60E-11

Table 23—Continued

Isotope	$Z = 1.38 \times 10^{-2}$	$Z = 6.0 \times 10^{-3}$	$Z = 3.0 \times 10^{-3}$	$Z = 1.0 \times 10^{-3}$	$Z = 1.0 \times 10^{-4}$
¹²³ Sb	1.86E-10	7.58E-10	6.64E-10	3.36E-10	2.21E-11
¹²² Te	5.49E-09	7.32E-09	3.57E-09	9.24E-10	5.03E-11
¹²³ Te	1.99E-09	2.55E-09	1.20E-09	3.02E-10	1.65E-11
¹²⁴ Te	1.08E-08	1.53E-08	7.46E-09	2.01E-09	1.18E-10
¹²⁵ Te	3.64E-09	5.19E-09	2.50E-09	6.52E-10	3.86E-11
¹²⁶ Te	1.98E-08	3.01E-08	1.50E-08	3.50E-09	1.92E-10
¹²⁸ Te	2.18E-09	3.82E-09	1.91E-09	7.06E-10	6.07E-11
¹³⁰ Te	-3.95E-11	-4.15E-11	-3.47E-11	-2.55E-11	-2.30E-12
¹²⁷ I	2.53E-09	3.94E-09	1.99E-09	4.47E-10	2.35E-11
¹²⁹ I	3.35E-11	7.80E-11	4.92E-11	2.03E-11	1.75E-12
¹²⁸ Xe	6.18E-09	9.33E-09	4.74E-09	1.09E-09	5.51E-11
¹²⁹ Xe	2.43E-09	3.81E-09	1.91E-09	4.33E-10	2.30E-11
¹³⁰ Xe	1.32E-08	2.07E-08	1.04E-08	2.37E-09	1.18E-10
¹³¹ Xe	3.56E-09	7.79E-09	2.94E-09	6.52E-10	4.25E-11
¹³² Xe	2.45E-08	4.16E-08	2.18E-08	5.13E-09	2.39E-10
¹³⁴ Xe	2.28E-10	1.44E-09	2.33E-09	2.32E-09	1.69E-10
¹³⁶ Xe	-2.22E-12	1.23E-12	1.49E-11	7.25E-11	1.42E-11
¹³³ Cs	3.22E-09	5.78E-09	3.12E-09	7.56E-10	3.47E-11
¹³⁵ Cs	7.34E-10	3.34E-09	2.24E-09	8.42E-10	5.97E-11
¹³⁴ Ba	9.02E-09	1.37E-08	6.40E-09	1.40E-09	6.57E-11
¹³⁵ Ba	3.28E-09	5.14E-09	2.29E-09	4.97E-10	2.31E-11

Table 23—Continued

Isotope	$Z = 1.38 \times 10^{-2}$	$Z = 6.0 \times 10^{-3}$	$Z = 3.0 \times 10^{-3}$	$Z = 1.0 \times 10^{-3}$	$Z = 1.0 \times 10^{-4}$
¹³⁶ Ba	2.32E-08	4.32E-08	2.23E-08	4.82E-09	2.39E-10
¹³⁷ Ba	1.81E-08	3.57E-08	2.02E-08	5.95E-09	3.70E-10
¹³⁸ Ba	1.38E-07	4.38E-07	3.10E-07	8.54E-08	3.80E-09
¹³⁹ La	1.56E-08	5.44E-08	3.96E-08	1.08E-08	4.80E-10
¹⁴⁰ Ce	3.52E-08	1.57E-07	1.32E-07	3.44E-08	1.36E-09
¹⁴² Ce	9.99E-11	1.68E-09	4.10E-09	4.49E-09	2.65E-10
¹⁴¹ Pr	2.76E-09	1.40E-08	1.34E-08	4.26E-09	1.75E-10
¹⁴² Nd	7.89E-09	3.82E-08	3.28E-08	7.27E-09	2.70E-10
¹⁴³ Nd	1.04E-09	5.57E-09	5.33E-09	1.66E-09	7.41E-11
¹⁴⁴ Nd	3.20E-09	1.73E-08	1.71E-08	5.53E-09	2.56E-10
¹⁴⁵ Nd	5.71E-10	3.17E-09	3.19E-09	1.03E-09	4.69E-11
¹⁴⁶ Nd	3.00E-09	1.62E-08	1.59E-08	4.95E-09	2.16E-10
¹⁴⁸ Nd	8.15E-11	1.44E-09	2.62E-09	1.23E-09	5.21E-11
¹⁵⁰ Nd	-3.82E-12	1.37E-11	8.29E-11	9.80E-11	4.04E-12
¹⁴⁴ Sm	-5.02E-13	-5.68E-13	-4.38E-13	-2.52E-13	-2.06E-14
¹⁴⁶ Sm	7.07E-14	7.64E-14	3.84E-14	6.43E-15	2.42E-16
¹⁴⁷ Sm	3.20E-10	1.86E-09	1.88E-09	5.84E-10	2.51E-11
¹⁴⁸ Sm	9.75E-10	4.70E-09	4.05E-09	1.11E-09	4.77E-11
¹⁴⁹ Sm	1.32E-10	7.46E-10	7.74E-10	2.62E-10	1.12E-11
¹⁵⁰ Sm	5.94E-10	3.31E-09	3.35E-09	1.10E-09	4.72E-11
¹⁵¹ Sm	2.71E-15	1.51E-14	2.49E-14	1.06E-14	5.97E-16

Table 23—Continued

Isotope	$Z = 1.38 \times 10^{-2}$	$Z = 6.0 \times 10^{-3}$	$Z = 3.0 \times 10^{-3}$	$Z = 1.0 \times 10^{-3}$	$Z = 1.0 \times 10^{-4}$
¹⁵² Sm	4.29E-10	2.67E-09	2.84E-09	9.84E-10	4.21E-11
¹⁵⁴ Sm	3.01E-11	6.48E-10	1.22E-09	5.95E-10	2.59E-11
¹⁵¹ Eu	7.69E-11	4.55E-10	4.67E-10	1.59E-10	6.71E-12
¹⁵³ Eu	7.49E-11	4.89E-10	5.25E-10	1.84E-10	7.84E-12
¹⁵² Gd	1.53E-11	4.99E-11	3.59E-11	1.16E-11	5.07E-13
¹⁵⁴ Gd	1.51E-10	7.84E-10	7.76E-10	2.65E-10	1.14E-11
¹⁵⁵ Gd	9.43E-11	6.26E-10	7.37E-10	2.80E-10	1.21E-11
¹⁵⁶ Gd	3.71E-10	2.10E-09	2.29E-09	8.58E-10	3.75E-11
¹⁵⁷ Gd	1.76E-10	9.78E-10	1.05E-09	3.93E-10	1.73E-11
¹⁵⁸ Gd	7.58E-10	4.11E-09	4.17E-09	1.51E-09	6.80E-11
¹⁶⁰ Gd	1.60E-11	4.22E-10	8.65E-10	4.81E-10	2.23E-11
¹⁵⁹ Tb	1.65E-10	9.33E-10	9.42E-10	3.41E-10	1.53E-11
¹⁶⁰ Dy	2.61E-10	1.37E-09	1.34E-09	4.71E-10	2.14E-11
¹⁶¹ Dy	1.14E-10	6.64E-10	6.95E-10	2.65E-10	1.21E-11
¹⁶² Dy	5.42E-10	2.98E-09	3.00E-09	1.09E-09	5.05E-11
¹⁶³ Dy	1.73E-10	9.82E-10	9.69E-10	3.41E-10	1.56E-11
¹⁶⁴ Dy	9.73E-10	5.46E-09	5.31E-09	1.69E-09	7.63E-11
¹⁶³ Ho	3.97E-13	1.64E-12	2.02E-12	1.05E-12	6.58E-14
¹⁶⁵ Ho	2.15E-10	1.28E-09	1.29E-09	4.35E-10	2.02E-11
¹⁶⁴ Er	8.04E-11	4.74E-10	4.96E-10	1.91E-10	9.10E-12
¹⁶⁶ Er	4.01E-10	2.05E-09	1.93E-09	6.17E-10	2.91E-11

Table 23—Continued

Isotope	$Z = 1.38 \times 10^{-2}$	$Z = 6.0 \times 10^{-3}$	$Z = 3.0 \times 10^{-3}$	$Z = 1.0 \times 10^{-3}$	$Z = 1.0 \times 10^{-4}$
¹⁶⁷ Er	1.82E-10	9.55E-10	9.10E-10	2.93E-10	1.39E-11
¹⁶⁸ Er	7.66E-10	4.21E-09	4.00E-09	1.20E-09	5.55E-11
¹⁷⁰ Er	6.39E-11	1.16E-09	2.02E-09	7.77E-10	3.40E-11
¹⁶⁹ Tm	1.92E-10	1.12E-09	1.08E-09	3.25E-10	1.51E-11
¹⁷⁰ Yb	2.53E-10	1.35E-09	1.26E-09	3.61E-10	1.64E-11
¹⁷¹ Yb	2.57E-10	1.71E-09	1.91E-09	5.83E-10	2.56E-11
¹⁷² Yb	7.55E-10	4.32E-09	4.52E-09	1.38E-09	6.10E-11
¹⁷³ Yb	3.47E-10	2.01E-09	2.09E-09	6.48E-10	2.85E-11
¹⁷⁴ Yb	1.62E-09	9.76E-09	1.01E-08	3.07E-09	1.32E-10
¹⁷⁶ Yb	3.71E-11	8.71E-10	1.94E-09	1.04E-09	4.44E-11
¹⁷⁵ Lu	2.17E-10	1.36E-09	1.42E-09	4.35E-10	1.86E-11
¹⁷⁶ Lu	3.84E-11	2.42E-10	2.52E-10	7.64E-11	3.24E-12
¹⁷⁶ Hf	2.92E-10	1.73E-09	1.77E-09	5.30E-10	2.26E-11
¹⁷⁷ Hf	1.67E-10	1.08E-09	1.20E-09	4.03E-10	1.72E-11
¹⁷⁸ Hf	7.86E-10	4.89E-09	5.38E-09	1.80E-09	7.69E-11
¹⁷⁹ Hf	2.67E-10	1.67E-09	1.83E-09	6.12E-10	2.61E-11
¹⁸⁰ Hf	1.48E-09	9.38E-09	1.01E-08	3.20E-09	1.37E-10
¹⁸² Hf	1.59E-11	4.17E-10	1.14E-09	7.12E-10	3.01E-11
¹⁸⁰ Ta	4.67E-14	3.03E-13	3.52E-13	1.31E-13	5.91E-15
¹⁸¹ Ta	2.98E-10	1.99E-09	2.19E-09	6.88E-10	2.93E-11
¹⁸⁰ W	-2.18E-14	-2.06E-14	-1.35E-14	-6.55E-15	-5.74E-16

Table 23—Continued

Isotope	$Z = 1.38 \times 10^{-2}$	$Z = 6.0 \times 10^{-3}$	$Z = 3.0 \times 10^{-3}$	$Z = 1.0 \times 10^{-3}$	$Z = 1.0 \times 10^{-4}$
¹⁸² W	7.09E-10	3.88E-09	3.73E-09	1.06E-09	4.48E-11
¹⁸³ W	4.27E-10	2.62E-09	2.76E-09	8.60E-10	3.63E-11
¹⁸⁴ W	1.10E-09	7.05E-09	7.55E-09	2.19E-09	9.07E-11
¹⁸⁶ W	1.93E-10	2.95E-09	4.95E-09	1.70E-09	6.78E-11
¹⁸⁵ Re	2.06E-10	1.39E-09	1.51E-09	4.33E-10	1.80E-11
¹⁸⁷ Re	-6.45E-12	5.80E-10	9.89E-10	3.43E-10	1.35E-11
¹⁸⁶ Os	4.36E-10	2.45E-09	2.45E-09	6.63E-10	2.73E-11
¹⁸⁷ Os	1.83E-10	7.14E-10	6.59E-10	1.76E-10	7.71E-12
¹⁸⁸ Os	5.34E-10	3.47E-09	4.19E-09	1.45E-09	5.98E-11
¹⁸⁹ Os	1.33E-10	9.44E-10	1.15E-09	4.06E-10	1.66E-11
¹⁹⁰ Os	7.13E-10	4.77E-09	5.62E-09	2.02E-09	8.50E-11
¹⁹² Os	3.31E-11	9.85E-10	1.64E-09	6.32E-10	2.65E-11
¹⁹¹ Ir	1.21E-10	1.01E-09	1.21E-09	4.31E-10	1.80E-11
¹⁹³ Ir	1.23E-10	1.20E-09	1.54E-09	5.47E-10	2.31E-11
¹⁹² Pt	3.13E-10	1.59E-09	1.59E-09	5.29E-10	2.29E-11
¹⁹⁴ Pt	8.69E-10	5.65E-09	6.85E-09	2.68E-09	1.20E-10
¹⁹⁵ Pt	2.94E-10	2.21E-09	2.62E-09	9.28E-10	4.13E-11
¹⁹⁶ Pt	1.37E-09	8.98E-09	1.06E-08	3.24E-09	1.43E-10
¹⁹⁸ Pt	2.46E-12	2.82E-10	9.56E-10	7.60E-10	3.35E-11
¹⁹⁷ Au	3.45E-10	2.46E-09	2.97E-09	8.86E-10	3.82E-11
¹⁹⁸ Hg	1.13E-09	7.43E-09	8.73E-09	2.31E-09	9.67E-11

Table 23—Continued

Isotope	$Z = 1.38 \times 10^{-2}$	$Z = 6.0 \times 10^{-3}$	$Z = 3.0 \times 10^{-3}$	$Z = 1.0 \times 10^{-3}$	$Z = 1.0 \times 10^{-4}$
¹⁹⁹ Hg	4.85E-10	3.43E-09	4.31E-09	1.25E-09	5.14E-11
²⁰⁰ Hg	1.64E-09	1.16E-08	1.50E-08	4.42E-09	1.70E-10
²⁰¹ Hg	6.68E-10	4.85E-09	6.48E-09	1.95E-09	7.30E-11
²⁰² Hg	2.74E-09	1.92E-08	2.55E-08	7.61E-09	2.77E-10
²⁰⁴ Hg	2.60E-12	1.32E-10	5.73E-10	7.91E-10	4.18E-11
²⁰³ Tl	1.21E-09	9.00E-09	1.29E-08	4.15E-09	1.51E-10
²⁰⁵ Tl	3.18E-09	2.18E-08	3.06E-08	8.74E-09	3.13E-10
²⁰⁴ Pb	2.06E-09	1.32E-08	1.68E-08	4.27E-09	1.51E-10
²⁰⁵ Pb	1.48E-10	1.05E-09	1.54E-09	3.95E-10	1.12E-11
²⁰⁶ Pb	1.05E-08	7.41E-08	1.38E-07	5.00E-08	2.17E-09
²⁰⁷ Pb	1.25E-08	8.01E-08	2.02E-07	8.74E-08	3.67E-09
²⁰⁸ Pb	1.88E-08	1.51E-07	5.50E-07	8.48E-07	1.03E-07
²⁰⁹ Bi	1.07E-10	1.21E-09	5.52E-09	1.63E-08	2.68E-09
²¹⁰ Po	1.66E-24	1.21E-22	4.54E-21	1.37E-20	1.41E-20